FZD-526

Silicon based microcavity enhanced light emitting diodes

Jaroslava Potfajova

Dezember 2009

Wissenschaftlich-Technische Berichte
FZD-526 2009 · ISSN 1437-322X

WISSENSCHAFTLICH-TECHNISCHE BERICHTE

Forschungszentrum
Dresden Rossendorf

Wissenschaftlich-Technische Berichte
FZD-526
Dezember 2009

Jaroslava Potfajova

Silicon based microcavity enhanced light emitting diodes

Forschungszentrum
Dresden Rossendorf

Silicon based microcavity enhanced light emitting diodes

Dissertation

vorgelegt der
Fakultät Mathematik und Naturwissenschaften
Technische Universität Dresden

von
Ing. Jaroslava Potfajova
geboren am 26. März 1980 in Trencin, Slowakei

Eingereicht am 30. Juli 2009
Verteidigt am 7. Dezember 2009

1. Gutachter: Prof. Dr. Manfred Helm
2. Gutachter: Prof. Dr. Thomas Dekorsy

It is better to light a candle, than to curse the darkness.
Konfuzius

Abstract

Realising Si-based electrically driven light emitters in a process technology compatible with mainstream microelectronics CMOS technology is key requirement for the implementation of low-cost Si-based optoelectronics and thus one of the big challenges of semiconductor technology. This work has focused on the development of microcavity enhanced silicon LEDs (MCLEDs), including their design, fabrication, and experimental as well as theoretical analysis. As a light emitting layer the abrupt pn-junction of a Si diode was used, which was fabricated by ion implantation of boron into n-type silicon. Such forward biased pn-junctions exhibit room-temperature EL at a wavelength of 1138 nm with a reasonably high power efficiency of 0.1% [1]. Two MCLEDs emitting light at the resonant wavelength about 1150 nm were demonstrated: *a)* 1λ MCLED with the resonator formed by 90 nm thin metallic $CoSi_2$ mirror at the bottom and semitranparent distributed Bragg reflector (DBR) on the top; *b)* 5.5λ MCLED with the resonator formed by high reflecting DBR at the bottom and semitransparent top DBR. Using the appoach of the 5.5λ MCLED with two DBRs the extraction efficiency is enhanced by about 65% compared to the silicon bulk pn-junction diode.

Keywords

microcavity, resonant cavity, Fabry-Perot resonator, distributed Bragg reflector, silicon light emitter, silicon diode, LED, MCLED

Contents

List of Abbreviations and Symbols

Abbreviations

AFM	atomic force microscopy
BHF	buffered hydrofluoric acid
BOE	buffered oxide etch
BOX	buried oxide
CCD	charge coupled device
CMOS	complementary metal oxide semiconductor
DBR	distributed Bragg reflector
DC	direct current
EDX	energy dispersive X-ray spectroscopy
EL	electroluminescence
EZ	emitting zone
FSR	free spectral range
FTIR	Fourier transform infrared spectroscopy
FWHM	full width at half maximum
H	high refractive index material
HVEM	high voltage electron microscopy
IC	integrated circuit
L	low refractive index material
LED	light emitting diode
MBE	molecular beam epitaxy
MCLED	micocavity light emitting diode
MIS	metal-insulator-semiconductor
MOS	metal-oxide-silicon
NA	numerical aperture
NBOHC	non-bridging oxygen hole center
NBS	National Bureau of Standards
NC	nanocrystals
ODC	oxygen deficiency center
OLED	organic light emitting diode
OX	oxide
PECVD	plasma enhanced chemical vapour deposition
PL	photoluminescence
PS	porous silicon

RCLED	resonant cavity light emitting diode
RF	radio frequency
SEM	scanning electron microscopy
SIMOX	separation by implantation of oxygen
SOI	silicon on insulator
SUB	substrate
TEM	transmission electron microscopy
TIR	total internal reflector
TTV	total thickness variation
VASE	variable angle spectroscopic ellipsometry
VCSEL	vertical-cavity surface-emitting lasers
VSL	variable stripe length

Symbols

A	area
a	amplitude
c	speed of light (299 792 458 ms^{-1})
d	thickness
$D_{n,p}$	carrier mobility
e	elementary charge (1.60217646 × 10^{-19} coulombs)
E	energy
F	finesse
G_{int}	integrated emission enhancement
G_e	spectral enhancement
h	Planck's constant (6.626068 × $10^{-34} m^2 kg s^{-1}$) h = $2\pi\hbar$
I	current
k	wave vector
L	length, thickness
l	optical mode
m	mass
n	refractive index
N_A	Avogadro's constant
p	momentum
P	power
Q	quality factor
R	resistivity, reflectance
r	reflectivity
T	temperature, transmittance
t	time, transmisivity
V	voltage, bias
W	transition rate
W_D	width of depletion zone
ϵ	permitivity
η	efficiency

λ	wavelength
μ	permeability
ν	frequency
Ω	solid angle
ϕ	phase
Φ	flux, fluence
ρ	density
σ	standard deviation
τ	lifetime
θ	emission / measurement angle
ξ	enhancement factor

Chapter 1

Introduction and motivation

Light emission from silicon has received growing interest in the past decades. The main reason is the possible monolithic integration of light emitters with silicon integrated circuits (IC), which would add significantly new functionalities to the modern ICs. Optical interconnection systems (emitter, modulator, waveguide, amplifier, detector) are being investigated as an outstanding solution to the interconnects bottleneck posed by conventional metal lines. Realising Si-based light emitters in a process technology compatible with mainstream microelectronics CMOS technology is one of the big challenges of semiconductor technology. The realisation of Si-based, electrically driven light emitters is a key requirement for the implementation of low-cost Si-based optoelectronics [2].

Silicon has an indirect energy bandgap what is the reason for a low radiative recombination rate, leading to efficiencies of the bandgap electroluminescence in the range of 10^{-6} [3]. Every approach to make a more efficient light emitter must either increase the radiative recombination rate or suppress the non-radiative recombination channels.

Recently, different approaches have led to an increase of the power efficiency of the bandgap EL by more than three orders of magnitude up to values of 0.1-1% [4, 5, 1]. These approaches are based on pn-diodes, where either the non-radiative lifetime is increased by using high-purity floatzone Si, combined with surface texturing to improve the outcoupling efficiency [4], or where specific defects introduced by ion implantation enhance the radiative recombination rate through carrier confinement effects [5, 1].

However, the spectral width and temporal response of these devices still constrains their practical application. One possible route for a further enhancement of the efficiency of these devices is a photonic confinement of the emitting layer. III-V semiconductor based light emitting diodes (LED) gained significantly in performance by incorporation into microcavities (MCs) [6, 7]. Optically excited Si based microcavity emitters have been demonstrated before, in SOI wafers [8] and in MOS devices containing nanoclusters and/or Er^{3+} ions in the silicon oxide [9]. In porous Si also cavity enhanced electroluminescence (EL) has been reported [10, 11]. In more recent attempts, photonic-crystal structures were integrated into Si based LEDs [12–14].

In a planar MCLED the spontaneous internal emission is controlled by placing the emitter between two highly reflecting mirrors forming an optical cavity with the thickness in the order of the emitting wavelength $d_{cavity} = i \times \lambda_{MC}/2n$, where i is the integer, λ_{MC} the resonance wavelength of the MC, n the refractive index of the cavity material. The resulting interference effects increase the brightness, efficiency and directionality of the emission from a high-index material and lead to more than an order of magnitude increase in the spectral power density [15].

The aim of this work is the development of microcavity enhanced silicon LEDs (MCLEDs), including their design, fabrication, and experimental as well as theoretical analysis. As a light emitting layer the abrupt pn-junction of a Si diode is used, which is fabricated by ion implantation of boron onto n-type silicon. Such forward biased pn-junctions exhibit room-temperature EL at a wavelength of 1138 nm with a reasonably high power efficiency of 0.1% [1]. For the fabrication of the microcavities two resonator types were realised: *i*) the resonator is formed by 90 nm thin metallic $CoSi_2$ mirror at the bottom and semi-tranparent distributed Bragg reflector (DBR) on the top; *ii*) the resonator formed by two DBRs.

The work is divided into three parts. Chapter two portrays the theoretical backgrounds of light emitting diodes, lists different principles of light emission from silicon and describes the microcavity enhancement effect. At the end of this chapter the design and the theoretical spectral calculation of the ideal 1λ silicon microcavity LED is presented. Chapter three describes the preparation and the characterisation methods used during the experiments. Chapter four is the most exciting part of this thesis, where the whole experimental work is described and where all the results are shown and discussed. It starts with the investigation of the single amorphous Si (a-Si) and SiO_2 layers building the multilayer stack acting as a distributed Bragg reflector (DBR) of the microcavity. Further a first microcavity enhanced silicon LED with metallic $CoSi_2$ mirror being the bottom part of the resonator and with the DBR on the top is presented. At the end of chapter four the most important part of this work is described more in detail, namely the fabrication process of the silicon based $5.5\ \lambda$ MCLED fabricated on SOI wafer (silicon on insulator) with the optical resonator consisting of two distributed Bragg reflectors, as well as the results of optical and electrical investigations. The most important results of this work, conclusions, suggestions of improvements and alternative designs are summarised in Chapter five.

Chapter 2

Theory

2.1 Electronic band structure of semiconductors

The most important semiconductors for electronic and optical applications are silicon and GaAs, respectively. Therefore the band structure of these two archetypical semiconductors well be briefly described here.

Silicon crystallizes in the diamond structure, which consists of two interpenetrating face-centered cubic lattices displaced from each other by one quarter of the body diagonal. GaAs crystallizes in the zinc-blende structure. In this lattice the atoms are arranged as in the diamond case but the two sub-lattices consist of Ga and As, respectively [16].

The energy band structure in semiconductors represents the relationship between the energy and crystal momentum of a charge carrier, which depends on the crystal structure, bond lengths between atoms and chemical species. The band structure is often quite complex, but it can be calculated using quantum mechanics. Fig. 2.1 shows the electronic band structure of the Si and GaAs.

In general, $E(k)$ has maxima or minima at the zone center and/or other symmetry points, but additional extrema may occur at the other points in the Brillouin zone. The energy gap E_G in a semiconductor is defined as the separation between the maximum of the valence band E_V and the minimum of the conduction band E_C. The valence band structure is for many semiconductors similar. Its maximum is situated in the center of the first Brillouin zone, in the point Γ at $k = 0$. The lowest point in the conduction band E_C of GaAs is situated also at the Γ point. Therefore the electronic transition between the initial and final states (having the same wave vector) can occur directly at $k = 0$. It is also called *direct band gap semiconductor*. In the case of Si, the conduction band minimum E_C is shifted towards the point X at the Brillouin zone boundary (along $\langle 001 \rangle$). Si is termed an *indirect band gap semiconductor*, because the initial and final states have different wave vectors.

Optical transitions conserve both energy and momentum. In direct gap GaAs, an excited electron at the bottom of the conduction band can relax spontaneously back into a hole in the valence band by emitting a photon at the band-gap energy with momentum conservation (the photon momentum is negligible with respect to the electronic one). This electron-hole radiative recombination process can only occur in Si with the assistance of a further process to conserve the momentum. This, in pure Si, occurs via the transfer of the electron momentum to a phonon that is created with equal and opposite wave vector to that of the initial state in the conduction band. Such a three-body process is quite inefficient compared with direct gap recombination. Thus, the probability of spontaneous

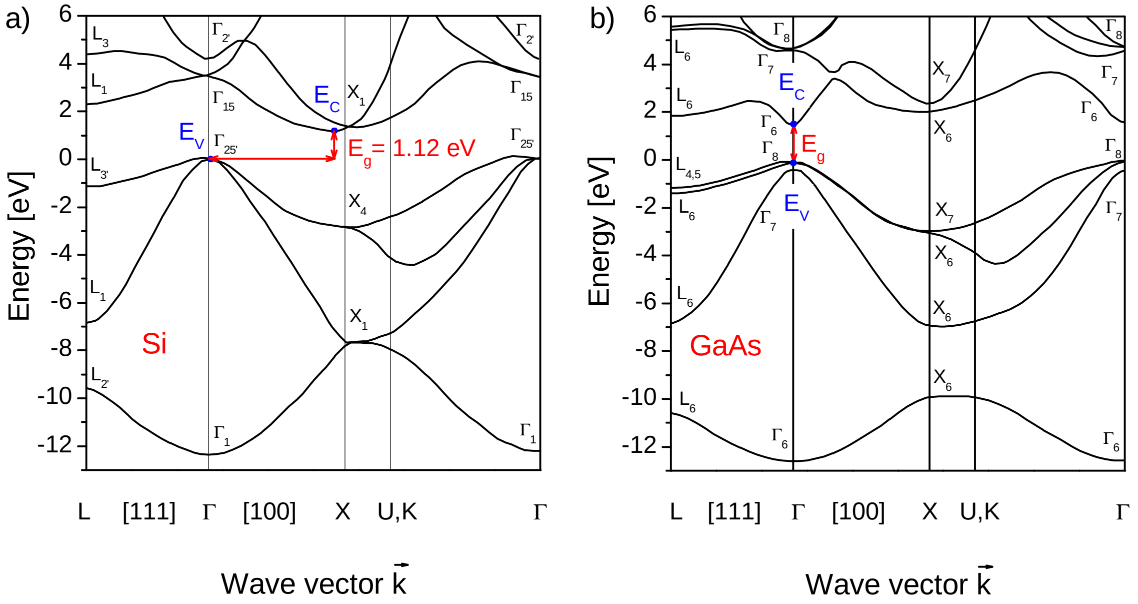

Figure 2.1: Calculated band structures of Si and GaAs [17]

emission is very low for Si and high for GaAs. Therefore the recombination radiative lifetime in Si is many orders of magnitude longer than in direct III-V semiconductors. During the relaxation of excited carriers, there is always a competition between the radiative and nonradiative processes. Because of the three-body process and long radiative lifetime in Si, the non-radiative recombinations are dominant. That is the reason for the very low luminescence efficiency in Si. However, when high purity and surface passivated Si is used, high luminescence efficiency can be achieved although still with a very long recombination time [4].

2.2 Light emitting diodes (LED)

Semiconductor light emitting devices can be classified into two basic categories: *light emitting diodes* (LEDs) that emit incoherent spontaneous light, and *laser diodes* emitting coherent radiation [18]. LEDs are among the most widely used semiconductor optoelectronic devices. They have a wide application field starting with simple indicator lamps to optical communication sources, from lighting lamps to elements for large color displays. Comparing to incandescent lamps, the LEDs are very compact, reliable and offer a relatively high efficiency, brightness and modulation bandwidth. Nowadays they are often replaced by semiconductor laser diodes, but the production of LEDs is much less complicated and therefore cheaper. Also in applications where the human eye is exposed to the light beam, in terms of safety and inconvenience of speckle typical for coherent light, the temporal and spatial incoherence of LEDs is more of an advantage than a disadvantage [18, 6].

2.2.1 History of LED

Henry Joseph Round of Marconi Labs first noted that a semiconductor junction would produce light from SiC crystallites already in 1907 [19] and is recognized as the discoverer of the phenomenon of electroluminescence.

Russian Oleg Vladimirovich Losev independently observed luminescence with SiC metal-semiconductor rectifiers [20–23] and his name is connected with the invention of the first LED.

Rubin Braunstein of the Radio Corporation of America reported on infrared emission from gallium arsenide (GaAs) and other semiconductor alloys in 1955 [24]. Biard and Pittman found in 1961 that gallium arsenide (GaAs) gave an infrared radiation when electric current was applied [25, 26]. They received the patent for the infrared LED and Texas Instruments marketed the first commercial LED product. In 1962 Nick Holonyak Jr. invented a method to synthesize gallium arsenide phosphide (GaAsP) crystals [27], which exhibited wavelengths in the visible spectrum. Using this tunable alloy, Holonyak crafted the first practical LED in 1962 (the red LED) and is seen as the father of the light-emitting diode.

The weak band-to-band emission from Si was first observed by Hayness and Briggs [28] using visible light excitation or by forward biasing Si diodes already in 1952.

In 1960s, Ralph Logan and his coworkers have pioneered on investigation of indirect band-gap GaP and GaAsP LEDs doped with optically active isoelectronic impurities (nitrogen) [6]. They developed a manufacturing process for GaP-based red and green LEDs. Simultaneously Maruska was working on the investigation of GaN films. In 1969 he succeeded to produce first single-crystal GaN film and in the early 1970s Pankove published a *metal* (In surface contact) - *insulator* (Zn doped n-GaN) - *semiconductor* (p-GaN) diode, which was the first current-injected GaN green and blue (475 nm) light emitter [29]. Two years later Maruska has developed Mg-doped GaN MIS device emitting violet luminescence [30].

In 1990s, Shuji Nakamura demonstrated the first high-brightness blue LED based on GaInN. He proposed that blue LEDs in combination with phosphor coating (yellow light) produce light that appears white. Nakamura was awarded the 2006 Millennium Technology Prize for his invention of inventions of blue, green and white light-emitting diodes (LEDs) and the blue laser diode [31–36].

Conventional LEDs are made from a variety of inorganic semiconductor materials, producing the following colors:

Semiconductor	Substrate	Colour	λ [nm]	η_{ext} [%]
GaAs	GaAs	infrared	870 - 900	10
AlGaAs	GaAs	red and IR	640 - 870	10
AlGaAsP	GaAs	red	650 - 670	
AlGaInP	GaAs	red - orange	610 - 617	1 - 10
		yellow	590	
		yellow - green	573	
InGaAsP	InP	IR	1000 - 1600	1 - 10
GaAsP	GaP	orangish yellow	560 - 700	< 1
	GaAs	red - IR	630 - 870	< 1
GaP	GaP	red - orange	700	2 - 3
GaP:N	GaP	green	550 - 560	< 1
Nitrides:				
GaN/AlGaN	Al_2O_3	blue	405	
AlN, AlGaN, AlGaInN		near - deep UV	210 nm - 375 nm	

Semiconductor	Substrate	Colour	λ [nm]	η_{ext} [%]
InGaN	GaN, SiC	blue green	430 - 460 500 - 530	2 3

With this wide variety of colors, arrays of multicolor LEDs can be designed to produce unconventional color patterns.

2.2.2 Mechanisms of light emission

The light emission from a semiconductor is based on three processes. The first is the electron-hole pair formation, the excitation process. The second process is recombination, where the excited carriers give up their energy either through a radiative or a nonradiative process. The third process is the extraction of emitted photons from the active region of the semiconductor. The overall efficiency of the LED is the result of the efficiencies of each of these processes.

Excitation mechanisms

Electron excitation is the transition of an electron to a higher energy state. Two convenient ways of achieving excitation are photoexcitation and electrical excitation. In the process of photoexcitation the electron absorbs a photon from an external light source and gains all the photon's energy. In the case of the electrical excitation the electron gains energy from the injected electrical current (charge carriers). Within a semiconductor crystal lattice, thermal excitation is a process where lattice vibrations provide enough energy to move electrons to a higher energy band.

Recombination of excess carriers

After a certain time the system relaxes to a lower energy state by electron-hole (e-h) recombination.

In semiconductors, there are two competitive processes of recombination of electrons and holes as shown in Fig. 2.2. The radiative recombination is accompanied by the emission of a photon with energy equal to the bandgap energy of the semiconductor (Fig. 2.2(a)). In light-emitting devices is this clearly the preferred process. However, non-radiative recombination (Fig. 2.2(b)) can never be reduced to zero. The maximation of the radiative process and the minimation of the non-radiative process can be attained in a number of ways. Figure 2.3 illustrates the important radiative *(a)* and nonradiative *(b)* transitions in a semiconductor. The path *(1)* from the radiative transitions depicts the intrinsic band-to-band transition involving the recombination of an electron-hole pair. This process has a high probability of occurrence only in semiconductors with a direct band gap. Path *(2)* shows an extrinsic recombination between a hole bound to a neutral acceptor and a free electron in the conduction band. Path *(3)* demonstrates the exciton recombination involving an acceptor-type trap. A typical example, where this type of recombination occurs is GaP doped with isovalent nitrogen. When a P atom is replaced by an N atom in GaP, it creates an acceptor-type trap level in the band gap very close to the conduction band edge E_C. This level captures an electron from the conduction band and becomes negatively charged. Subsequently, through Coloumbic attraction, a hole from the valence band gets bound to the trap level, and the electron-hole pair remaining in the excited state is known as a *bound exciton*. The pair then recombines by emitting a

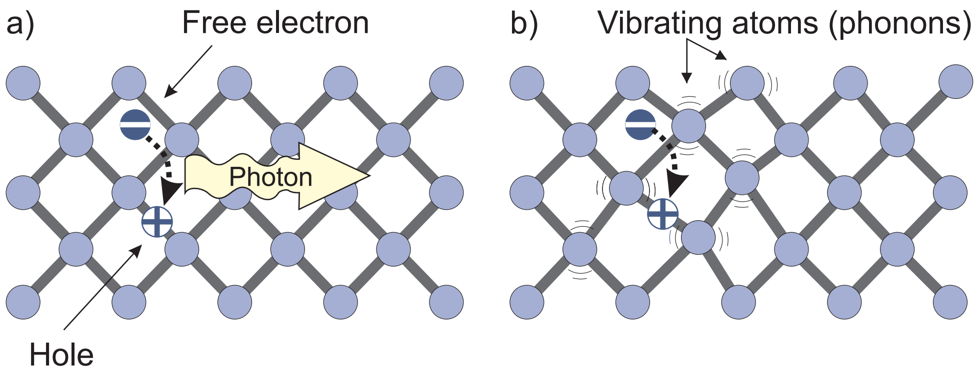

Figure 2.2: (a) Radiative recombination of electron-hole pairs accompanied by an emission of photons with an energy $h\nu \approx E_g$. (b) In non-radiative recombination events the energy is converted to phonons.

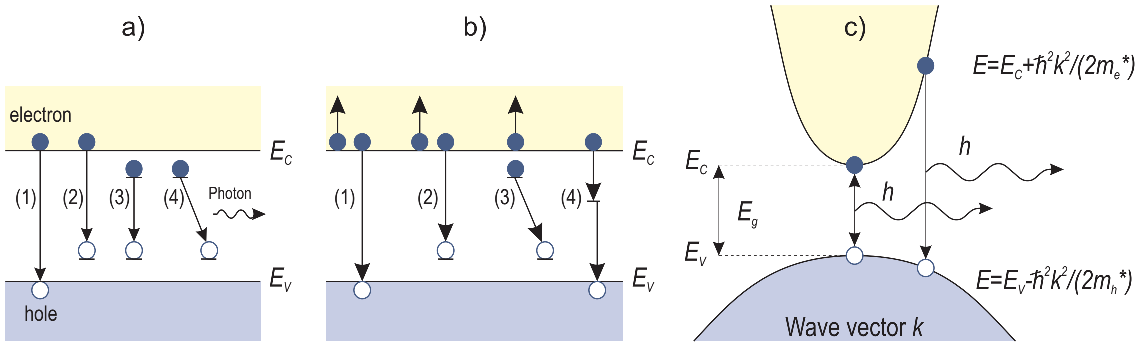

Figure 2.3: Schematic illustration of possible vertical electron-hole (a) radiative and (b) nonradiative transitions in semiconductors. (c) Parabolic electron and hole dispersion relations.

photon. Path *(4)* shows the extrinsic process of donor-acceptor pair recombination. An ionized donor captures an electron from the conduction band and a hole is trapped by the ionized acceptor. By the recombination of electron-hole pair in the acceptor state there is a photon emitted with energy equal to difference between the two energy levels [18].

During non-radiative recombination, the electron energy is converted to vibrational energy of lattice atoms, i.e. phonons (Figure 2.2(b)). Thus, the electron energy is converted to heat. For obvious reasons, non-radiative recombination events are unwanted in light-emitting devices. An important non-radiative recombination mechanism is **Auger recombination**. In this process the energy becoming available though electron-hole recombination (approximately E_g), is dissipated by an excitation of a free electron high into the conduction band, or by a hole deeply excited into the valence band. The highly excited carriers subsequently lose energy by multiple phonon emission until they are close to the band edge. Auger recombination reduces the luminescence efficiency in semiconductors only at very high excitation intensities or at very high carrier injection currents. This is due to the cubic carrier concentration dependence. The numerical values of Auger recombination can be determined by a quantum mechanical calculation that takes into account the band structure of semiconductor. Path *(1)* in Figure 2.3*b* represents the band-to-band Auger recombination involving two electrons and one hole (eeh process).

Trap-assisted Auger recombination can also occur. Path *(2)* depicts an Auger transition involving two free electrons and a trapped hole. In path *(3)* is shown donor-acceptor pair and a free electron. Finally, path *(4)* illustrates the non-radiative recombination process via **deep-level recombination centers**, which are crystal defects like foreign atoms, native defects and dislocations. All such defects have energy level structures, that are different from substitutional impurity atoms. Thus they form one or several energy levels within the forbidden gap of the semiconductor, which are very effective recombination centers. The recombination of free carriers via deep levels was first analyzed by Shockley, Read and Hall [37, 38].

Figure 2.3 (c) illustrates e-h recombination process in a direct bandgap semiconductor. Electrons in the conduction band and holes in valence band are assumed to have the parabolic dispersion relations

$$E_e = E_C + \frac{\hbar^2 \mathbf{k}^2}{2m_e^*} \quad \text{and} \quad E_h = E_V - \frac{\hbar^2 \mathbf{k}^2}{2m_h^*} \tag{2.1}$$

for electrons and holes, respectively. In these equations m_e^* and m_h^* are the electron and hole effective masses, $\hbar$ is the Planck's constant divided by 2π, $\mathbf{k}$ is the carrier wavevector, and E_V and E_C are the valence and conduction band edges, respectively.

In a thermel equilibrium is the kinetic energy of the electron $E_{kin} = \frac{1}{2}mv^2$ equal to the thermal energy $E_{th} = kT$ [39]. A carrier with an energy kT and effective mass m^* has the momentum

$$p_{carrier} = m^* v = \sqrt{2m^* \frac{1}{2} m^* v^2} = \sqrt{2m^* kT}. \tag{2.2}$$

The momentum of a photon with energy E_g can be derived from the de Broglie relation

$$p_{photon} = \hbar k = h\nu / c = E_g / c \tag{2.3}$$

The carrier momentum $p_{carrier}$ is orders of magnitude larger than the photon momentum p_{photon}. Therefore the electron momentum cannot change significantly during the transition from the conduction to the valence band. The electrons only recombine with holes that have the same momentum or k value (fig. 2.3 (c)).

Electrons and holes have Fermi-Dirac distribution and average energy of kT. For high temperatures and not too high doping one can use an approximation in the form of Boltzmann distribution. Energy conservation requires that the photon energy is given by the difference electron and hole energy. Using the requirement that the electron and hole have the same momentum, the photon energy can be written as the joint dispersion relation

$$h\nu = E_e - E_h = E_g + \frac{\hbar^2 k^2}{2m_r^*}, \qquad \text{where} \qquad \frac{1}{m_r^*} = \frac{1}{m_e^*} + \frac{1}{m_h^*}, \tag{2.4}$$

where m_r^* is the reduced mass. If the thermal energy is much smaller than the bandgap energy, $kT << E_g$, the photon energy $h\nu$ is approximately equal to the bandgap energy E_g.

From the eq. 2.4 the joint density of states $\rho(E)$ can be calculated [6]

$$\rho(E) = \frac{1}{2\pi^2} \left(\frac{2m_r^*}{\hbar^2} \right)^{2/3} \sqrt{E - E_g}. \tag{2.5}$$

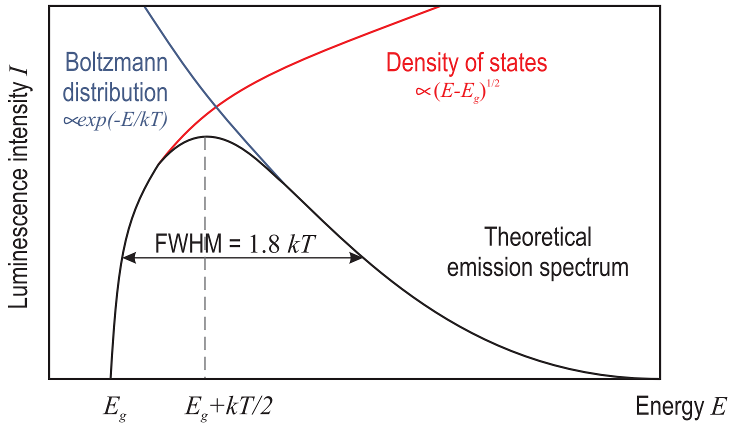

Figure 2.4: Theoretical emission curve of an LED.

In the allowed bands are the carriers distributed by Boltzmann distribution $e^{-E/kT}$. The emission lineshape is proportional to the product of joint density of states and the Boltzmann factor (Fig. 2.4)

$$I(E) \propto \sqrt{E - E_g} e^{-E/kT}, \quad \text{with maximum at} \quad E = E_g + \frac{1}{2}kT. \tag{2.6}$$

Extraction of light from the semiconductor

In a typical LED, photons are generated within of few μm around about the pn-junction depth, and the emitted light must pass through the semiconductor to reach the surface from where it is emitted to reach the observer's eye. Although the internal power conversion efficiency of high quality semiconductor diodes can reach the values close to 100%, the external power efficiency (internal efficiency multiplied by the light extraction efficiency from the emitting semiconductor into air) is rather poor (Figure 2.5). There are three loss mechanisms that reduce the amount of light reaching the observer. Firstly, the optical absorption coefficient α of the semiconductor decreases the amount of light with the distance x from the junction as $exp(-\alpha x)$. Secondly, the point source emits isotropically, with uniform power density in all directions, but only rays with the angle $\theta < \theta_c$ (critical angle for total internal reflection) can escape from the semiconductor into air, whereby θ_c is:

$$sin\theta_c = \frac{n_{air}}{n_S} \tag{2.7}$$

where n_S and n_{air} are the refractive indices of the semiconductor and air, respectively. For small values of critical angle $\theta_c \approx 1/n_S$. The solid angle Ω (Fig. 2.5) of the cone corresponding to those escaping rays is given by:

$$\Omega = 2\pi\left(1 - cos\theta_c\right) \approx \frac{\pi}{n_S^2} \tag{2.8}$$

The third loss is due to the partial reflection at the semiconductor/air interface, which is the reason why the rays cannot fully escape from the extraction cone (Fresnel loss). The extraction efficiency is limited to:

$$\eta_{extraction} \leq \frac{n_{air}^2}{4n_S^2} \tag{2.9}$$

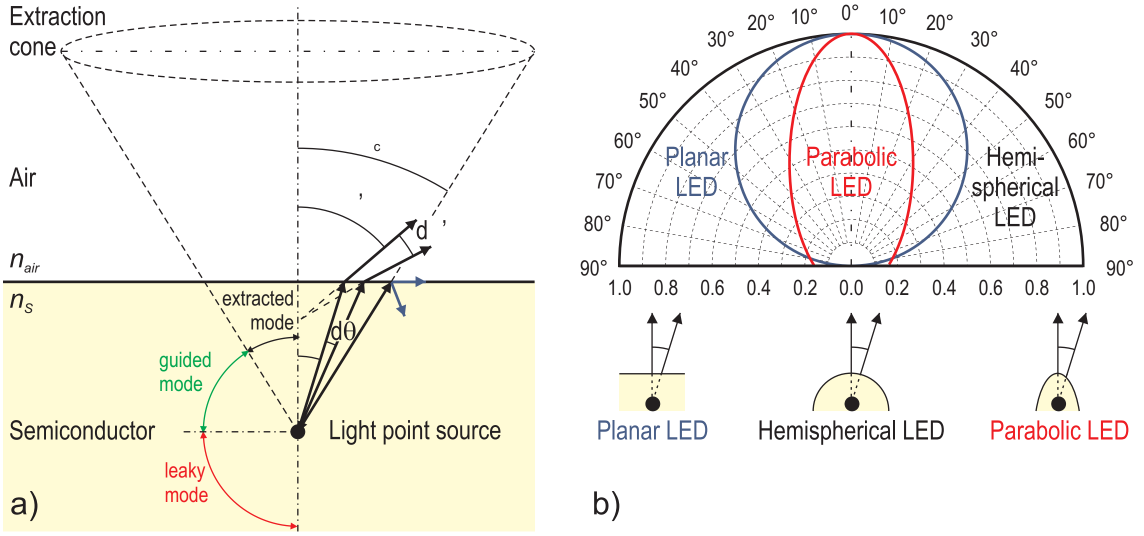

Figure 2.5: (a) Refraction of light rays from a point source at a semiconductor-air interface, showing the extraction cone. (b) Far-field emission patterns of LEDs with different surface shapes: planar LED, hemispherical LED and parabolic LED.

The escape problem is significant for high efficiency of LEDs. In most semiconductors, the refractive index is quite high and thus only a a few percent of generated light can escape. In reality this means that the critical angle of high index semiconductor ($n_S \approx 3$) containing the pn-junction in which light is generated is only $\theta_c \approx 20°$. Extraction efficiency at a single planar face for an isotropic emitter into the surrounding air is typically only $\eta_{extraction} \leq 2-3\%$.

High contrast between the refractive indices of semiconductor and surrounding ambient (air) leads to an non-isotropic emission pattern. For high index LEDs with a planar surface, a lambertian emission pattern is obtained

$$I_{air} = \frac{P_{source}}{4\pi r^2}\frac{n_{air}^2}{n_S^2}cos\Phi, \tag{2.10}$$

where P_{source} is total power source and r is the distance from the light source. The lambertian emission pattern follows a cosine low, with the highest intensity at $\Phi = 0°$. In this equation, Fresnel reflection losses at the semiconductor-air interface have been neglected, which must be taken into the account in a rigorous calculation. At normal incidence the Fresnel power transmittance is given by

$$T = 1 - R = 1 - \left(\frac{n_S - n_{air}}{n_S + n_{air}}\right)^2 = \frac{4n_S n_{air}}{(n_S + n_{air})^2}. \tag{2.11}$$

Fig. 2.5 (b) shows emission patterns of LEDs with different surface shapes. A planar LED has a lambertian emission profile. An isotropic emission pattern is obtained for hemispherically shaped LEDs, which have the light emitting region in the center of the sphere. A strongly directed emission pattern can be obtained for parabolically shaped LEDs. However, both hemispherical as well as parabolic surfaces are difficult to fabricate.

A common industrial solution to the low efficiency issue is to embed the semiconductor chip in a transparent plastic (epoxy) with a dome shape (Figure 2.6). Since the refractive index of the plastic is higher than that of air, the extraction cone in the semiconductor

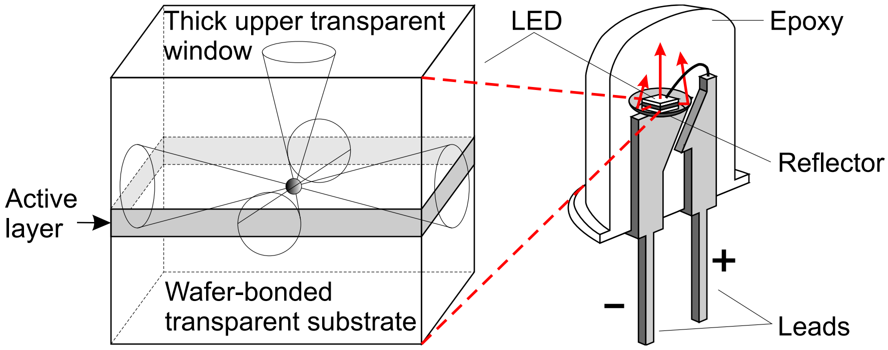

Figure 2.6: Side collection of light in high-brightness LEDs. A thick transparent layer covers an active layer, which has been lifted of from its substrate and bonded to a nonepitaxial transparent conducting substrate [41].

is larger and therefore also the extraction efficiency increases. The reason for dome-shaping of the plastics is that the rays hit the plastics-air interface at close to normal angles. In order to increase the number of extracted photons, it is convenient to apply a transparent layer also at the bottom of the active region, to evoke the so-called 'photon recycling' phenomenon [40]. This step implies a costly removal of the substrate, in which the light is absorbed, and bonding to a transparent substrate. Light is extracted from all six sides of the chip. It is collected and collimated by curved mirrors, possibly in a combination with a lens. The transparent substrate approach has led to devices with external quantum efficiencies of 20-40%. Since the light is escaping from all sides with a more or less Lambertian radiation profile, the brightness cannot be actually very high. This means, it is difficult to focus the beam into a small spot or couple it into an optical system with limited numerical aperture. The transparent substrate approach is also not suitable for array devices. Other way to raise the excitation efficiency rest on the principle of randomising the photon direction until an angle $\theta < \theta_c$ is found. For this purpose, one may use optically rough interfaces [42]. By nanotexturing the thin film surface, the light ray dynamics becomes chaotic, and the optical phase-space distribution becomes ergodic, allowing even more of the light to find the escape cone. Recycling phenomena are not exclusive of resonant microcavity effects (closely explained in further the Sec. 2.4) since both can be combined to further increase device performances. An increase of the external efficiency of factor of three in GaAs LEDs by employing these principles have been demonstrated [42].

2.2.3 Electrical properties of LED

A light emitting diode (LED) is essentially a pn-junction diode typically made from a direct bandgap semiconductor, in which the electron-hole pair recombination results in the emission of a photon. The emitted photon energy is therefore approximately equal to the bandgap energy $h\nu \approx E_g$.

When dissimilar doped materials are placed in contact with each other, the flow of current in the region of the junction is different than it is in either of the two materials alone. Current will readily flow in one direction across the junction, but not in the other, constituting the basic diode configuration. This behavior can be understood in terms of the movement of electrons and holes in the two material types and across the junction.

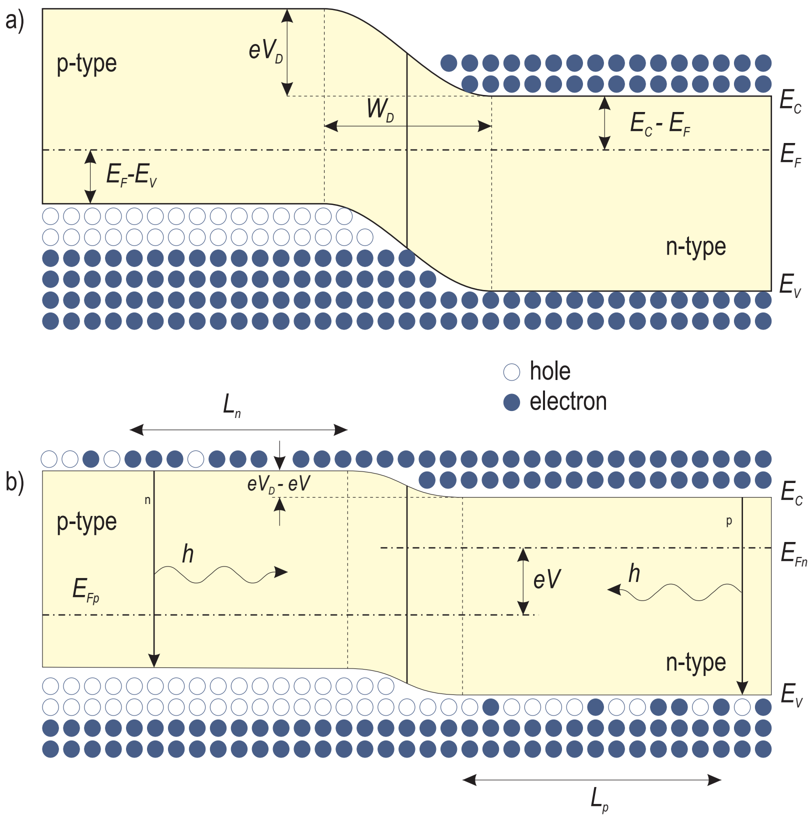

Figure 2.7: Distribution of carriers in a pn-homojunction under (a) zero bias and (b) forward bias [6].

pn-homojunction diodes

pn-junctions consisting of a single material are called *pn-homojunctions*. Let's consider an abrupt pn-homojunction. All dopants are assumed to be fully ionized. The electron concentration is given by a donor concentration $n = N_D$. The concentration of free holes is given by an acceptor concentration $p = N_A$. It is further assumed that no compensation of dopants occurs by unintentional impurities and defects. Fig. 2.7 shows the energy bandgap diagram of an *a)* unbiased pn-junction device and *b)* the device under the forward bias. The band diagram in fig. 2.7 *a)* is drawn to keep the Fermi level uniform throughout the device, what is a requirement of equilibrium.

The free electrons in the n-type material tend to move from the negatively doped area to a positively doped (p-type) area. The result of this migration is that the holes appear to move in the opposite direction, or away from the p-type region and toward the n-type area. Electrons from the n-type region and holes from the p-type region recombine in the vicinity of the junction to form a *depletion zone* W_D, in which no charge carriers remain. In the depletion zone, a static charge is established that inhibits any additional electron transfer, and no appreciable charge can flow across the junction unless assisted by an external bias voltage (Fig. 2.7).

The only charge in the depletion region comes from ionised donors and acceptors, which form a space charge region on the n-type and p-type side, respectively. The space charge region produces a potential - *diffusion voltage* V_D (Fig. 2.7). It represents a barrier that the free carriers must overcome in order to reach the neutral region of opposite conductivity type.

$$V_D = \frac{kT}{e} ln \frac{N_A N_D}{n_i^2}, \tag{2.12}$$

where n_i^2 is the intrinsic carrier concentration of the semiconductor.

The *width of depletion region* as a dependence of the diffusion voltage can be derived via Poisson's equation

$$W_D = \sqrt{\frac{2\epsilon}{e}(V - V_D)\left(\frac{1}{N_A} + \frac{1}{N_D}\right)}, \tag{2.13}$$

where $\epsilon = \epsilon_r \epsilon_0$ is the dielectric permittivity of the semiconductor and V is the diode bias voltage.

The diffusion constants of carriers is difficult to measure. Usually the carrier mobility, for example using the Hall effect, is measured. Using Einstein relation, the diffusion constants can be calculated from the carrier mobility:

$$D_n = \frac{kT}{e}\mu_n \qquad \text{and} \qquad D_p = \frac{kT}{e}\mu_p. \tag{2.14}$$

Carriers in an intrinsic semiconductor, without applied external electric field, propagate by diffusion. If the carriers are injected into a region with opposite conductivity, the minority carriers will eventually recombine. The depth of diffusion without recombination of carriers is called *diffusion length.* The diffusion length is given by

$$L_n = \sqrt{D_n \tau_n} \qquad \text{and} \qquad L_p = \sqrt{D_p \tau_p}, \tag{2.15}$$

for electrons and holes, respectively. The values τ_n and τ_p are the electron and hole minority carrier lifetimes. In typical semiconductors, the diffusion length is in the range of several micrometers and the minority carrier lifetime in order of some tens or hundreds of nanoseconds. A disadvantage of pn-homojunctions is that the minority carriers are distributed over a large distance and their concentration decreases as they diffuse further into the adjacent region.

The depletion region is highly resistive due to the fact that it is depleted of free carriers. An external bias therefore decreases or increases the pn-junction barrier for forward or reverse bias, respectively.

Under *forward bias* conditions, electrons and holes are injected into the region with opposite conductivity type and the current flow increases. The carriers diffuse into the region with opposite conductivity type where they eventually recombine, thereby emitting a photon.

If the circuit polarity is reversed with respect to the p-type and n-type regions, electrons and holes will be pulled in opposite directions, with an accompanying widening of the depletion region at the junction. No continuous current flow occurs in a *reverse-biased* pn-junction, although initially a transient current will flow as the electrons and holes are pulled away from the junction. Current flow will cease as soon as the growing depletion zone creates a potential that is equal to the applied voltage.

Current-voltage $(I - V)$ diode characteristics

According to [6] the current-voltage $(I - V)$ characteristics of the pn-junctions are described by the Shockley equation for a diode with cross-sectional area A as followed

$$I = eA\left(\sqrt{\frac{D_p}{\tau_p}}\frac{n_i^2}{N_D} + \sqrt{\frac{D_n}{\tau_n}}\frac{n_i^2}{N_A}\right)\left(e^{eV/kT} - 1\right), \tag{2.16}$$

where $D_{n,p}$ and $\tau_{n,p}$ are the electron and hole diffusion constants and minority carrier lifetimes, respectively.

Under reverse bias conditions, the diode current saturates and the saturation is given by the factor preceding the exponential function in the Shockley equation. Under typical forward bias conditions, the diode voltage $V >> kT/e$ and thus $[exp(eV/kT) - 1] \approx exp(eV/kT)$. Using Eq. 2.12

$$I = eA\left(\sqrt{\frac{D_p}{\tau_p}}N_A + \sqrt{\frac{D_n}{\tau_n}}N_D\right)e^{e(V-V_D)/kT}. \tag{2.17}$$

The current strongly increases as the forward diode voltage reaches the diffusion voltage $V \approx V_D$. It is also called *threshold voltage* V_{th}. In highly doped semiconductors, the separation between the band edges and the Fermi level is small compared with the bandgap energy $E_C - E_F$ and $E_F - E_V << E_g$. In this case the diffusion voltage can be approximated by the bandgap energy divided by the elementary charge [6]

$$V_{th} \approx V_D \approx E_g/e. \tag{2.18}$$

Fig. 2.8 shows the forward current-voltage characteristics of pn-junctions of different semiconductor materials at room temperature. The experimental threshold voltages shown in the figure agree well with the bandgap energy E_g.

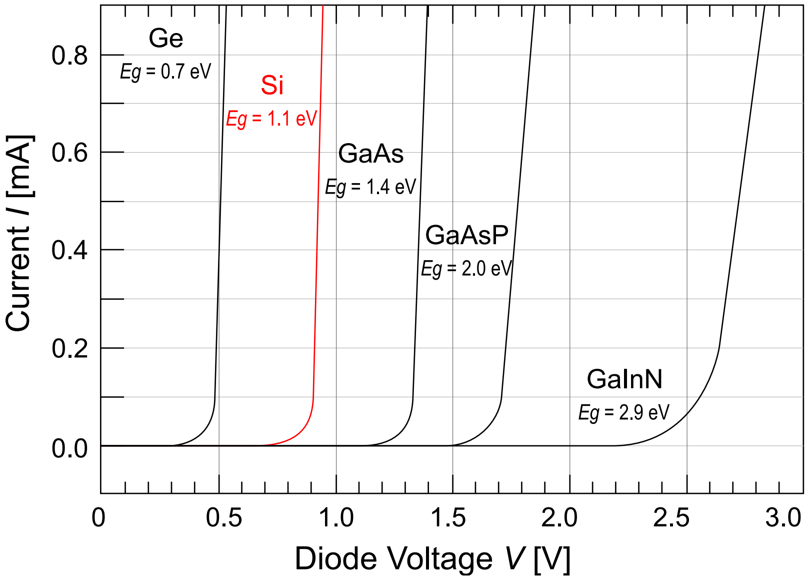

Figure 2.8: Forward current-voltage characteristics of pn-junctions of different semiconductors at the room temperature [6].

Deviations from the ideal $I - V$ curve

The theoretical $I - V$ characteristics are described by the Shockley equation 2.16, which is for the experimentally measured values used in the following form:

$$I = I_s e^{eV/(n_{ideal})kT}, \tag{2.19}$$

where n_{ideal} is the *ideality factor* of the diode. An ideality factor of $n_{ideal} = 1.0$ stands for perfect diodes. Typical value of Si-LEDs are $n_{ideal} = 1.1 - 1.5$, the arsenide and phosphide diodes have $n_{ideal} = 2.0$ and a value of $n_{ideal} = 6.0$ has been found for the GaN/GaInN diodes.

Every real diode has some parasitic resistances. The series and parallel resistance are shown in fig. 2.9. A series resistance R_s can be caused by contact resistance or by the resistance of the neutral diode regions. The reason for the parallel resistance R_p can be any leakage channel that bypasses the pn-junction, caused by damage or by surface imperfections. In order to take into account these parasitic resistances, the Shockley equation for forward biased pn-junction has to be modified:

$$I - \frac{V - IR_s}{R_p} = I_s e^{e(V-IR_s)/(n_{ideal})kT}, \tag{2.20}$$

If the parallel resistance goes to infinity and the series resistance to zero, this equation is reduced to the Shockley equation. The parallel resistance can be evaluated near the origin of the $I - V$ diagram, at $V << E_g/e$, where the pn-junction current can be neglected. The series resistance is evaluated at a high voltage, where $V > E_g/e$. For sufficiently large voltages, the diode characteristics become linear due to the series resistance.

Reasonable real diodes have much higher parallel resistance $R_p \rightarrow \infty$ than the series resistance. Then Eq. 2.20 can be written as

$$I = I_s e^{e(V-IR_s)/(n_{ideal})kT}, \tag{2.21}$$

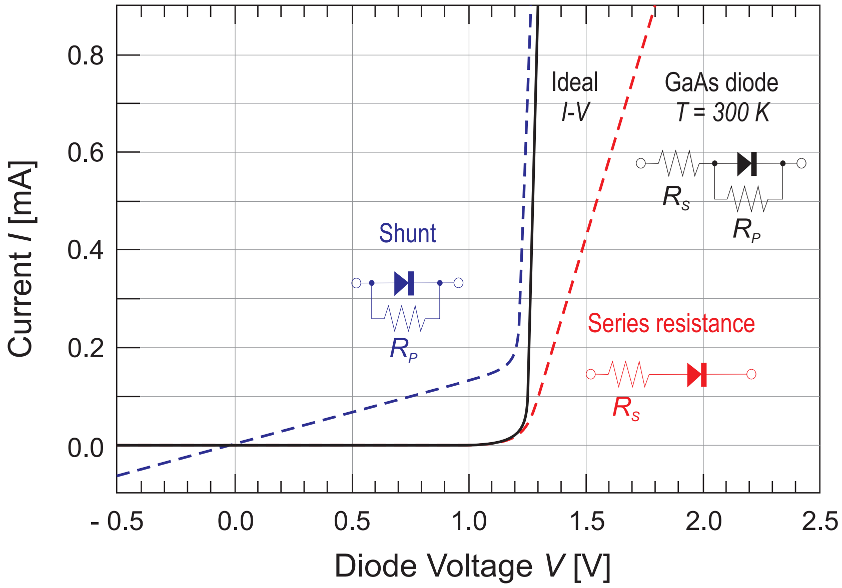

Figure 2.9: Effect of a series resistance and a parallel resistance (shunt) in the $I - V$ characteristic of a pn-junction diode.

Solving the equation for V, differentiating V with respect to I and followed multiplication by I allows one to identify the series resistance of the diode as the slope of IdV/dI versus the diode current I:

$$I\frac{dV}{dI} = R_s I + \frac{n_{ideal}kT}{e}. \tag{2.22}$$

2.2.4 LED efficiency

Internal quantum efficiency

The internal quantum efficiency η_{int} gauges what fraction of e-h recombinations in the forward biased pn-junction are radiative and therefore lead to photon emission. Nonradiative transitions are those in which e-h recombine through a recombination center such as a crystal defect or an impurity and emit phonons (lattice vibrations). By definition,

$$\eta_{int} = \frac{\text{Rate of radiative recombination}}{\text{Total rate of recombination}} = \frac{\frac{1}{\tau_r}}{\frac{1}{\tau_r} + \frac{1}{\tau_{nr}}}, \tag{2.23}$$

where τ_r is the mean lifetime of a minority carrier before the radiative recombination and τ_{nr} the mean lifetime before they recombine via a recombination center without emitting a photon. The total current I is determined by the total rate of recombinations whereas the number of photons emitted per second Φ_{ph} is determined by the rate of radiative recombinations.

$$\eta_{int} = \frac{\text{Photons emitted per second}}{\text{Electrons injected per second}} = \frac{\Phi_{ph}}{I/e} = \frac{P_{opt(int)}/h\nu}{I/e}, \tag{2.24}$$

where $P_{opt(int)}$ is the optical power generated internally.

Extraction efficiency

The extraction efficiency $\eta_{extraction}$ is defined as a ratio between photons emitted into the free space and photons emitted by the active region. In a real diode the extraction efficiency never reaches unity. There are many factors having an influence on photon emission into the free space (see Sec. 2.2.2). For example the reabsorption of the photon by the substrate or by the metallic contact. Also the phenomenon of total internal reflection, also referred to as the trapped light phenomenon reduces the ability of the light to escape from the semiconductor. The extraction efficiency is defined by

$$\eta_{extraction} = \frac{\text{Photons emitted into free space per second}}{\text{Photons emitted from active region per second}} = \frac{P_{opt}/h\nu}{P_{opt(int)}/h\nu}, \tag{2.25}$$

where P_{opt} is the optical power emitted into free space.

External quantum efficiency

The external quantum efficiency η_{ext} gives the ratio of the number of useful photons to the number of injected charge carriers.

$$\eta_{ext} = \frac{\text{Photons emitted into free space per second}}{\text{Electrons injected into LED per second}} = \frac{P_{opt}/(h\nu)}{I/e} = \eta_{int}\eta_{extraction}. \tag{2.26}$$

Power efficiency

Power efficiency η_{power} is defined by

$$\eta_{power} = \frac{\text{Optical power output}}{\text{Electrical power input}} = \frac{P_{opt}}{IV}, \tag{2.27}$$

where IV is the electrical power applied to the LED.

2.3 Si based light emitters

The indirect band gap of Si is 1.12 eV at room temperature. The weak band-to-band emission at this energy was first observed by Haynes and Briggs [28] using visible light excitation or by forward biasing Si diodes. A review of the work on intrinsic and extrinsic radiative recombination in Si has been given by Davies [43].

Electron-hole pairs created either optically or electrically may bind to each other to form excitons. Exciton recombination dominates the optical emission process at low temperatures and is characterized by very narrow emission lines. At high temperatures the excitons are thermally dissociated. The emission is due to band-to-band recombination [17].

There are various attempts, how to overcome the indirect band-gap limitations in light emission from Si.

- Increasing of the luminescence efficiency by increasing the overlap of the electron and hole wave functions via quantum confinement and band structure engineering or by spatially confining the exciton in a defect-free region so that the nonradiative recombination lifetime becomes very long. Research on the quantum confinement of carriers in Si-based nanostructures including porous silicon (PS), nanoclusters, quantum wells (e.g. Si/SiGe), nanowires and nanodots forms a large part of the work on light emission in Si. Reduced size of quantum dot structures gives rise to spread in momentum leading to augmentation of "quasi direct no-phonon" process.

- Inducing recombination at impurity centers. Introduction of rare earths (mostly Er) in SiO_2 and Silicon rich oxides in MOS structures shows improved performance. Rare earth impurities like Er, Nd, and Pr in the pn-junctions of Si have also yielded significant increase in the efficiency and power output.
- Intraband transitions, where the indirect band-gap of Si does not play any role (e.g. transitions between quantum confined states within the valence or conduction band).

Porous Si (PS)

PS has created some sensation in the early 1990s. The PS network is usually created by an anodic wet chemical etching process [44]. Many publications, articles and books [45–52] have been written about PS, which exhibit the maximum of PL intensity at various photon energies from blue 3 eV [50–52] up to near infrared 0.8 eV [47] with room temperature PL external quantum efficiency between 1% and 10%. The efficient PL is a direct result of the small width of Si pillars, which are only few nanometers small. Quantum confinement of the excited carriers results in an effective enlargement of Si band-gap. The probability of recombination increases. The localisation of the carriers prevents their diffusion to possible nonradiative recombination centers, thus the chances of radiative transitions increase. The first electroluminescent PS device was demonstrated by Richter [53] (5 mA, 200 V). Considerable progress in the fabrication of EL porous silicon LEDs made Gelloz and Koshida [54]. They have produced devices with RT external quantum efficiency approaching 1% for an applied bias 5 V, although the exact nature of the carrier excitation process is not known. In 2001 have Chan and Fauchet demonstrated the all-silicon microcavity light emitting devices made of a thin, high-porosity porous silicon active layer sandwiched between two Bragg reflectors made of several pairs of low index/high index of refraction porous silicon layers of lower porosities [55]. The problem of PS is the high sensitivity of the electro-optical properties to the etching parameters and subsequent treatment. The layers of PS are inhomogenous, obtaining mix of Si wires, nanocrystals and amorphous Si material, what causes difficulties by analyzing their optical properties. PS is also not an attractive solution as it is not compatible with standard Si microfabrication technology.

Si nanocrystals (Si-nc)

Si-nc are usually embedded in a SiO_2 matrix in order to exploit the quality and stability of the SiO_2 /Si-nc interface and to improve emission properties of quantum confined Si. There are many different approaches, how to fabricate Si-nc. The most widely used are deposition of SiO_X films or Si implantation into SiO_2 , followed by high temperature annealing, which causes a phase separation of SiO_x into Si-nc and SiO_2 .

Devices in which the optically active medium is insulating (as in the case of SiO_2) would seem incompatible with electrical excitation. Nevertheless, by utilisation of current tunneling between the embedded nanocrystals, efficient electroluminescence has been demonstrated [56].

In 2000 a breaking work of Lorenzo Pavesi about the evidence for optical gain in silicon nanocrystals that were produced by implanting silicon in SiO_2 grown on silicon wafers was published in Nature [57]. In this work, 3 nm silicon nanocrystals luminescent in the near infrared around 1.5 eV were inserted into a crude waveguide structure. The light, emitted by the material, was amplified as it traveled along the waveguide. Net modal gains between 10 and 100 cm^{-1} were measured using the variable stripe length (VSL) method. Although gain has been independently reported by other groups [57–63], several important questions remain unresolved. It is not clear why no gain is observed in some studies [64, 65] or why groups that do observe gain report that only a fraction of the samples yield gain. The differences may be due to the use of different samples or experimental conditions as well as measurement setup or pump fluence.

Rare earths in SiO_2

Many researchers have investigated MOS structures doped with different rare earths. It was shown that MOS structures incorporating different rare earths can emit light with different colour related to their specific energy level structure [66, 67]. There have been demonstrated MOS based light emitting diodes (MOSLEDs) doped with Er^{3+}, Tb^{3+}, Ce^{3+}, or Gd^{3+} emitting in the infrared, green, blue, and ultraviolet spectral ranges, respectively [68–71]. These MOSLEDs typically reach external quantum efficiencies between 1% and 10%. Even a switchable two-color MOSLED doped with Eu has been developed and published [72]. This device takes an advantage of the fact that Eu occurs in the two oxidation states Eu^{3+} and Eu^{2+}. The electroluminescence EL can be switched with the excitation current between red low current and blue high current, ascribed to electronic transitions in tri- and divalent Eu ions, respectively. The disadvantage of MOSLEDs is that in order to get a relatively efficient electoluminescence very high voltages (about 100 V) are necessary and the device lifetime is rather short.

Silicon nanocrystals and Erbium in SiO_2

An important experimental finding is a strong enhancement of the Er luminescence in a SiO_2 matrix containing nanocrystals (NC). Thus the Si NCs act as sensitizers for the Er luminescence, i.e. there is an efficient energy transfer form the NCs to the Er ions. This has been clearly shown for photoexcitation, but also reported for electric excitation in some cases [17].

Quantum efficiencies of 1-10% have been demonstrated, yet with low stability of the devices [73–80]. The stability (lifetime) can be enhanced by increasing the Si content, which leads also to lower operating voltages (under these conditions amorphous Si clusters are formed). However, the efficiency decreases under these conditions, so there appears to be a trade-off between stability and efficiency.

Raman laser

An alternative path has been followed by the development of a continuous wave Raman laser in 2005 [81–84]. Stimulated Raman scattering in silicon has been observed by launching intense pump beam at 1540 nm into the Si core of a Silicon-On-Insulator waveguide. The Stokes wave at 1540 nm, amplified by high power pump beam, is reflected back and forth by two mirrors resulting in self sustained oscillation. The detrimental effect of

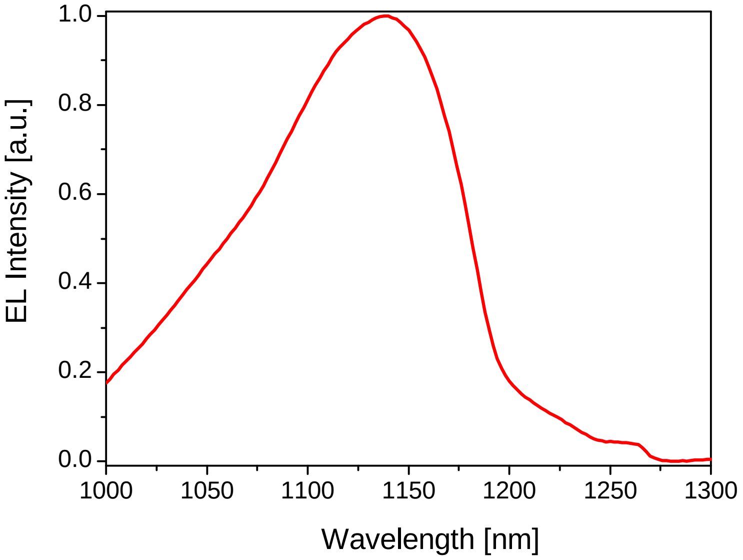

Figure 2.10: EL spectra at 300 K from silicon pn diodes prepared by B^+ implantation into n-type silicon at 25 keV with doses of $4x10^{15}$ [89].

loss by free carrier absorption by electron-hole pairs generated by two-photon absorption is eliminated by a bias applied to a lateral p-i-n structure. The drawbacks of the device are large device length, optical pumping and difficulty in modulating by electrical means.

Si light emitting pn-diodes (Si-LED)

LEDs emitting light from the pn-junction and made either by boron or by phosphorus implantation into Si attract special interest [5, 1, 85–87]. Efficient light emission at the Si bandgap energy was achieved by introduction of dislocation loops [5, 88] or surface texturing of ultrapure and passivated silicon [4].They allow efficient room temperature electroluminescence (EL) of the Si band-to-band line at 1.1 μm.

A high dose B^+ ion implantation into n-type Si, and the resulting pn-diodes were shown to exhibit increasing electroluminescence efficiency with increasing temperature, reaching values between 0.1 and 1% of external quantum efficiency [5, 88]. The efficient EL was assumed to result from carrier confinement near dislocation loops formed after implantation and annealing.

We use this latter approach as the starting point for our work. In our B^+ implanted structures the EL increases with temperature, resulting in a power efficiency of 0.1% at room temperature [1, 89]. A model has been proposed, which is based on the interplay between free excitons/carriers and excitons localized at nanoscale boron doping spikes, similar to δ-doped layers produced by MBE. Within this model it was possible to explain the EL dependence on current and temperature [89], as well as an electrical bistability occurring at low temperature [90].

Fig. 2.10 shows a typical emission spectrum of a bulk silicon pn-diode at room temperature after the thermal quenching of the bound exciton peaks, published by Sun in [89].

We do not want to speculate on the microscopic process, but simply to use the efficient EL Si pn-diode and to place it between two distributed Bragg mirrors forming a resonator, in order to fabricate a microcavity enhanced Si pn-diode (MCLED). The MCLED should enhance the outcoupling efficiency, spectral purity and directionality of emitted light from pn-junction.

In this work, it is not our intention to attempt a clarification of the detailed microscopic process responsible for the enhanced room-temperature EL, but we simply intend to employ the efficient Si pn-LED for a microcavity device. To this end we will place the LED between two distributed Bragg mirrors forming a resonator, in order to fabricate a microcavity enhanced Si pn-diode (MCLED). The MCLED should enhance the outcoupling efficiency, spectral purity and directionality of emitted light from pn-junction.

2.4 Microcavity enhanced light emitting pn-diode

The microcavity light emitting diode (MCLED) is a light emitting diode that has a light emitting region inside of an optical cavity. The optical cavity has a thickness of typically one-half to a few times the wavelength of the emitted light. The resonance wavelength of the cavity coincides or is in the resonance with the emission wavelength of the light emitting active region of the LED [91, 6].

The spontaneous emission of the LED is enhanced due to the resonant cavity effect, leading to the following light emission properties:

1. The light intensity emitted from the MCLED along the axis of the cavity (perpendicular to the surface) is higher compared with the conventional LEDs. The enhancement factor is typically a factor of 2 - 10.

2. The emission spectrum of the MCLED has a higher spectral purity. In conventional LEDs, the spectral emission linewidth is determined by the thermal energy kT. However, in MCLEDs, the emission linewidth is determined by the quality factor Q of the optical cavity. As a result, the spectral emission width of the MCLED is a factor of 2 - 5 narrower compared with conventional LEDs. For the same reason, the wavelength shift with temperature is determined by the temperature coefficient of the optical cavity and not by the energy band of the active material. This results in a significant higher temperature stability of the MCLED emission wavelength compared to the LED without the microcavity effect [91, 6].

3. The emission far field pattern of the MCLED is more directed, mostly along the optical axis. In conventional LED the emission pattern is lambertian.

Here a brief history of VCSEL and MCLED / RCLED: Motivation for VCSEL: for many applications it is useful to have any array of lasers which emit vertically from the substrate. This technology became viable through epitaxial growth (molecular beam epitaxy), where the active material and the Bragg reflectors are grown in the same run. Later on it was noticed (Schubert) that for many applications a coherently emitting VCSEL is not necessary, but a spontaneously LED with appropriate vertical mirror can be sufficient. Even in such a resonant (or micro-) cavity LED (RCLED or MCLED) one keeps the advantages of narrow emission spectrum and improved directionality.

In the following we will describe the properties of Bragg reflectors, Fabry-Perot resonators, and, as a combination of both, of a microcavity with two Bragg reflectors.

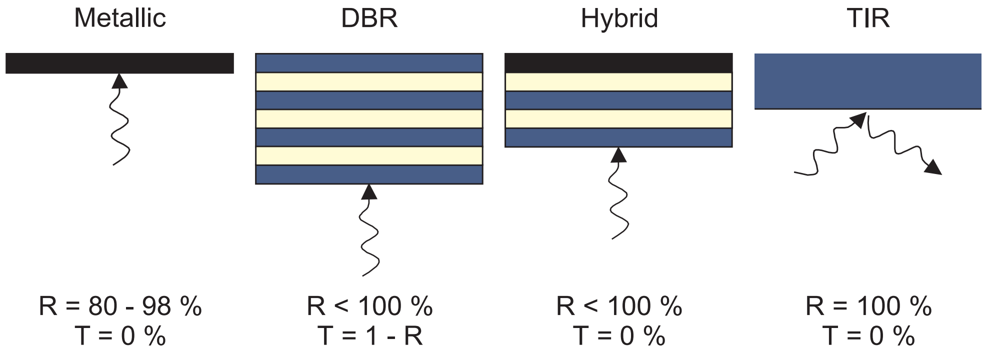

Figure 2.11: Different types of reflectors as metallic, distributed Bragg reflectors (DBR), hybrid metal-DBR reflectors, and total internal reflectors (TIR).

2.4.1 Bragg reflectors

Figure 2.11 shows the different types of reflectors as metallic, distributed Bragg reflectors (DBR), hybrid metal-DBR reflectors, and total internal reflectors (TIR). The transmittance of the metallic and hybrid reflectors is near zero (unless the thickness of the metal is very small), therefore they should not be used as light-exit reflectors [92]. By the total internal reflectors (TIR) the angle of incidence has to be shallow in order to achieve high reflectivity. TIR have been used in edge-emitting lasers [93] and in whispering gallery lasers [94]. A distributed Bragg reflector (also called Bragg mirror or quarter-wave mirror) is a structure which consists of an alternating sequence of layers of two different optical materials, with each optical layer thickness corresponding to one quarter of the wavelength for which the mirror is designed. The latter condition holds for normal incidence; if the mirror is designed for larger angles of incidence, accordingly thicker layers are needed. The operation principle can be understood as follows. Each interface between the two materials contributes a Fresnel reflection. For the design wavelength, the optical path length difference between reflections from subsequent interfaces is one half the wavelength; in addition, the reflection coefficients for the interfaces have alternating signs. Therefore, all reflected components from the interfaces interfere constructively, which results in a strong reflection. The achieved reflectivity is determined by the number of layer pairs and by the refractive index contrast between the layer materials. The reflection bandwidth is determined mainly by the index contrast. The comparison of reflectance spectra between metal mirror and a DBR is shown in Fig. 2.12. The metal Al reflector (optical constants from Palik [95]) exhibit a broad band with high reflectivity up to 98%, while the DBR based on 5.5 pairs of 200 nm SiO_2 / 80 nm a-Si, with optical constants also from Palik [95], display only a narrow band of high reflectivity denoted as the *stop band* with characteristic interference fringes [96–98].

Consider a distributed Bragg reflector consisting of m pairs of two dielectric, lossless materials with refractive indices $\overline{n}_1$ and $\overline{n}_2$. The thickness of the two layers is assumed to be a quarter wave, i.e. $L_1 = \lambda_{Bragg}/(4\overline{n}_1)$, and $L_2 = \lambda_{Bragg}/(4\overline{n}_2)$. The period of the DBR is $L_1 + L_2$. The reflectivity of the single interface is given by Fresnel's equation for normal incidence

$$r = \frac{\overline{n}_1 - \overline{n}_2}{\overline{n}_1 + \overline{n}_2} \tag{2.28}$$

The particular characteristic of a stack of $\lambda/4$ layers is to have a high reflectivity in a given spectral region. The reflectivity maximum is centered on the Bragg wavelength

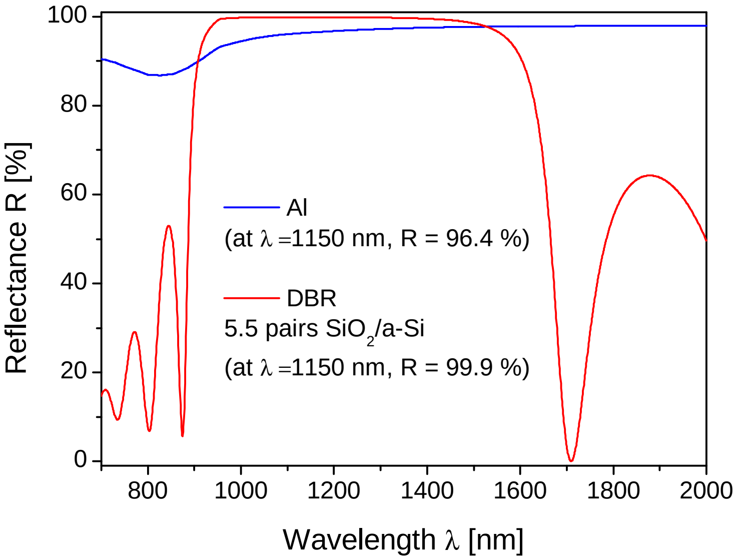

Figure 2.12: The comparison of reflectance spectra between Al mirror and a DBR consisting of 5.5-pairs of a-Si/SiO$_2$. Optical constants of Al, a-Si and SiO$_2$ are from Palik [95]).

λ_{Bragg} and it is given by [96]

$$R_{DBR} = |r_{DBR}|^2 = \left[\frac{1-(\overline{n}_1/\overline{n}_2)^{2m}}{1+(\overline{n}_1/\overline{n}_2)^{2m}}\right]^2 \tag{2.29}$$

where m is the number of pairs. The reason for this is that all the beams, which are reflected by the multiple interfaces, have the same phase when they reach the top interface. Thus they interfere constructively. For other wavelengths the interface is no longer constructive and the reflectivity consequently drops.

It is worth emphasizing the following considerations, which follow directly from Eq. 2.29:

1. keeping m fixed, the reflectivity increases as the ratio $\overline{n}_1/\overline{n}_2$ increases;
2. keeping $\overline{n}_1/\overline{n}_2$ fixed, R increases with increasing m.

Figure 2.13 a and b show examples of the reflectance spectra of various DBR obtained by varying m and n, respectively. There is no absorption considered in the simulation and $\overline{n}_{air}$= 1. The spectra are not symmetric around the region of maximal reflectivity, due to plotting on the wavelength scale, on a frequency scale it would be symmetric. Summarizing, we can conclude the following from these simulations [99]:

1. by increasing m, R increases;
2. by increasing m, the stop band becomes sharper;
3. by increasing $\overline{n}_1/\overline{n}_2$ the stop band enlarges and sharpens;
4. by increasing $\overline{n}_1/\overline{n}_2$ the overall reflectance value increase, that is, both in the stop band and in the side-lobes.

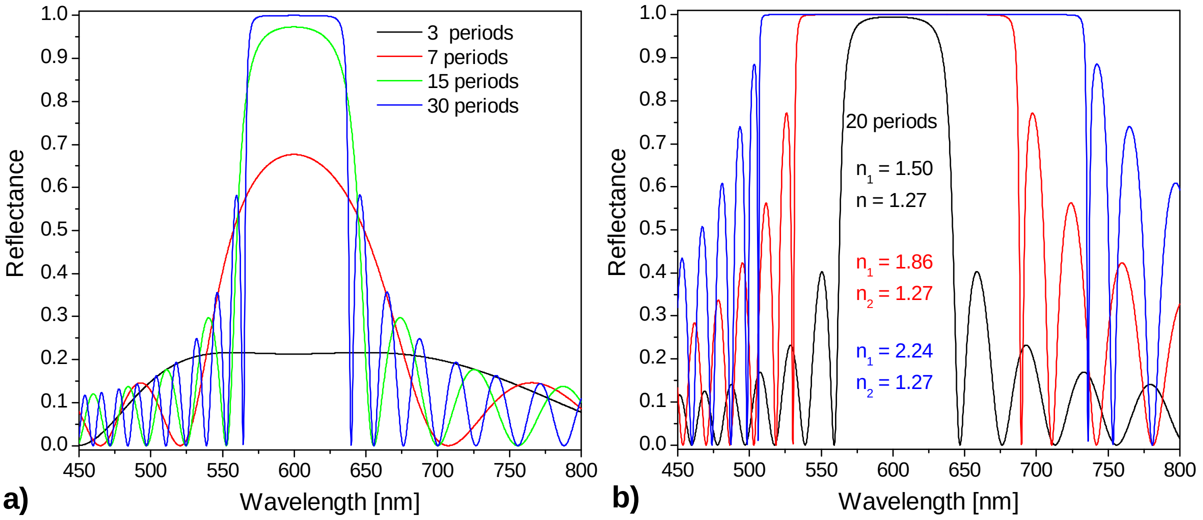

Figure 2.13: SCOUT simulation of reflectance spectra of DBR formed by a) different number of periods, the high ($\overline{n}_1$) and low ($\overline{n}_2$) refractive indexes have the values 1.5 and 1.27, respectively; b) a different ratio between the high and low refractive index.

The maximum reflectivity or stop band of DBR depends on the difference in refractive index of two constituent materials, $\Delta\overline{n}$. The spectral width of the stop band is given by [97]

$$\Delta\lambda_{\text{stop band}} = \frac{2\lambda_{Bragg}\Delta\overline{n}}{\pi\overline{n}_{eff}} \tag{2.30}$$

where $\overline{n}_{eff}$ is the effective refractive index of the mirror and is given by

$$\overline{n}_{eff} = 2\left(\frac{1}{\overline{n}_1} + \frac{1}{\overline{n}_2}\right)^{-1}. \tag{2.31}$$

In the case of two metal mirrors, the length of the cavity is the physical distance between them. For DBRs, the optical wave penetrates into the reflector by one or several quarter-wave pairs (Fig. 2.14). Only a finite number of the quarter-wave pairs are effective in reflecting the optical wave. The effective number of pairs seen by the wave electric field is given by [96]

$$m_{eff} = \frac{1}{2}\frac{\overline{n}_1 + \overline{n}_2}{\overline{n}_1 - \overline{n}_2} tanh\left(2m\frac{\overline{n}_1 - \overline{n}_2}{\overline{n}_1 + \overline{n}_2}\right). \tag{2.32}$$

For very thick DBRs ($m \to \infty$) the *tanh* function approaches unity and one obtains

$$m_{eff} = \frac{1}{2}\frac{\overline{n}_1 + \overline{n}_2}{\overline{n}_1 - \overline{n}_2}. \tag{2.33}$$

At the Bragg wavelength ($\lambda = \lambda_{Bragg}$), the phase change of the reflected wave is zero. In the vicinity of the Bragg wavelength ($\lambda \approx \lambda_{Bragg}$), the phase of the reflected wave changes *linearly* with the wavelength. It is therefore possible to approximate a DBR with a metal-like mirror located a distance L_{pen} behind the first dielectric interface. The reflection of the DBR can thus be expressed as

$$r_{DBR} \approx |r_{DBR}|e^{-2i(\beta-\beta_{Bragg})L_{pen}} \tag{2.34}$$

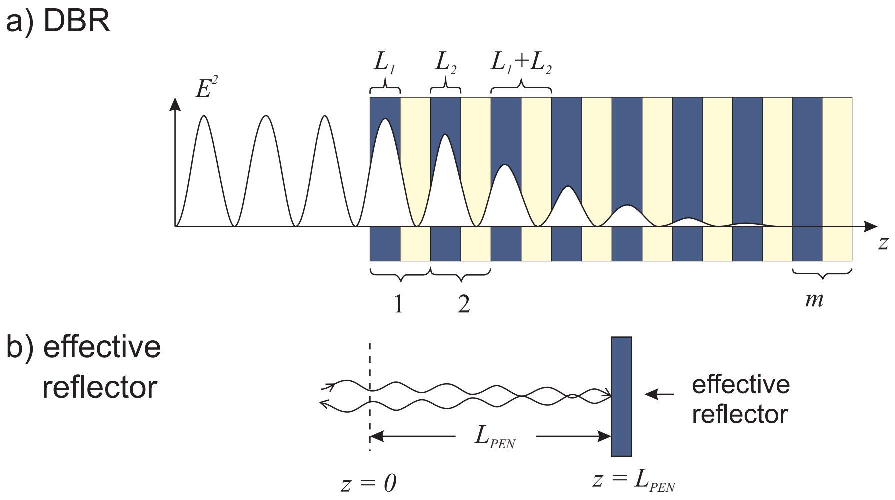

Figure 2.14: Illustration of the DBR penetration depth. (a) DBR consisting of two materials with thickness L_1 and L_2. (b) Ideal (metallic) reflector displaced from the DBR surface by the penetration depth.

where $\beta = 2\pi/\lambda$ is the average phase constant of the wave. The phase change at *z=0* of the wave reflected by the metal mirror is given by

$$r_{metal}|_{z=0} = |r_{metal}|e^{2i(2\pi/\lambda)L_{pen}}. \tag{2.35}$$

Equating the phase changes given by Eqs. 2.34 and 2.35 and using the phase changes of a DBR [96], the penetration depth is given by

$$L_{pen} = \frac{L_1 + L_2}{4r} tanh(2mr). \tag{2.36}$$

For a large number of pairs ($m \to \infty$) [6], the penetration depth is given by

$$L_{pen} = \frac{L_1 + L_2}{4r} = \frac{(L_1 + L_2)}{4}\frac{\overline{n}_1 + \overline{n}_2}{\overline{n}_1 - \overline{n}_2} \tag{2.37}$$

Comparison of Eqs. 2.37 and 2.33 yields that

$$L_{pen} = \frac{1}{2} m_{eff}(L_1 + L_2). \tag{2.38}$$

The factor of (1/2) in Eq. 2.38 is due to the fact that m_{eff} applies to the effective number of periods seen by the *electric field*, whereas L_{pen} applies to the optical power, which is equal to the square of the electric field and hence it penetrates half as far to the mirror [6]. The effective length of a cavity consisting of two DBRs is thus given by the sum of the thickness of the center region plus the two penetration depths into the DBRs. The effective length of a cavity with DBRs is thus longer than the effective length of a cavity with metal mirrors.

2.4.2 Fabry-Perot resonators

The simplest form of an optical cavity consists of two coplanar mirrors separated by a distance L_{cav} . In 1899 Fabry and Perot have demonstrated optical cavities with

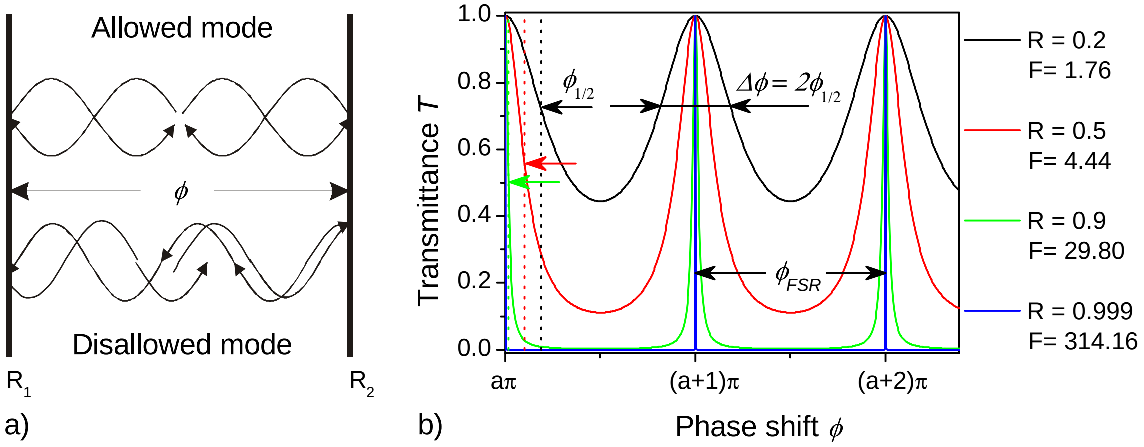

Figure 2.15: (a) Schematic illustration of allowed and disallowed optical modes in a Fabry-Perot cavity consisting of two coplanar reflectors. (b) Optical mode density of a symmetric resonator ($R_1 = R_2 = R$) for different values of R.

coplanar reflectors with a large separation between the two reflectors $L_{cav} \gg \lambda$. However, if the distance between the two reflectors is of the order of the wavelength of light, new physical phenomena occur, including the enhancement of the optical emission from an active material inside the cavity. Very small cavities, with typical dimensions of $L_{cav} \approx \lambda$, will be denoted as *microcavities*.

Coplanar microcavities are the simplest form of optical microcavities and their properties are summarized below. Fabry-Perot cavities with two reflectors of reflectivity R_1 and R_2 are shown in Figs. 2.15. Plane waves propagating inside the cavity can interfere constructively and destructively resulting in stable (allowed) optical modes and attenuated (disallowed) optical modes, respectively. For lossless (non-absorbing) reflectors, the transmittance through the two reflectors is given by $T_1 = 1 - R_1$ and $T_2 = 1 - R_2$. Taking into account multiple reflection inside the cavity, the transmittance through s Fabry-Perot cavity can be expressed in terms of a geometric series. The transmitted light intensity is given by

$$T(\phi) = \frac{T_1 T_2}{1 + R_1 R_2 - 2\sqrt{R_1 R_2}\cos 2\phi} \tag{2.39}$$

where ϕ is the phase change of the optical wave for a single pass between two reflectors. The maxima of the transmittance occur if the condition of constructive interference is fulfilled, i.e. if the denominator in the fraction is minimal. This is valid for $2\phi = 0, 2\pi, \ldots$. Insertion of these values into Eq. 2.39 yields the transmittance maxima as

$$T_{max} = \frac{T_1 T_2}{(1 - \sqrt{R_1 R_2})^2}. \tag{2.40}$$

For asymmetric cavities ($R_1 \neq R_2$), it is $T_{max} < 1$. For symmetric cavities ($R_1 = R_2$), the transmittance maxima $T_{max} = 1$.

Near $2\phi = 0, 2\pi, \ldots$, the cosine term in Eq. 2.39 can be expanded into a power series ($cos 2\phi \approx 1 - 2\phi^2$). One obtains

$$T = \frac{T_1 T_2}{(1 \pm \sqrt{R_1 R_2})^2 + \sqrt{R_1 R_2} 4\phi^2}. \tag{2.41}$$

Equation 2.41 indicates that near the maxima, the transmittance can be approximated by a lorentzian function. The transmittance T in Eq. 2.41 has a maximum at $\phi = 0$. The transmittance decreased to half of the maximum value at

$$\phi_{1/2} = \frac{1}{2} arccos \frac{2R}{1+R^2} \approx \frac{1-\sqrt{R_1R_2}}{2\sqrt[4]{R_1R_2}}. \tag{2.42}$$

For high values of R_1 and R_2, i.e. $R_1 \approx 1$ and $R_2 \approx 1$, it is

$$\phi_{1/2} = \frac{1}{2}(1-\sqrt{R_1R_2}). \tag{2.43}$$

The cavity finesse, F, is defined as the ratio of the transmittance peak separation to the transmittance full-width at half-maximum, i.e.

$$F = \frac{\text{Peak separation}}{\text{Peak width}} = \frac{\phi_{FSR}}{\Delta\phi} = \frac{\pi}{2\phi_{1/2}} = \frac{\pi\sqrt[4]{R_1R_2}}{1-\sqrt{R_1R_2}} \approx \frac{\pi}{1-\sqrt{R_1R_2}}. \tag{2.44}$$

Inspection of Eq. 2.44 shows that the finesse becomes very large for high values of R_1 and R_2 (see Fig. 2.15 b).

The wavelength and frequency of light are practically more accessible than the phase. Eq. 2.39 - 2.44 can be converted to wavelength and frequency using

$$\phi = 2\pi\frac{\overline{n}L_{cav}}{\lambda} = 2\pi\frac{\overline{n}L_{cav}\nu}{c} \tag{2.45}$$

where L_{cav} is the length of the cavity, λ is the wavelength of light in vacuum, ν is the frequency of the light, and $\overline{n}$ is the reflection index inside the cavity. Practically this means that:

$$\text{for} \quad \phi = 0 \quad \lambda = \infty \quad \text{and} \quad \nu = 0 \tag{2.46}$$

$$\text{for} \quad \phi = \pi \quad \nu = \nu_0 = \frac{c}{2\overline{n}L_{cav}} \tag{2.47}$$

$$\text{for} \quad \phi = 2\pi \quad \nu = 2\nu_0 = 2\cdot\frac{c}{2\overline{n}L_{cav}} \tag{2.48}$$

$$\text{for} \quad \phi = 3\pi \quad \nu = 3\nu_0 = 3\cdot\frac{c}{2\overline{n}L_{cav}} \tag{2.49}$$

The maximum of transmittance T_{max} occurs at frequencies ν_0, $2\nu_0$, $3\nu_0$, ... (see Fig. 2.15). The frequency ν_0 is also called *resonant frequency*

In the frequency domain, the transmittance peak separation is called *free spectral* range ν_{FSR}. The finesse of the cavity in the frequency domain is given by $F = \nu_{FSR}/\Delta\nu$.

Frequently the cavity quality factor Q rather than the finesse is used. The Q is defined as the ratio of the transmittance peak frequency to the peak width. Using this definition and Eq. 2.44, one obtains

$$Q = \frac{\text{Peak frequency}}{\text{Peak width}} = \frac{2\overline{n}L_{cav}}{\lambda} \times \frac{\pi\sqrt[4]{R_1R_2}}{1-\sqrt{R_1R_2}} \approx \frac{2\overline{n}L_{cav}}{\lambda} \times \frac{\pi}{1-\sqrt{R_1R_2}} = \frac{2\overline{n}L_{cav}}{\lambda} \times F \tag{2.50}$$

where the peak width is measured in units of frequency.

Practical Fabry-Perot devices are governed by various loss elements that limit the expected performance of the device. The typical sources of losses are [100]:

1. Losses attributed to the absorption and scattering of the media that surround the mirrors.

2. Losses arising from imperfect reflections at the mirror of the Fabry-Perot filter. Non-ideal mirrors cause the light to be partially transmitted through the mirrors and the cavity, compromising performance.

2.4.3 Optical mode density and emission enhancement in coplanar Fabry-Perot resonator

Let's consider a coplanar (one-dimensional) Fabry-Perot resonator. According to Yariv [101], the spontaneous radiative transition rate in an optically active, homogeneous medium is given by:

$$W_{spont} = \tau_{spont}^{-1} = \int_0^{\infty} W_{spont}^{l}\, \rho(\nu_l) d\nu_l, \tag{2.51}$$

where W_{spont}^{l} is the spontaneous transition rate into the optical mode l and $\rho(\nu_l)$ is the optical mode density per unit length and frequency, which in a one-dimensional (1D) homogeneous medium is given by:

$$\rho^{1D}(\nu) = \frac{2\overline{n}}{c}. \tag{2.52}$$

In this equation $\overline{n}$ is refractive index of the medium.

The optical mode density of a 1D cavity for emission along the cavity axis is given by:

$$\rho(\nu) = \frac{(R_1R_2)^{3/4}}{T_1T_2}\frac{4\overline{n}}{c}(1-\sqrt{R_1R_2})T(\nu), \tag{2.53}$$

where $T(\nu)$ is the transmission through a Fabry-Perot cavity. The maxima of the mode density is given by [6]:

$$\rho_{max} = \frac{(R_1R_2)^{3/4}}{1-\sqrt{R_1R_2}}\frac{4\overline{n}}{c} \approx \frac{4}{\pi}\frac{\overline{n}F}{c}. \tag{2.54}$$

The minima of the mode density can be written as [6]:

$$\rho_{min} = \frac{(R_1R_2)^{3/4}(1-\sqrt{R_1R_2})}{(1+\sqrt{R_1R_2})^2}\frac{4\overline{n}}{c} \approx \pi\frac{\overline{n}}{cF}. \tag{2.55}$$

The physics of optical mode densities are in detail described in [6, 101]

In Fig. 2.16 (a) the comparison of the optical mode density of a coplanar (1D) Fabry-Perot microcavity (solid line), $\rho(\nu)$, and of the homogeneous 1D free space (dashed line), $\rho^{1D}(\nu)$, is shown. The total number of modes is conserved, i.e the areas below the 1D mode density and the 1D cavity mode are the same. Fig. 2.16 shows (b) the theoretical shape of emission spectrum of an LED, which has been discussed in more detail in Sec. 2.2.2.

Emission enhancement

The emission rate at a given wavelength is directly proportional to the optical mode density (see Eq. 2.51). The *spectral emission enhancement* G_e at the resonant frequency ν_0 is defined as a ratio of the one dimensional optical mode density of the cavity ρ_{max}

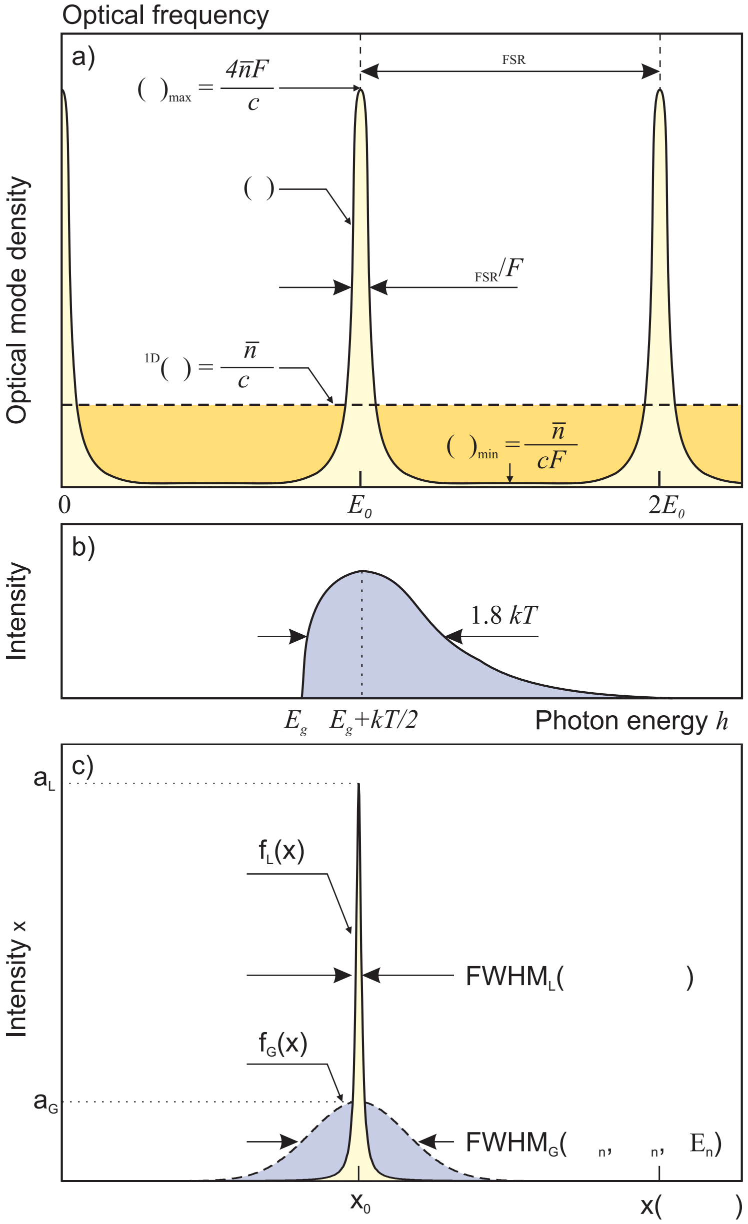

Figure 2.16: (a) Optical mode density of coplanar (1D) Fabry-Perot microcavity (solid line) and of homogeneous 1D space (dashed line). (b) Theoretical emission spectrum of an LED. (c) Natural emission spectrum with a Gaussian shape (dashed line) and the enhanced (resonant) spectrum having a Lorentzian shape (solid line) used for the analytical calculation of the integrated emission enhancement G_{int}.

and the free space ρ^{1D} (Fig. 2.16 a). The equation representing the average emission rate enhancement out of both reflectors of the cavity is written in following form:

$$G_e = \frac{\rho_{max}}{\rho^{1D}} \approx \frac{2}{\pi}F \approx (\frac{2}{\pi})\frac{\pi\sqrt[4]{R_1R_2}}{1-\sqrt{R_1R_2}}. \tag{2.56}$$

To find the emission rate enhancement only out of the semitransparent mirror R_1, Eq. 2.56 must be multiplied by the fraction of the light exiting the semitransparent mirror $(1-R_1)$ divided by the average mirror loss for one round trip in the cavity $\frac{1}{2}[(1-R_1)+(1-R_2)]$. For large R_1 and R_2 and using the approximation $1-\sqrt{R_1R_2} \approx \frac{1}{2}(1-R_1R_2) \approx \frac{1}{2}(2-R_1-R_2)$ the emission rate enhancement through a single reflector with reflectivity R_1 can be written as

$$G_e^{R1} \approx \frac{2(1-R_1)}{2-R_1-R_2}\frac{2F}{\pi} \approx \frac{1-R_1}{1-\sqrt{R_1R_2}}\frac{2F}{\pi} \approx \frac{2}{\pi}\frac{\pi\sqrt[4]{R_1R_2}(1-R_1)}{(1-\sqrt{R_1R_2})^2}. \tag{2.57}$$

Let us take into account a distribution of the optically active material relative to the nodes and antinodes of the optical wave (the optical standing wave effect). The antinode enhancement factor ξ has a value of:

1. $\xi = 2$, if the active region is located exactly at the antinode of the standing wave inside the cavity.
2. $\xi = 1$, if the active region is too broad and smeared out over many periods of the standing optical wave.
3. $\xi = 0$, if the active region is located at a node.

The equation for emission rate enhancement G_e, which takes into account changes in the spontaneous emission lifetime without cavity τ and with cavity τ_{cav} is written as [39]

$$G_e = \frac{\xi}{2}\frac{2}{\pi}\frac{\pi(R_1R_2)^{1/4}(1-R_1)}{(1-\sqrt{R_1R_2})^2}\frac{\tau_{cav}}{\tau}. \tag{2.58}$$

The factor $\frac{\tau_{cav}}{\tau}$ ensures that the enhancement decreases if the cavity lifetime is reduced as a result of the cavity. For planar microcavities, the ratio $\frac{\tau_{cav}}{\tau} \geq 0.9$ [102]. Thus, the emission lifetime change is negligible for a planar microcavity.

The *integrated emission enhancement* over the wavelength can be calculated analytically assuming that the natural emission spectrum has a Gaussian shape (G) and the enhanced (resonant) spectrum has a Lorentzian shape (L) (Fig. 2.16 c):

$$f_G(x) = \frac{1}{\sigma\sqrt{2\pi}} \cdot e^{-\frac{(x-x_0)^2}{2\sigma^2}} = a_G \cdot e^{-\frac{(x-x_0)^2}{2\sigma^2}}, \tag{2.59}$$

$$f_L(x) = \frac{2}{\pi\Gamma} \cdot \frac{1}{(x-x_0)^2+\frac{1}{4}} = a_L \cdot \frac{1}{(x-x_0)^2+\frac{1}{4}}, \tag{2.60}$$

where σ is the standard deviation of the gaussian function, Γ is the scale parameter specifying the width of the lorentzian spectrum, a_G and a_L are the amplitudes of the gaussian and the lorentzian function, respectively. The full widths at half-maxima (FWHM) of these functions are

$$FWHM_G = \Delta\lambda_n = 2\sigma\sqrt{2ln2} \tag{2.61}$$

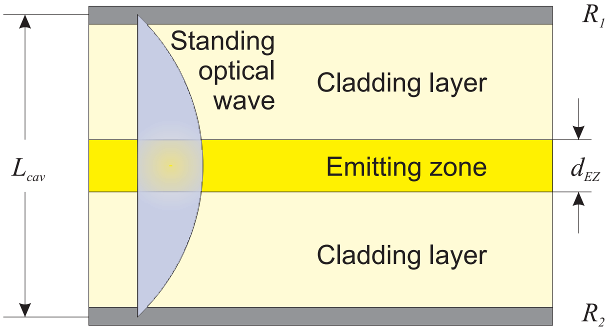

Figure 2.17: Scheme of a resonant cavity consisting of two metal mirrors with reflectivity R_1 and R_2. The active region has a thickness L_{active} and an absorption coefficient α. The cavity length L_{cav} is equal to $\lambda/2$.

$$FWHM_L = \Delta\lambda = \Gamma \tag{2.62}$$

The integrals of both functions over x correspond to the areas below these functions and are written in the following form

$$A_G = a_G \sigma \sqrt{2\pi} \tag{2.63}$$

$$A_L = a_L \Gamma \frac{\pi}{2} \tag{2.64}$$

Using the equations 2.59 - 2.64 can the integrated emission enhancement written as [103]:

$$G_{int} = \frac{A_L}{A_G} = \frac{a_L}{a_G} \frac{\frac{\pi}{2}\Delta\lambda}{\sigma\sqrt{2\pi}} = G_e \sqrt{\pi ln2} \frac{\Delta\lambda}{\Delta\lambda_n}, \tag{2.65}$$

where $\Delta\lambda$ and $\Delta\lambda_n$ are the FWHMs of the cavity resonance peak and of the natural emission linewidths, respectively. It is obvious that $\Delta\lambda < \Delta\lambda_n$ for a resonant cavity. One part of the natural emission spectrum is strongly enhanced, whereas the rest of spectrum is suppressed. Eq. 2.65 shows that narrow resonance spectral widths, i.e. high finesse values or long cavities, reduce the integrated enhancement (see an example in the Fig. 2.16 c, where $G_e = 5$, $\Delta\lambda/\Delta\lambda_n = 0.054$, $G_{int} = 0.4$).

2.4.4 Design and optical properties of a Si microcavity LED

In this section a 1λ-MCLED consisting of one crystalline Si active (light emitting) layer and two SiO$_2$ /a-Si DBRs is designed.

The basic structure of the MCLED with two metal mirrors with unequal reflectivities R_1 and R_2 is shown in Fig. 2.17. Let's consider that $R_1 < R_2$. The light exits the cavity predominantly through mirror with reflectivity R_1. It is also called *light-exit mirror.* The active region is located between the mirrors, preferably at the antinode of the standing optical wave of the cavity. The wave amplitude at the mirrors is zero.

Three criteria for MCLED design are summarized by Schubert [104, 105, 6]:

1. The reflectivity of the exit reflector, R_1, should be lower than the reflectivity of the back reflector R_2.

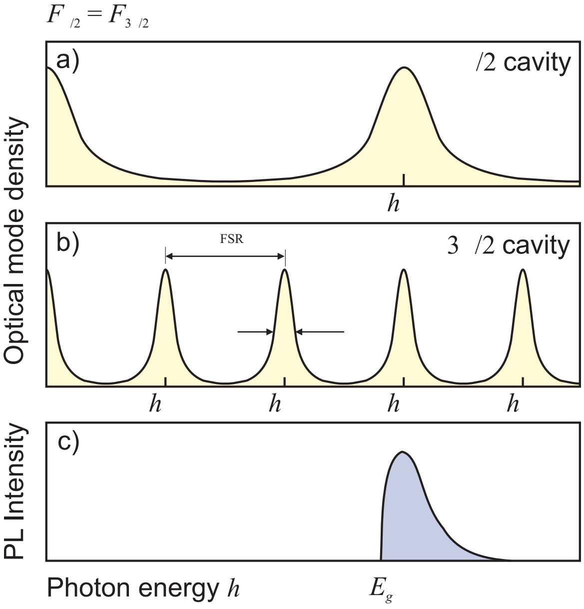

Figure 2.18: Optical mode density for (a) a short and (b) a log cavity with the same finesse F. (c) Theoretical emission spectrum of an LED active region (also in Fig. 2.4)

2. The cavity length L_{cav} should be as short as possible, which maximizes the integrated intensity. The importance of a short cavity is shown in Fig. 2.18. The optical mode densities of short ($\lambda/2$) and long ($3\lambda/2$) cavities are shown in Fig. 2.18a and 2.18b, respectively. Both cavities have the same mirror reflectivities and finesse. The natural emission spectrum of the active region is shown in Fig. 2.18c. The best overlap between the resonant optical mode and the emission spectrum from the active region is obtained for the shortest cavity. The cavity mode has to be in resonance with the emission from the active medium.

3. The self-absorption in the active region should be minimized, i.e. the reabsorption of photons emitted from the active region into the cavity mode should be smaller than the escape probability of photons through one of the reflectors. Re-absorption processes occurring in high-finesse cavities reduce the cavity mode emission out of the cavity.

The structure of the Si based MCLED is schematically drawn in Fig. 2.19. The system is defined for a resonance wavelength of $\lambda_{res} = 1150$ nm. The optical constants of the crystalline silicon (Si), amorphous silicon (a-Si) and silicon dioxide (SiO_2) used in reflectance and electroluminescence calculations are taken from Palik [95], having an index of absorption $\kappa = 0$. The active layer is crystalline silicon (Si) with a refractive index of $n_{Si} = 3.5419$ at 1150 nm. In order to simulate the 1λ cavity, the theoretical thickness of the Si active layer is $\lambda_{res}/n_{Si} = 324.68$ nm. The refractive indices of SiO_2 and a-Si, forming the top and the bottom multilayered mirror systems, are $n_{SiO2} = 1.4486$ and $n_{a-Si} = 3.564$ at the wavelength 1150 nm, respectively. In order to keep the conditions for distributed Bragg reflectors, the thicknesses of layers forming a DBR have to be a quarter of the resonance wavelength divided by their refractive indices. Thus the thicknesses of SiO_2 and a-Si layers are 198.47 nm and 80.67 nm, respectively.

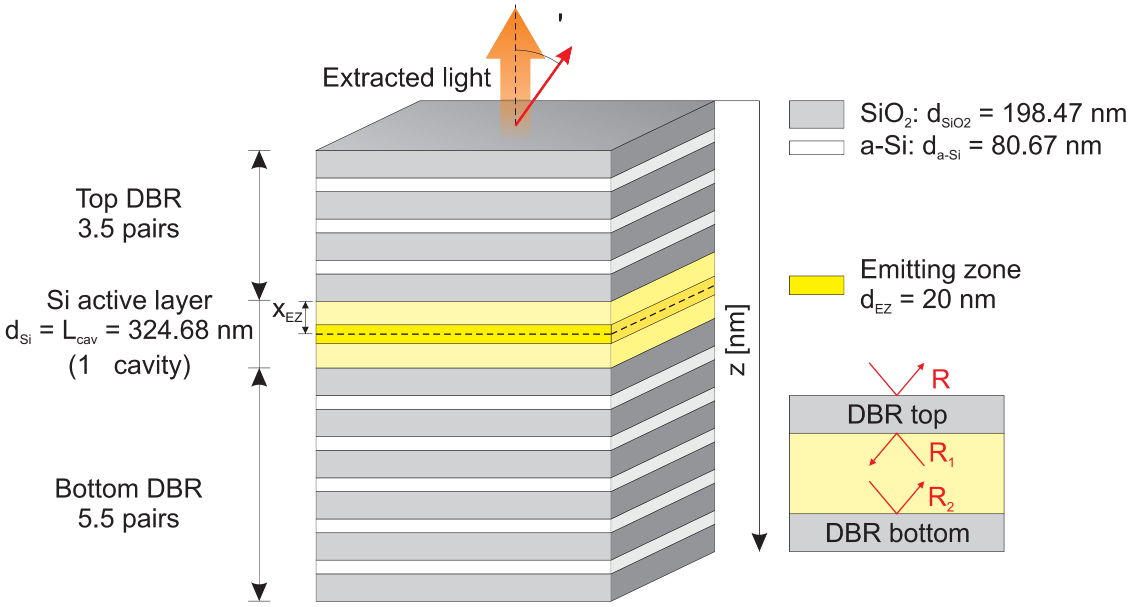

Figure 2.19: Schematic structure of Fabry-Perot microcavity system resonating at the wavelength $\lambda = 1150$ nm, where the material of the active layer is crystalline silicon (Si) having the thickness of $L_{cav} = 324.68$ nm (yellow) for a 1λ cavity. The materials of the top and bottom distributed Bragg reflectors are amorphous silicon (a-Si) with thickness $\lambda/4n_{a-Si} = 80.67$ nm (white) and SiO_2 of thickness $\lambda/4n_{SiO2} = 198.47$ nm (gray). The bottom and the top semitransparent DBRs contain 5.5 and 3.5 pairs SiO_2 /a-Si, respectively.

Reflectance

The calculations of the reflectance and electroluminescence of the MCLED shown in Fig. 2.19 were done using the program UniMCO (see Sec.3.2.4).

UniMCO calculates the reflection, transmission, absorption and the phase shift at three different interfaces R_1, R_2, and R. The calculated quantities at R_1 are for the top mirror, those at R_2 are for the bottom mirror, and those at R are for the whole device or microcavity (see Fig.2.19).

The angle in UniMCO is defined in relation to the surface normal. The maximum angle range is $-90° \leq \theta \leq +90°$. The UniMCO program calculates optical properties using the theory detailed described in Sec.2.4.2.

Figure 2.20a shows the plots of the reflectance (R) calculation of the MCLED from Fig. 2.19 as a function of the wavelength and over the angle range ±90°. The reflectivity has a sharp dip at 1150 nm with the full width at half minimum of 1.18 nm. The reflectance of the cavity does not approach zero at the resonant wavelength due to the unequalness of the reflectivities of the two reflectors. The reflectance minimum shifts to smaller wavelengths with increasing angle of about 1045 nm at 88°. Fig. 2.20b and 2.20c show the reflectance spectra in dependence on wavelength at an angle of 0° and as a function of angle at the resonant wavelength 1150 nm, respectively.

The reason for the sharp reflectivity drop is that at the resonant wavelength the primary reflected beam is canceled out by destructive interference of the multiple reflected beams inside of the cavity (Fig.2.21) [106]. This is true, if the phase shift between the primary reflected beam R_0^* and the multiple reflected beams R_1^*, R_2^*, R_3^*,... (see Fig. 2.21b) is an odd integer multiple of π. The incoming beam, the primary reflected beam R_0^* and the multiple reflected beams R_1^*, $R_2^* \cdots R_m^*$ can be described as follows:

$$\begin{aligned} I_0 : cos(\omega t - kx),\ R_0^* : cos(\omega t - kx + \pi), \quad & R_1^* : cos[\omega t - k(x + 2\bar{n}L_{cav})] \\ & R_2^* : cos[\omega t - k(x + 4\bar{n}L_{cav})] \\ & \vdots \\ & R_m^* : cos[\omega t - k(x + 2m\bar{n}L_{cav})] \end{aligned} \tag{2.66}$$

respectively, where $\bar{n}$ is the refractive index of the cavity medium and L_{cav} is the cavity length. The π in the primary reflected beam equation is due to the reflection from a material that has a greater refractive index (optically more dense) than the medium, where the incident beam comes from, $\bar{n} > \bar{n}_0$. Then the condition for destructive interference is given by:

$$[\omega t - k(x + 2\bar{n}L_{cav})] - (\omega t - kx + \pi) = (2m - 1)\pi, \tag{2.67}$$

where m is an integer. This yields to resonance condition for the cavity length

$$L_{cav} = m \cdot \frac{\lambda}{2\bar{n}}, \tag{2.68}$$

taking into the account, that the wave vector $k = 2\pi/\lambda$.

For maximum attenuation of the reflectance all intensity of the primary reflected beam has to be equal to the sum of the intensities of the multiple reflected beams.

$$r = t^2r + t^2r^3 + t^2r^5 + \ldots = \sum_{n=1}^{m} t^2r^{2n-1}, \tag{2.69}$$

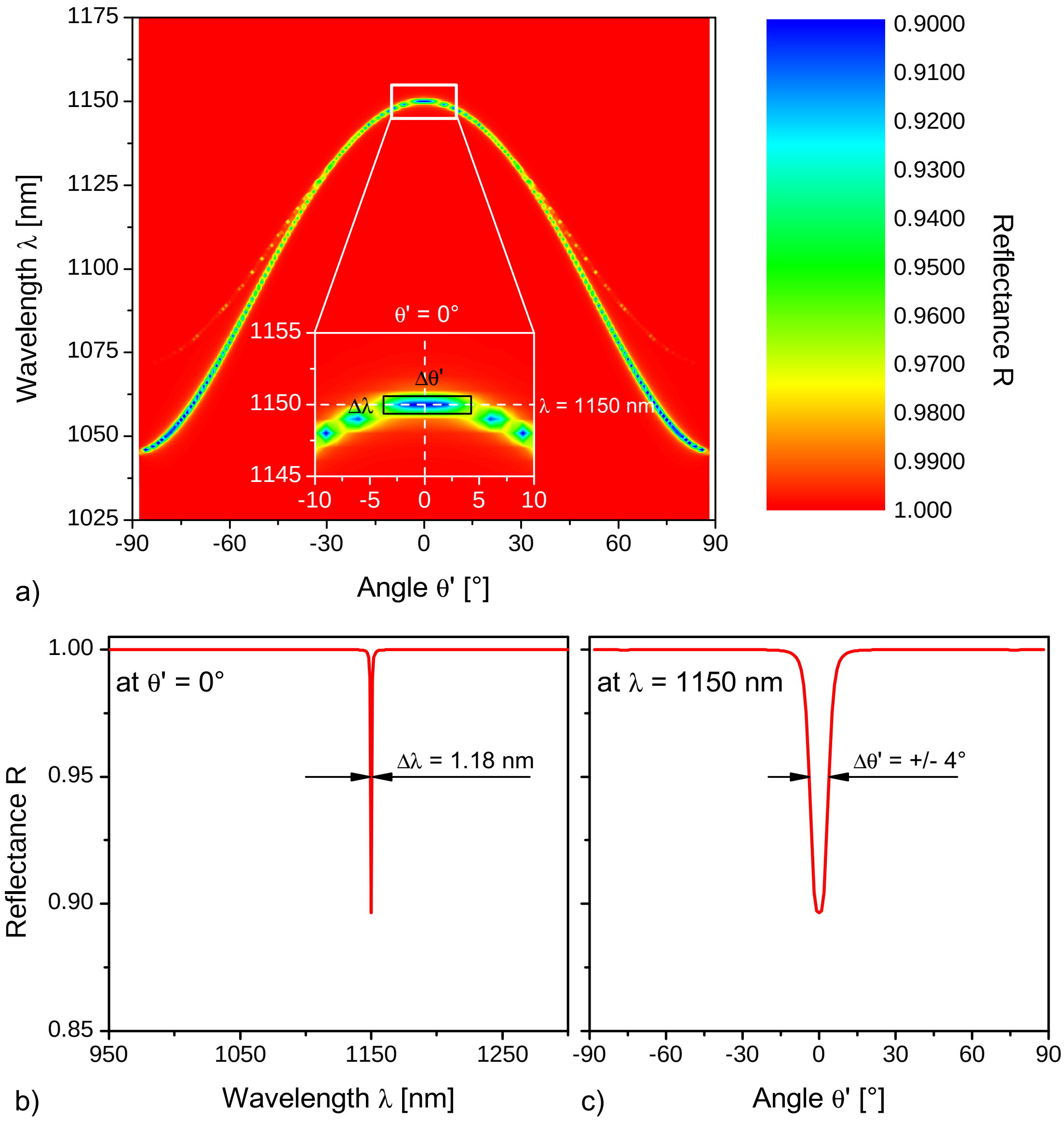

Figure 2.20: a) Calculated reflectance intensity of a Fabry-Perot microcavity consisting of two SiO_2 /a-Si reflectors and a Si active region in dependence on the wavelength and the angle θ' relative to the surface normal. b) Reflectance as a function of the wavelength λ at an angle of θ' $= 0°$. At the resonance wavelength λ=1150 nm a sharp dip of the reflectance is visible. c) Reflectance as a function of the angle θ' for the resonant wavelength λ=1150 nm.

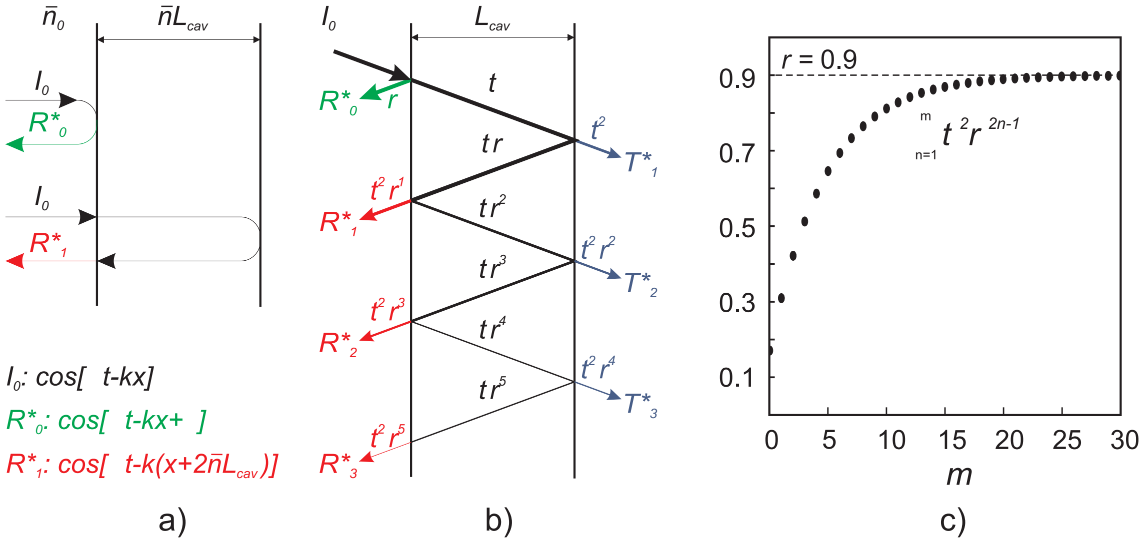

Figure 2.21: a) Definition of the incoming beam I_0, the primary reflected beam R_0^* and the multiple reflected beam R_1^*. b) Reflection and transmission of a light wave with an electric field amplitude I_0 through a Fabry-Perot resonator. c) Numerical calculation of the sum of multiple reflected beams for $r = 0.9$ [106].

where r and t are the factors of reflection and transmission for the electric field amplitude, respectively. $T = t^2$ and $R = r^2$ are the optical transmittance and the reflectance, respectively. This is true for the stationary case (infinite multiple reflection) and a nonabsorbing cavity medium ($T + R = 1$).

Fig. 2.21c shows the numerical calculation of $\sum_{n=1}^{m} t^2 r^{2n-1}$ for $r = 0.9$. For the stationary case, when $m \to \infty$, the $\sum_{n=1}^{m} t^2 r^{2n-1}$ approaches asymptotically the value $r = 0.9$, what means the total annihilation of the reflected amplitude.

Electric field distribution

The computation of the electric field distribution of the layer stack from Fig. 2.19 is shown in the Fig. 2.22. The angle of incidence of the incoming beam was set to zero in the simulation. The spatial range z for the electric field is over the whole cross section of the stack starting with zero at the top DBR up to 2950 nm at the bottom of the stack. The calculation is performed for the resonant wavelength of 1150 nm. The gray and the white fields in Fig. 2.22 correspond to 198.47 nm SiO_2 and 80.67 nm a-Si of the top and the bottom DBR, respectively. The broad yellow field in the middle represents the 1λ cavity, i.e. the active layer with the thickness $\Delta z = d = 324.68$ nm. In order to get an efficient Si-MCLED, the pn-junction has to be placed into the antinode of the electric field. Two antinodes (maxima) of the electric field amplitude of 1λ cavity are situated at the boundaries of the active layer and one antinode is exactly in the middle of the active layer. Since the pn-junction can be formed only inside of this active layer and not at its surface, the pn-junction has to be placed exactly in the middle of the active silicon layer (green solid line). This is also a reason why a $\lambda/2$ cavity design, having only 2 antinodes placed at the boundaries, does not appear so useful.

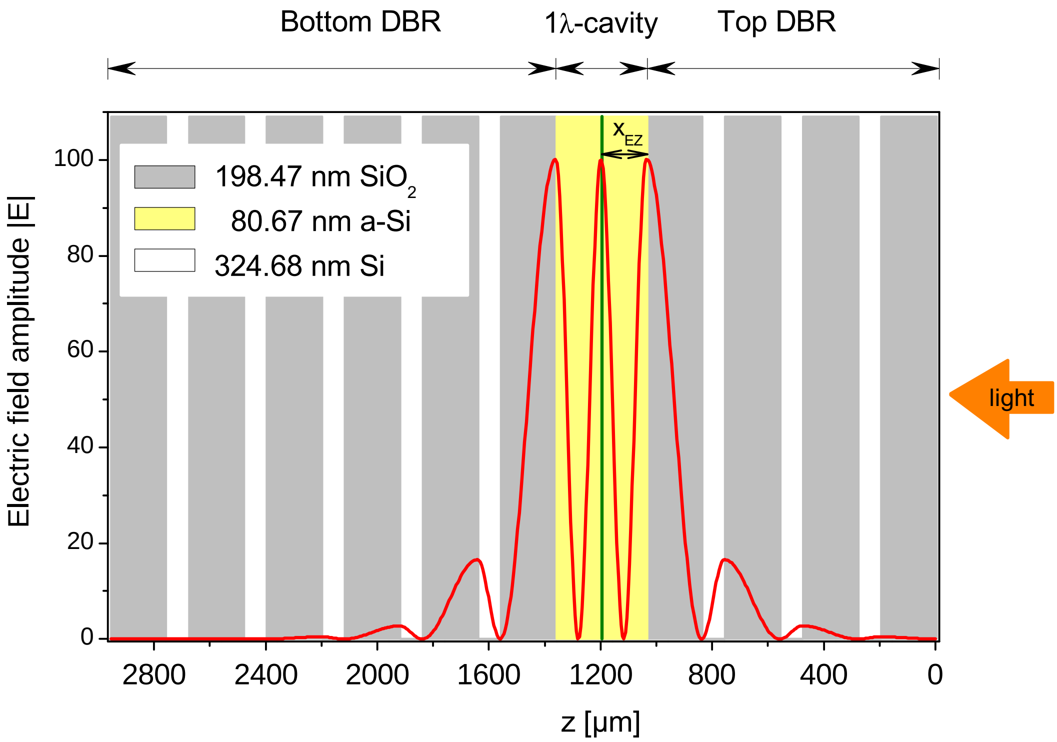

Figure 2.22: Calculated electric field intensity of the resonant mode in the investigated 1λ cavity MCLED. The calculation is performed for the 1150 nm wavelength and the structure shown in Fig. 2.19. Light is incident from the right side. Positions of high refractive index a-Si layers (white), low refractive index SiO_2 (gray) and the active Si layer (yellow) are shown in the background. In order to get a high efficiency MCLED the pn-junction must be placed exactly in the maximum of electric field amplitude, which is in the center of the active layer (green solid line).

Electroluminescence

Now, when the reflectivity and electric field amplitude data are available, the light output and efficiency can be calculated.

The method used in the code UniMCO for the calculation of the emitting power from a given medium is based on the transfer matrix formalism including additional source terms for the electric field (i.e., the dipole emission terms) [107]. The electric field emitted by electric dipoles can be expressed in terms of a superposition of s-(TE) and p-(TM) polarized waves, while the dipole source can be decomposed into three orthogonal components (ds, dp, dv), where ds and dp are in-plane dipole components, and dv is the out-of plane component. It can be shown [107] that the power per unit solid angle and surface emitted by such dipoles in an unbounded medium of refractive index n_{emit} are of the form:

$$P_0^s \propto \frac{3}{8\pi}, \quad P_0^p \propto= \frac{3}{8\pi} cos^2\theta, \quad P_0^v \propto= \frac{3}{8\pi} sin^2\theta \tag{2.70}$$

The above expressions describe the plane wave emission if $0 \leq cos^2\theta \leq 1$ and the evanescent wave emission if $cos^2\theta < 0$.

The situation inside of the microcavity is more complicated. For the dipoles inside a microcavity device, the power per unit solid angle and surface $P_{front}^{s,p,v}$ radiated outwards the microcavity by the s-, p-, and v-dipoles can be calculated from the following formula:

$$P_{front}^{s,p,v} = \left| 1 + r_2^{s,p,v} e^{2i\phi'} \right|^2 \frac{1 - |r_1^{s,p,v}|^2}{|1 - r_2^{s,p,v} r_1^{s,p,v} e^{2i\phi}|^2} P_0^{s,p,v}. \tag{2.71}$$

Where $r_1^{s,p,v}$ and $r_2^{s,p,v}$ are the reflectivity coefficients of the top and bottom mirrors of the microcavity, respectively. The power emitted toward the back mirror can be calculated by permutation of bottom and top indices ($r_2^{s,p,v} \leftrightarrow r_1^{s,p,v}$) in the above expressions.

Only the power (or EL intensity) emitted in the source medium n_S with angles θ smaller than the critical angle $\theta_c = arcsin(n_{air} sin\theta / n_S)$, where n_{air} is the refractive index of outside medium, can be extracted outside the microcavity (see Fig. 2.5 in Sec. 2.2.2). The interval $[0, \theta_c]$ corresponds to the escape window of the emission. If $\theta > \theta_c$, then, the light will undergo a total internal reflection. The extracted, guided and leaky light are defined as follows:

$$P_{extraction}^{s,p,v} = P_{front}^{s,p,v} \quad for \quad 0 \leq \theta \leq \theta_c \tag{2.72}$$

$$P_{guide}^{s,p,v} = P_{front}^{s,p,v} \quad for \quad \theta_c < \theta \leq \pi/2 \tag{2.73}$$

$$P_{leaky}^{s,p,v} = P_{back}^{s,p,v} \quad for \quad 0 < \theta \leq \pi/2 \tag{2.74}$$

There are two kinds of dipole models that are particularly interesting: isotropic dipoles and in-plane dipoles.

$$P_{isotropic} = \frac{1}{3} \left[P_{front}^s + P_{front}^p + P_{front}^v \right], \quad P_{in-plane} = \frac{1}{2} \left[P_{front}^s + P_{front}^p \right] \tag{2.75}$$

Usually, for a bulk active region and small LED devices, the dipole distribution is isotropic. For quantum well active regions and heavy hole-electron transitions in semiconductor LEDs, as well as in polymer-based organic LEDs, the in-plane dipole formulas should be used. In general, the light power P_{front} should be calculated using the general formula:

$$P_{front} = \frac{\alpha_s P_{front}^s + \alpha_p P_{front}^p + \alpha_v P_{front}^v}{\alpha_s + \alpha_p + \alpha_v} \tag{2.76}$$

Various dipole models can be obtained by properly adjusting the coefficients α_s, α_p and α_v.

The extracted, guided and leaky modes are given by the ratios between the light emitted in the respective windows and the total light emitted by the dipoles (see Fig.2.5a):

$$\eta^{s,p,v}_{extraction} = \frac{\int^{\theta_c} 0 sin\theta d\theta \int_{-\infty}^{\infty} d\lambda P^{s,p,v}_{front}(\theta,\lambda)}{\int_0^{\pi/2} sin\theta d\theta \int_{-\infty}^{\infty} d\lambda \left[P^{s,p,v}_{front}(\theta,\lambda) + P^{s,p,v}_{back}(\theta,\lambda)\right]} \tag{2.77}$$

$$\eta^{s,p,v}_{guide} = \frac{\int_{\theta^c_{emit}}^{\pi/2} sin\theta d\theta \int_{-\infty}^{\infty} d\lambda P^{s,p,v}_{front}(\theta,\lambda)}{\int_0^{\pi/2} sin\theta d\theta \int_{-\infty}^{\infty} d\lambda \left[P^{s,p,v}_{front}(\theta,\lambda) + P^{s,p,v}_{back}(\theta,\lambda)\right]} \tag{2.78}$$

$$\eta^{s,p,v}_{leaky} = \frac{\int_0^{\pi/2} sin\theta d\theta \int_{-\infty}^{\infty} d\lambda P^{s,p,v}_{back}(\theta,\lambda)}{\int_0^{\pi/2} sin\theta d\theta \int_{-\infty}^{\infty} d\lambda \left[P^{s,p,v}_{front}(\theta,\lambda) + P^{s,p,v}_{back}(\theta,\lambda)\right]} \tag{2.79}$$

Based on this theory the extracted electroluminescence intensity as a function of wavelength and angle can been calculated. The optical constants of the materials of the active layer and the DBRs (Si, SiO_2 and a-Si) used in the calculation have been taken from Palik [95]. The location of the center of the emitting zone x is defined as the distance between the emitting zone center and the emitting layer/bottom mirror interface, assuming that the light beam comes out from the top mirror. In the simulation of the light output the emitting zone is located in the middle of the active layer and has a width of $d_{EZ} =$ 20 nm. A normalised measured EL spectrum of a Si pn-diode taken from [89] shown in Fig. 2.10 (Sec. 2.3) with the full width at half maximum (FWHM) of 110 nm and the maximum located at the wavelength 1138 nm has been taken as an input (EL_0) for the calculation.

In order to evaluate the enhancement of the EL due to the microcavity effect, the calculation of the extracted EL was done for the (bulk) Si-LED, where the emitting layer is placed on a crystalline silicon substrate (at 162.34 nm bellow the Si surface) and for the Si-MCLED with the emitting layer placed between two DBRs (Fig. 2.23). Figures 2.23a and 2.23b show the extracted EL as a function of the wavelength and the angle of Si-LED and Si-MCLED, respectively. In Fig. (c) and (d) EL intensity is plotted as a function of the wavelength at angle θ' = 0°. The extracted EL maximum of the Si-LED (c) is situated at the wavelength λ = 1138 nm, has a FWHM of $\Delta\lambda$ = 110 nm and its intensity is 0.055 a.u. As expected, in the case of Si-MCLED (d), there is a very narrow EL peak (FWHM $\Delta\lambda$ = 1 nm) at the resonant wavelength λ_{res} = 1150 nm with a strongly increased emission (EL) intensity (I = 102 a.u.). Figures (e) and (f) show the plots of the extracted EL as a function of the angle for the wavelength λ = 1150 nm. The inset polar plot in Fig. (e) show a lambertian emission pattern typical for planar semiconductor light emitters. The resonance wavelength 1150 nm of the microcavity enhanced LED emits in a very confined angular range $\theta' \approx \pm 10°$.

The main results of the calculations of the MCLED can be summarized as follows:

1. The maximum of the calculated extracted EL intensity is at the resonant wavelength 1150 nm and at the angle of 0° and has a very small FWHM of only 1 nm. With increasing angle the light is emitted only at certain angles and with lower intensities. Also the emission wavelength shifts to the smaller wavelength3 from 1150 nm at 0° to 1050 nm at 88°.

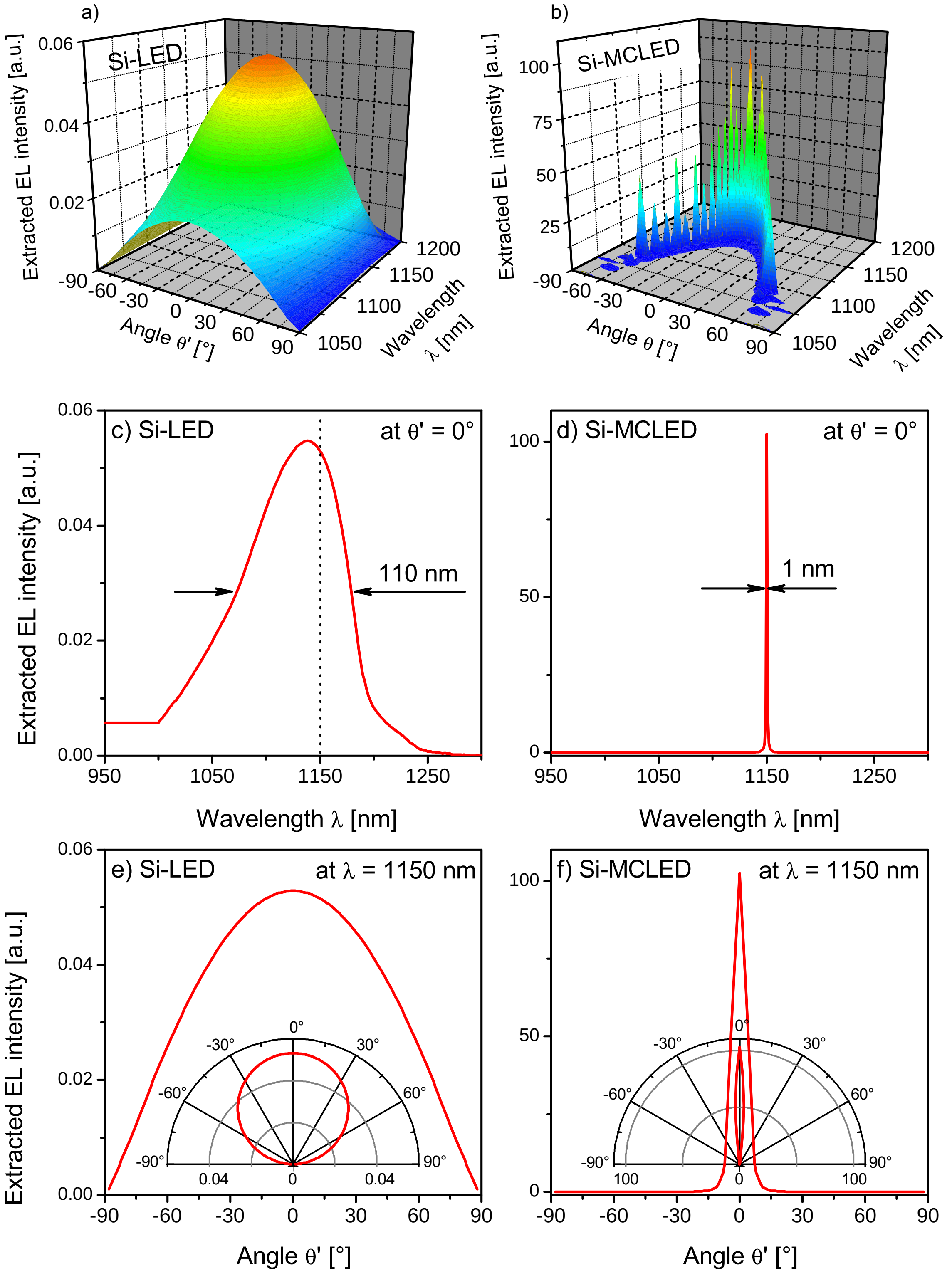

Figure 2.23: Calculated extracted EL intensity of a) Si-LED and b) Si-MCLED in dependence on the wavelength and the angle. Extracted EL intensity as a function of the wavelength at angle $\theta' = 0°$ of c) Si-LED and d) Si-MCLED. e), f) EL as a function of the angle for the wavelength $\lambda = 1150$ nm of the Si-LED and Si-MCLED, respectively. The insets show the corresponding polar plots.

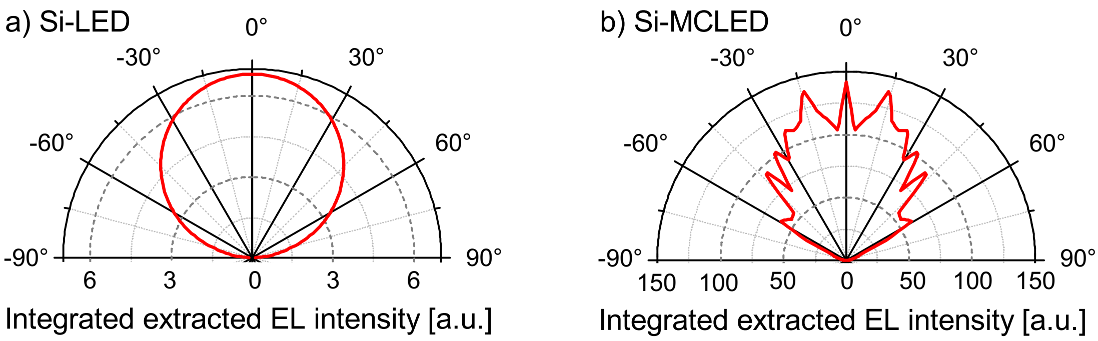

Figure 2.24: a) Extracted EL intensity integrated over the wavelength range (950 nm…1300 nm) as a function of the angle calculated for a) Si-LED and b) MCLED.

2. Using Eq. 2.50 the quality factor $Q = 1150$ and the cavity finesse $F \approx 575$ were calculated.

3. In comparison to conventional Si-LEDs the enhancement of the calculated extracted EL intensity of the MCLED at the resonant wavelength and at the direction perpendicular to the surface is $G_e = 1930$.

4. The emission enhancement in the same direction ($\theta' = 0°$) integrated over the wavelength range 1000 …1300 nm is supposed to be $G_{int}(\lambda) \approx 20$ and enhancement integrated over the whole angle and wavelength range is $G_{int}(\lambda, \theta') = 10$.

5. The external quantum efficiency is equal to the internal quantum efficiency multiplied by the extraction efficiency (Eq. 2.26). UniMCO is able to calculate only the extraction efficiency (Eq. 2.77). For the given system the calculated light extraction efficiency is equal to $\eta_{extraction} = 26\%$, which is about nine times higher than the extraction efficiency of a typical bulk Si-LED $\eta_{extraction} = 3\%$. The remaining light is guided in the active layer in the direction parallel to the surface or leaky - absorbed by the substrate (Si-LED: $\eta_{leaky} = 97\%$; Si-MCLED: $\eta_{guided} = 36\%$, $\eta_{leaky} = 38\%$).

Chapter 3

Preparation and characterisation methods

There are two main groups of experimental techniques used in this work. One part contains the preparation techniques used in the diode processing, including deposition of distributed Bragg reflectors. The second group includes analytical methods for optical, electrical and structural characterisation of the devices.

3.1 Preparation techniques

In order to fabricate microcavity enhanced silicon based pn-diodes (Si-MCLED), more than 40 process steps have been carried out. The used CMOS compatible techniques are described in this section.

- The pn-diodes have been produced by silicon planar technology containing:
    1. thermal oxidation,
    2. photolithography,
    3. etching (SiO_2 , Al, Si_3N_4, Si substrate),
    4. ion implantation,
    5. metallisation (PVD sputter deposition)
    6. PECVD of passivating Si_3N_4 layers.
- Distributed Bragg reflectors consisting of multilayers of SiO_2 and a-Si, forming an optical resonator, have been deposited by magnetron sputtering (PVD).

3.1.1 Thermal oxidation of silicon

Thermal oxidation of silicon is one of the most fundamental processes in semiconductor manufacturing, playing a crucial role in the development of the semiconductor planar processes. Although industry has nowadays started to replace silicon dioxide with other specialized dielectric materials for some applications [108], silicon oxidation is still indispensable to form easily a high quality interface between silicon dioxide and silicon substrate with low density of interface states [109].

In the process of the device (Si-MCLED) preparation, the SiO_2 layers have been used for surface passivation, isolation between Al contacts and the substrate and as implantation mask. Oxidation and subsequent SiO_2 etching have also been employed for precise thinning of the device Si layer on the SOI wafer.

The thermal oxidation of SiO_2 proceeds by exposing the silicon substrate to an oxidizing environment of O_2 or H_2O at elevated temperature (usually between 700-1200°C), producing oxide films whose thicknesses range from 5 to 1500 nm. Oxidation of silicon is not difficult, since silicon has a natural inclination to form a stable oxide even at room temperature, as long as an oxidizing ambient is present. The elevated temperature used in thermal oxidation therefore serves primarily as an accelerator of the oxidation process, resulting in thicker oxide layers per unit of time.

Depending on which oxidant species are used (O_2 or H_2O), the thermal oxidation of SiO_2 may either be in the form of *dry oxidation* (where the oxidant is O_2)

$$Si(solid) + O_2(vapour) \rightarrow SiO_2(solid) \tag{3.1}$$

or *wet oxidation* (where among O_2 the fast oxidant is H_2O). The reactions for dry and wet oxidation are governed by the following equations:

$$Si(solid) + 2H_2O(vapour) \rightarrow SiO_2(solid) + 2H_2(vapour) \tag{3.2}$$

During dry oxidation, the silicon wafer reacts with the ambient oxygen, forming a layer of silicon dioxide on its surface. During wet oxidation, oxygen gas is introduced into the chamber with the distilled water heated to 95°C - bubbler (see fig. 3.1). Molecules of O_2 and H_2O enter then the furnace, where they diffuse toward the wafers. They react with the silicon to produce the oxide and another reaction product, i.e., hydrogen gas [110].

These oxidation reactions occur at the Si-SiO_2 interface, i.e., silicon at the interface is consumed as oxidation takes place. As the oxide grows, the Si-SiO_2 interface moves into the silicon substrate. The amount of silicon consumed by the formation of silicon dioxide is also fairly predictable from the relative densities and molecular weights of Si and SiO_2, i.e., the thickness of silicon consumed is 44% of the final thickness of the oxide layer. Thus, an oxide that is 100 nm thick will consume about 44 nm of silicon from the substrate [110].

In 1965 Deal and Grove [111] postulated the so called *Linear and Parabolic Growth Laws*, also known as the Linear Parabolic Model. This oxide growth model has been empirically proved to be accurate over a wide range of temperatures (700-1300°C), oxide thicknesses (30-2000 nm), and oxidant partial pressures (0.2-25 atmospheres).

According to the Deal-Grove equation [111], the oxide thickness x_0 increases linearly with time for relatively small oxidation times $x_o = C(t + \tau)$, where C is the linear rate constant and τ is the initial time displacement. This is the linear regime, in which the rate-limiting process is the interfacial oxidation reaction.

At longer oxidation times t, the limiting process is the diffusion of the oxidant (O_2 or H_2O molecule) through the growing SiO_2 , and the thickness increases parabolically with time $x_0^2 = B.t$. This is the parabolic regime, showing that the oxide thickness is proportional to the square root of the oxidation time, which means that the oxide growth is hampered as the oxide thickness increases. This is because the oxidizing species has to diffuse a greater length to the Si-SiO_2 interface as the oxide layer thickens increases [110].

The oxide growth depends on oxidation time, atmosphere, oxidation temperature, or oxidation pressure. Other factors that affect thermal oxidation growth rate for SiO_2

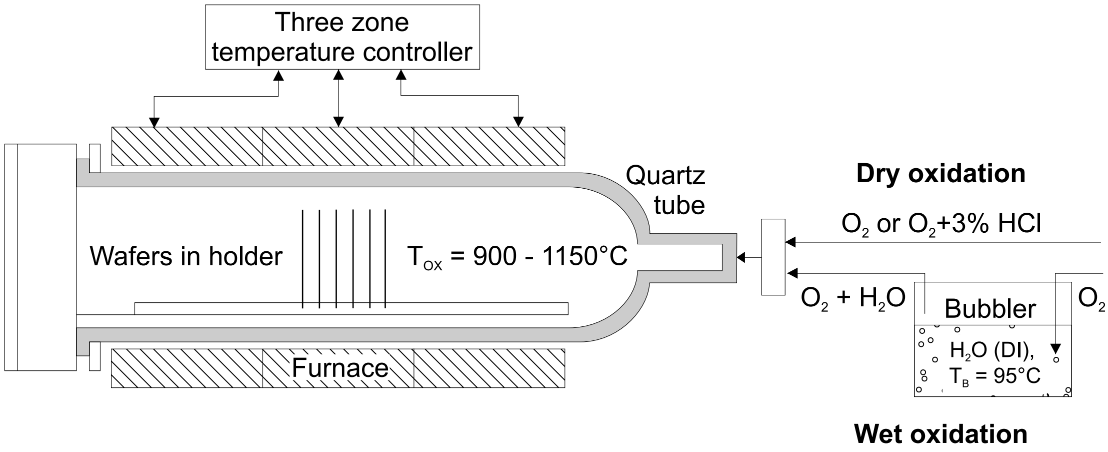

Figure 3.1: Schematic illustration of the wet and dry oxidation process in the horizontal furnace INOTHERM.

include the crystallographic orientation of the silicon wafer, the wafer doping level and the presence of halogen impurities in the oxidation ambient. For high quality oxides, dry oxidation O_2 +5% HCl is used.

Horizontal Furnace with three quartz tubes INOTHERM

Thermal oxidation and annealing have been performed in the horizontal furnace INOTHERM. The furnace operates in the temperature range of 300 – 1150°C. Possible process gases are O_2 (wet and dry oxidation), O_2 + HCl, N_2, N_2 + 5% H_2, Ar + 7% H_2 (all of 5.0 purity). The quartz tubes are built for 25 wafers with max. diameter of 150 mm (Fig. 3.1).

The furnace is used for three basic processes:

1. Dry oxidation - high quality gate oxides, $d_{ox} = (10–250)$ nm.
2. Wet oxidation - growth of thick field oxides with $d_{ox} = (200–1500)$ nm.
3. Annealing - of radiation defects after ion implantation, activation and diffusion after implantation, metal contact formation.

3.1.2 Photolithography

The fabrication of circuits on a wafer requires a process by which specific patterns of various materials can be deposited on or removed from the wafer's surface. The process of defining these patterns on the wafer is known as photolithography.

Optical Lithography refers to a lithographic process that uses ultraviolet light to form patterns in the photoresist through exposure, also called photolithographic patterning. Photolithographic patterning is the process of projecting the image of the mask patterns onto the wafer surface using a light source and a glass mask [110].

Masks, composed of patterned chromium layer on glass substrate, are used during exposure to cover areas of the photoresist layer that shouldn't get exposed to light (Fig. 3.2a). Development of the photoresist in a developer solution after its exposure to light produces a resist pattern on the wafer, which defines which areas of the wafer are exposed for material removal (Fig. 3.2b).

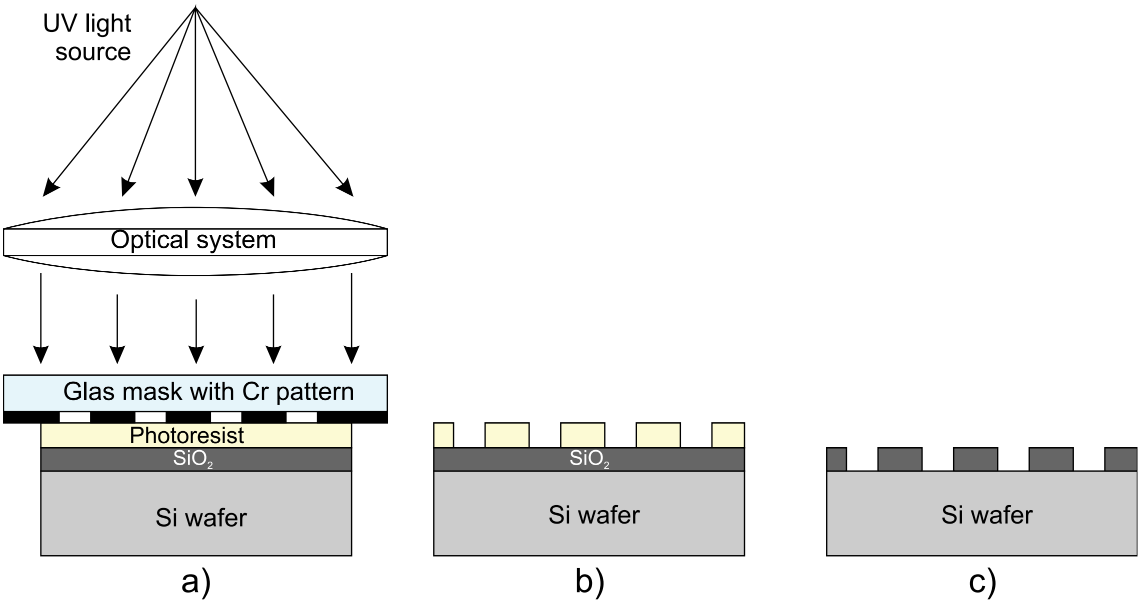

Figure 3.2: a) Contact photolitography, b) development of the photoresist, c) etching and resist stripping.

There are three types of photolithographic patterning - contact, proximity and projection exposure. In this work the contact mode was applied.

Contact photolitography refers to the light exposure process where the photomask is pressed against the resist-covered wafer with a certain degree of pressure. This pressure is typically in the range of 0.05 - 0.3 atmospheres. Light with a wavelength of about 400 nm is used in contact photolitography.

Contact photolitography also results in defects in both the masks used and the wafers, necessitating the regular disposal of masks (whether thick or thin) after a certain level of use. Mask defects include pinholes, scratches, intrusions, and star fractures. Despite these drawbacks, however, contact exposure continues to be widely used. After all, good contact photolithographic patterning processes can achieve resolutions of 0.5 - 1 μm or better.

For photolithographic patterning the Mask-Aligner MA4 (SÜSS) has been used, which is able to pattern wafers up to 100 mm diameter. This equipment was applied for one- and two-sided photolithographic patterning of Al, Si and SiO_2 films on silicon and SOI substrates.

3.1.3 Wet chemical cleaning and etching

- **Cleaning** with Piranha solution. It is a mixture of sulfuric acid (H_2SO_4) and hydrogen peroxide (H_2O_2). The Pirhana is used to clean organic residues off silicon substrates. Because the mixture is a strong oxidizer, it will remove most organic matter, and it will also hydroxylate most surfaces (add OH groups), making them extremely hydrophilic (water compatible). The standard acid piranha used is a 3:1 mixture of concentrated sulfuric acid (H_2SO_4) with hydrogen peroxide (40% H_2O_2). Acid piranha is a self starting reaction and is extremely exothermic; this mixture becomes hot when the sulfuric acid is added into the hydrogen peroxide [112].

- **Etching** selectively removes thin films and results in desired thin film patterns. The etch mask is usually photo-resist or an oxide/nitride prepatterned layer. Multilayered systems can be etched sequentially using the same etching masking layer. Basically there are two main kinds of etching: *wet etching* [113–116] using liquid etchants and *dry etching* [117–131] using gas phase etchants in a plasma. During the diode fabrication in this work, only wet etching processes, available at the processing in the clean room, have been used.

Etching of SiO_2 in HF

Wet HF etching of SiO_2 is an isotropic process, where the addition of ammonium fluoride NH_4F creates a buffered hydrofluoric acid HF solution (BHF) also called buffered oxide etch (BOE). NH_4F controls the pH value and replenishes the depletion of the fluoride ions, thus maintaining stable etch rate.

Three main uses of BOE are:

1. to remove unwanted silicon dioxide on patterned silicon wafers, see fig. 3.2 c (e.g. windows opening for B^+ and P^+ ion implantation into the silicon substrate in order to form a pn-junction),
2. to remove native silicon dioxide on silicon wafers before thermal oxidation or contact metal deposition,
3. to remove the underlying sacrificial oxide layer of suspended microstructures on silicon wafers.

While the removal of parasitic oxide is relatively straight forward, the timing issue in releasing microstructures can be critical and requires great care. The BOE process is based on the reaction [132]:

$$SiO_2 + 6HF \rightarrow H_2SiF_6 + 2H_2O \tag{3.3}$$

where H_2SiF_6 is soluble in water. This reaction is performed in a dilute solution of HF (40%, 100 ml), buffered with NH_4F (40%, 220 ml) mixed with 680 ml H_2O to avoid depletion of the fluoride ions. The etching is performed at room temperature. Buffering of the hydrofluoric acid also lessens the attack of the photoresist [132]. Both thermally grown and deposited SiO_2 can be etched in buffered hydrofluoric acid. However, etching of deposited SiO_2 films proceeds faster than that of the thermal oxide. Heat treatment of the deposited SiO_2 films at 1000-1200°C for about 15 minutes results in a decrease in the etch rate to approximately the same as that for the thermally grown oxide (75 nm/min). The etch rate of Si_3N_4 in buffered HF, 200 nm/h, is negligible compared to the etch rate of SiO_2 .

Etching of Al

The aluminum metalization and etching process using photo-lithographic techniques is basic to semiconductor and microelectronic technology. The aluminum etchant consists of a mixture of phosphoric acid (760 ml 85% H_3PO_4), acetic acid (150 ml 100% HAC), nitric acid (30 ml 69% HNO_3) and 50 ml water. It is highly compatible with commercial photoresists and permit delineation into high resolution patterns. This etchant do not attack silicon, silicon dioxide, silicon nitride or nichrome resistor films. The etch rate of this solution is about 2 μm/min, at 40°C.

Etching of Si_3N_4

Thin films of amorphous silicon nitride (Si_3N4) were produced by PECVD. The importance of patterned nitride layers is to protect SiO_2 layers and silicon substrate during long time deep anisotropic KOH etching, where the SiO_2 masks cannot be used.

The etching rate of SiO_2 in KOH is 300 - 500 times slower than the etching rate of (100)-silicon, and in most cases a SiO_2 mask can be used successfully. However, a very deep anisotropic and selective etch may require a long etching time, and the (300...500):1 etching rate ratio may be still too small to prevent the removal of the SiO_2 mask before the process is completed. Under such circumstances Si_3N4, thank to its reduced etched rate, can successfully replace the oxide mask layer.

The wet etching of nitride films is often performed in concentrated hot phosphoric acid (85% H_3PO_4). The bath temperature is 160°C, with a corresponding etch rate around 4 nm/min. It is good practice to bring the vapours into contact with a cold surface and to drive the condensed liquid back into the etching bath. This technique is referred to as reflux.

Etching of Si in KOH

Heated Potassium Hydroxide solution (30% KOH) is used as an anisotropic wet etchant which attacks silicon preferentially in the <100> direction, producing a characteristic anisotropic V-etch, with sidewalls that form a 54.7° angle with the surface (35.3° from the normal). This etch process is independent of the doping concentration for As, P and Sb. For B, the etch rate in the <100> direction drops quickly at high boron doping concentrations ($> 5.10^{19}$cm^3). In order to create thin (1-2 μm) membranes, we have etched the back side (Si substrate) of SOI wafers using the buried oxide layer (BOX) as an etch stop. Normal etch rates of (100) n-Si by 80 °C are about 1 μm/minute. Long-time KOH etching (> 5 h) requires a *hard mask*. Silicon nitride is for this purpose preferred since oxide is also slowly etched by KOH with an etch rate of about 200 nm/h.

3.1.4 Ion implantation

Ion implantation is a high technology approach for modifying surface properties of materials. Ion implantation uses highly energetic beams of ions (positively or negatively charged atoms) to modify surface structure and chemistry of materials. The process does not adversely affect macroscopic dimensions or bulk material properties, but it creates near surface damage along the penetration path of the ions in matter.

Ion implanters are essential for modern integrated-circuit (IC) manufacturing. To create active circuit elements (transistors, diodes...), impurities (arsenic, phosphorus, boron, indium, antimony, germanium,...) must be selectively introduced to create n-type and p-type regions. The impurities are introduced into unprotected areas of the wafer at room temperature by accelerating dopant ions (atoms stripped of one or more of their electrons) to a high energy so they are driven into the wafer and become embedded. The depth at which the ions become to rest depends on their mass and energy. As the dopant ions penetrate into the silicon they damage the crystal due to the collisions with the target atoms (collisional cascades). However, some of this damage can be removed in a subsequent treatment process (annealing). Ion implantation allows accurate control of the dopant concentration and the depth distribution by selection ion current density, fluence and energy through an oxide layer if desired. It allows the introduction of the impurities by diffusion in the thermal equilibrium.

In order to fabricate high quality pn-junctions, the ion implantation has been used for controlled doping of the silicon substrate with B^+ and P^+ ions. The implantation of B^+ was performed at the 50 kV Low Energy Ion Implanter DANFYSIK 1050, which operates in the energy range of 0.5 keV – 40 keV. The upper current limit is 5 mA. The whole process takes place in high vacuum. P^+ ions were implanted at the 500 kV Ion Implanter, which provides ions in the energy range 30 keV – 500 keV.

3.1.5 Plasma Enhanced Chemical Vapour Deposition (PECVD) of silicon nitride

Plasma-enhanced chemical vapour deposition (PECVD) is a technique commonly used in microfabrication to deposit layers of insulating materials and amorphous or polycrystalline silicon. The plasma is used to stimulate a reaction on the Si substrate surface of two or more species from the gas phase. The plasma helps break down the precursor molecules and allows the reaction to occur at a lower temperature than conventional CVD. The major advantage of PECVD, in fact, consists in its lower temperature capability with respect to other system as conventional CVD. For example, while deposition temperatures of 700-900°C are required for silicon deposition in CVD, temperatures in the range 250-350°C are sufficient in PECVD systems [133–135].

In this work the PECVD process has been used for deposition of Si_3N_4 films, that work as pasivation layers during deep anisotropic etching of silicon. The deposition was performed in cooperation with the Gesellschaft für Silizium-Mikrosysteme mbH (GeSiM).

3.1.6 Magnetron sputter deposition

The sputtering process and apparatus has been patented by Chapin in 1979 [136]. Magnetrons are routinely used to rapidly deposit thin metal, dielectric and compound films in a broad range of applications, from architectural glass and food packaging to thin film microelectronics. Magnetron-like effects are also used in high-rate sputter and reactive etching devices. One of the most useful description available has been the work of Thorton and Penford [137].

Magnetrons are cold cathode discharge devices generally used in a diode mode. The plasma is initiated between the cathode and the anode at gas pressures in the mTorr range by the application of a high voltage. In the direct current (dc) sputtering mode a negative bias potential of some hundred Volts is applied to the target, while the chamber is grounded. As a result, positive Ar^+ ions are accelerated toward the target. Bombardment of the target surface by Ar^+ ions leads to collisions with the target atoms. The material of the target is detached (sputtered) and secondary electrons are produced. The advantage of a magnetron cathode in comparison with a conventional diode cathode is the presence of a magnetic field. The magnetic field in the magnetron is oriented parallel to the cathode surface.The polarity of the magnetic field is oriented such that the $E \times B$ drift paths of the emitted secondary electrons form a closed loop (Fig. 3.3a) [123]. Due to the increased confinement and dwell time of the secondary electrons in this $E \times B$ drift loop, the probability of ionization of Ar ions increases. The plasma density will be much higher, often by an order of magnitude or more, compared to a conventional diode device. The result of the high plasma density and its proximity to the cathode is a high current and

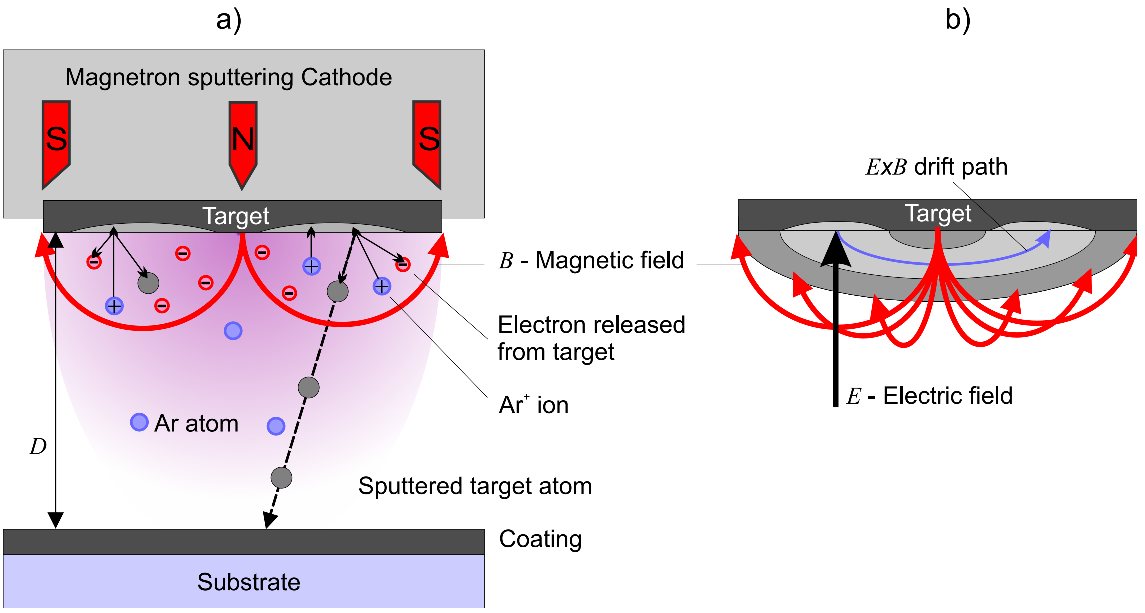

Figure 3.3: (a) Principle of magnetron sputter deposition with (b) circular planar magnetron (cross section of 3D view) [123].

relatively low voltage discharge at a lower operation pressure, which favors the formation of smooth and dense films. On the other hand the magnetron significantly reduces the electron bombardment of the substrate surface. High discharge currents allow to sputter the cathode at a high rate up to several microns per a minute for high sputter yield materials. Usually, the limiting factor for the maximum deposition rates in magnetron devices is the effective cooling of the cathode and the target.

The deposition tool Nordiko 2000

For sputter deposition of the thin films of Si and SiO_2 as well as Al contact layers a commercial sputter tool Nordiko 2000 (Fig. 3.4) has been used. It consists of four magnetrons. Each magnetron is equipped with a different 8 inch target (Si, SiO_2 , Al). The targets are situated on the top of the chamber (on the chamber lid) above a rotatable substrate table with four substrate holders (two water cooled, two heatable up to 500°C, one of the latter equipped with a thermocouple) for wafers with maximum 8 inch diameter. Two of the four magnetrons operate in dc mode (used for deposition of conductive materials: polycrystalline Si, Al), the other two are powered either in dc or in rf mode (for sputtering of insulators: fused silica). Simultaneous operation of one dc (up to 5 kW plasma power) and one rf magnetron (13.6 MHz, up to 2 kW) is possible. The central and the ring shaped outer magnets generate a fixed ring-like race track-region (Fig. 3.3b). Regions with low erosion rate are in the center and at the boundary edges of the target. The approximate partial pressures of gases are determined by means of a micropole sensor system (Ferran Scientific). Since the tool geometry did not enable an in-situ thin film analysis, the thin films were analyzed ex-situ.

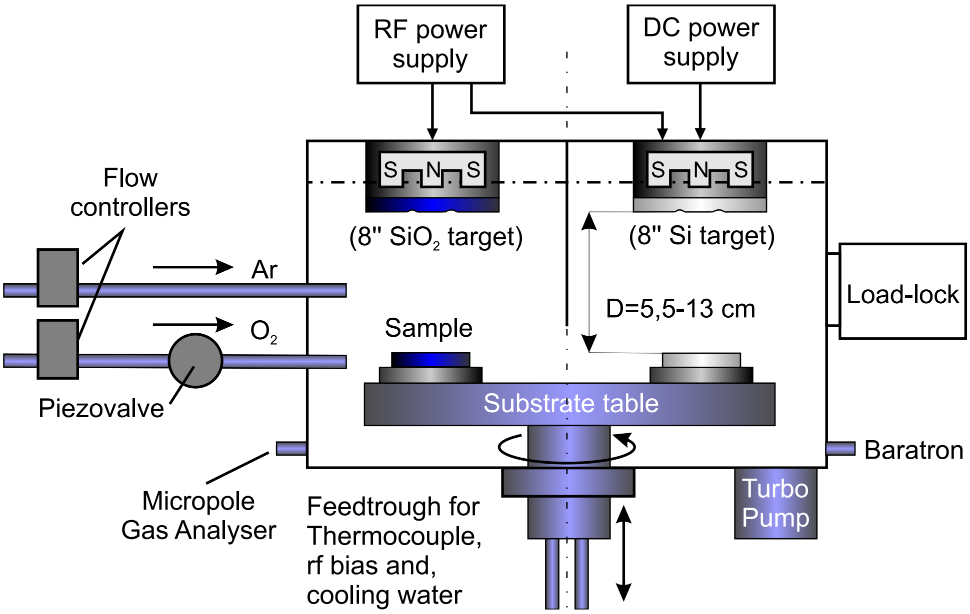

Figure 3.4: Schematic cross section of commercial sputter chamber NORDIKO 2000.

3.2 Characterization techniques

The optical chracterisation of the deposited Si/SiO$_2$ layers forming the distributed Bragg reflectors was performed by Variable Angle Spectroscopic Ellipsometry (VASE) and Fourier Transform Infrared Spectroscopy (FTIR). Electrical and electo-optical properties of the final devices were measured at the electroluminescence setup described later in this section. The structure was investigated by atomic force, light and electron microscopy.

3.2.1 Variable Angle Spectroscopic Ellipsometry (VASE)

Ellipsometry is a powerful tool for the characterisation of thin films and multi-layer structures. Ellipsometry uses the change in polarisation of light upon reflection from (or, less commonly, transmission through) a material to determine the real part (refractive index), $n(\lambda)$ and the imaginary part (extinction coefficient), $k(\lambda)$ of the complex refractive index of a material, $N(\lambda) = (n(\lambda)+ik(\lambda))$ where λ is the wavelength of the electromagnetic radiation (Fig. 3.5). Linearly polarised light at non-normal angles of incidence becomes elliptically polarised upon reflection from the material. The ellipticity, or ratio of minor to major axis of the ellipse, and the orientation of the reflected beam are determined by the relative phase difference Δ and azimuth angle Ψ. In reflection mode, the Fresnel reflection coefficient ratio ρ is measured:

$$\rho = r_p/r_s = tan(\Psi)e^{i\Delta} \tag{3.4}$$

The quantity r$_p$ (r$_s$) is the Fresnel reflection coefficient for light polarized parallel (perpendicular) to the plane of incidence. The ellipticity of the reflected light depends on the optical constants of the thin film and its thickness . Knowledge of the complex refractive index for a given material allows the thickness of various films of the same material to be determined and, with care, more complex multi-layered structures to be characterised. This generally requires Variable Angle Spectroscopic Ellipsometry (VASE), where both

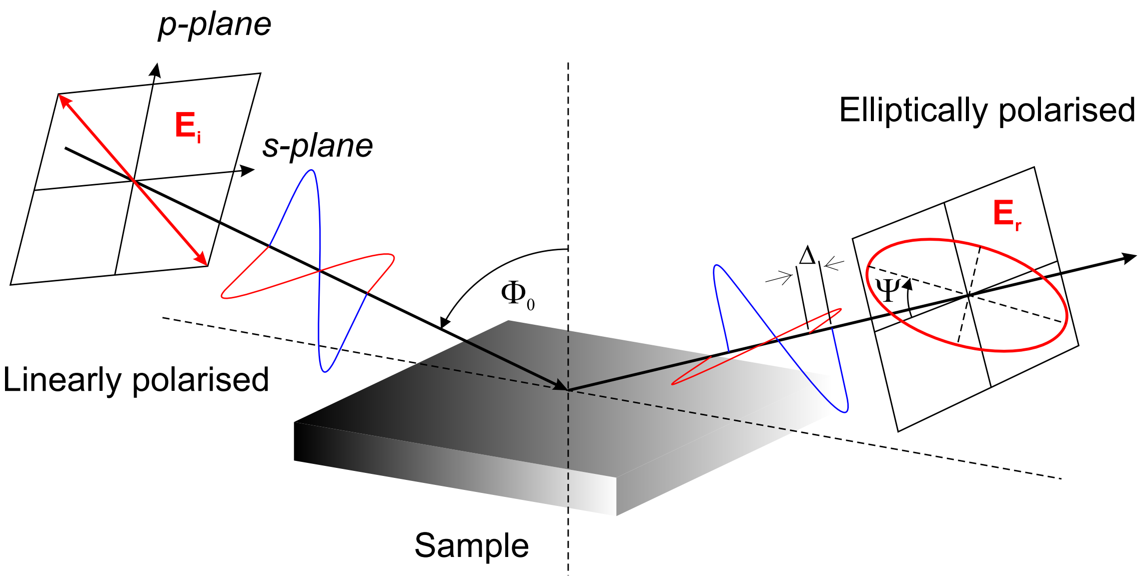

Figure 3.5: Linearly polarised light is generally elliptical polarised upon reflection with asymmetric intensity difference ($tan\Psi$) and phase difference (Δ).

the incident angle of the light and the wavelength can be varied to produce a greater range of data from and to model the response of the system. Thin film characterisation using spectroscopic ellipsometry generally requires a model of the optical response of the thin film and substrate to be built, which is then compared with the experimental data, in the form of the historical ellipsometric parameters $tan\Psi$ and $cos\Delta$. Ellipsometric measurements were made by using a variable angle spectroscopic ellipsometer by Woollam (VASE^{TM}). The detailed models used for parametrization of optical constants of deposited films and multilayered systems are described in appendix A.1.

3.2.2 Fourier Transform Infrared Spectroscopy (FTIR)

Infrared spectroscopy provides a reliable method for rapid, non-destructive quantitative analysis. The technique of Fourier transform infrared (FTIR) reflectometry has been advanced to characterize the thickness and optical properties of thin films commonly used in advanced integrated circuits. It is based on a Michelson Interferometer. An interference pattern is produced by splitting a beam of light into two paths, bouncing the beams back and merging them. A movable mirror accomplishes this. The beam splitter is usually a mirror with 50% surface reflectivity and 50% transparency. One-half of the light goes straight through the beam splitter to the movable mirror and one-half of the light it reflected upwards to the fixed mirror. These two half-intensity beams are then reflected back to the beam-splitter where once again each is split into two beams which are 25% the intensity of the incident beam. Two these 25% intensity beams interfere and emerge from the interferometer in the direction of the detector and two in the direction of the original incident beam. The reflectivity spectra is created through Fourier transformation of interferogram.

Reflectance measurements have been performed by a Fourier transform infrared spectrometer (FTIR) Bruker Equinox 55 using a Tungsten lamp, a Quartz beam splitter and an InGaAs detector for the near infrared wavelength region. The standard spectral res-

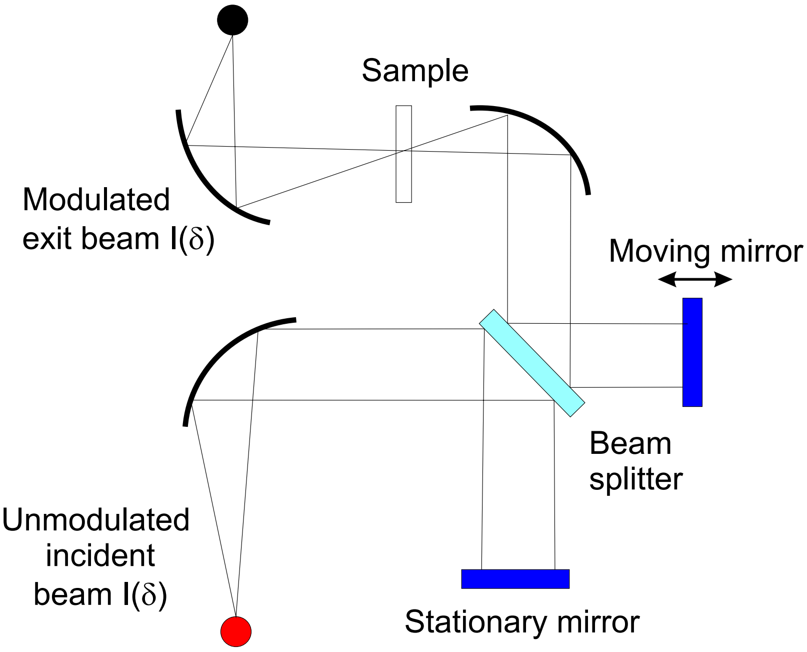

Figure 3.6: Principle of Michelson interferometer.

olution of better than 0.5 cm^{-1} is suitable for most applications. As a reference a silver metal mirror has been used.

SCOUT spectrum simulation software

The goal of optical spectroscopy is the determination of macroscopic quantities such as thin film thicknesses and microscopic quantities such as resonance frequencies from the experiments. This is possible if the microscopic phenomena are coupled to the electric fields of the probing radiation. The key property of a material representing this connection is the dielectric function or its square root, the complex refractive index [138].

It is also a very powerful technique to interpret experimental optical spectra of the multilayered systems by a simulation based on a physical model and adjustment of the model parameters in order to fit it to the measured data. Fortunately, rather simple models of dielectric functions lead to a realistic simulation of optical spectra. This enables quick parameter fits from which the wanted information can be obtained.

The simulation of optical spectra is the central task of SCOUT, which is a Windows 98/2000/NT/XP software for the analysis of optical spectra by comparison of measurements and models. This software is able to simulate the reflectance, transmittance, absorbance, ATR, ellipsometry, photoluminescence electric field distribution and local absorption [138].

Model calculations are based on:

1. **Optical constant models** (Classical Drude model for free carriers, enhanced Drude model with frequency-dependent carrier damping, harmonic oscillators, extended oscillator model due to Brendel, extended oscillator model due to Kim, OJL inter-band transition model, Campi-Coriasso inter-band transition model, Tauc-Lorentz inter-band transition model, user-defined expressions for optical constants, imported dielectric functions)

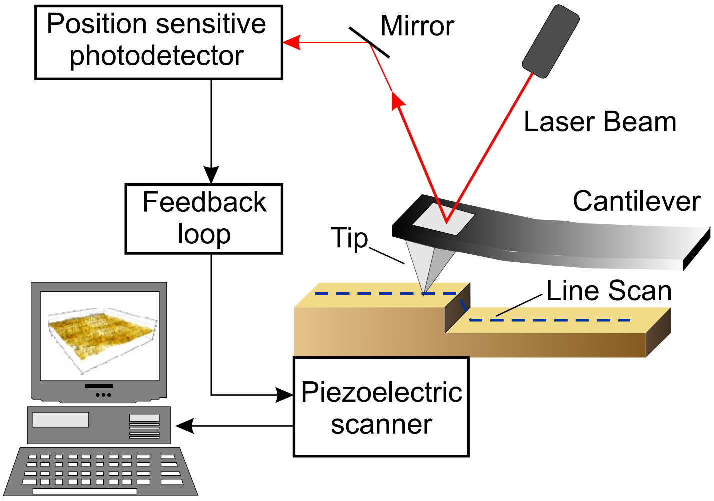

Figure 3.7: Principle of operation of atomic force microscope.

2. **Various effective medium concepts for inhomogeneous materials** (Maxwell, Garnett, Bruggeman, Looyenga, Bergman representation)

3. **Wave propagation in layer stacks** including coherent or incoherent superposition of partial waves, easy definition of superlattices, corrections for scattering losses at rough interfaces; efficient averaging algorithm for lateral layer thickness inhomogeneities; gradually changing optical properties; anisotropic layers and angle of incidence averaging.

3.2.3 Microscopy

Atomic Force Microscopy (AFM)

The Atomic Force Microscope (AFM) is a member of the family of Scanning Probe Microscopes (SPM). This relatively recent technology (invented in 1986 by Binning, Quate and Gerber) is capable of examining many different materials at ultra high resolution in as close to natural environmental conditions as possible. There are no high vacuum or coating requirements and imaging can even be carried out under liquids (including physiological buffer solutions), all at ambient temperature.

The AFM produces images by scanning a tip across the sample and recording the displacement forces experienced (Fig. 3.7). No optical lenses are employed in the image acquisition system, avoiding the theoretical diffraction limit of maximum resolution associated with other types of microscopes. AFM is capable of acquiring images at molecular resolution and may even be successfully used to acquire images of atomic lattice structures with suitable samples. The resolution is sample dependent and samples with very high topographical features (larger than several microns) do require some preparative methods to optimise presentation to the AFM.

AFM is a very versatile technique that allows acquisition of many different data sets from a single sample, providing data on a range of different mechanical properties as well as simply topographical data.

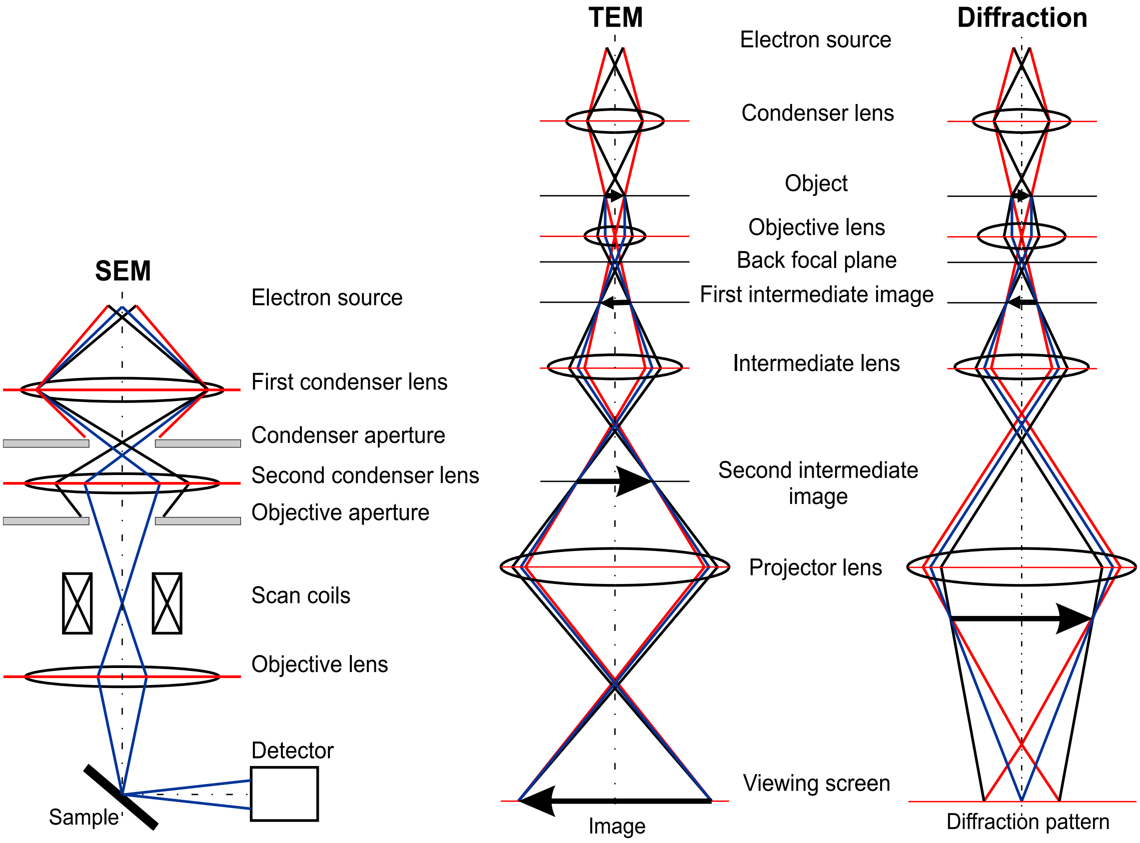

Figure 3.8: Ray diagram.

Scanning Electron Microscopy (SEM)

Scanning electron microscopy is used for inspecting topographies of specimens at very high magnifications and the material contrast. SEM magnifications can go to more than 300,000 x but many semiconductor manufacturing applications require magnifications of less than 3,000 x only. SEM inspection is often used in the analysis of die/package cracks and fracture surfaces, bond failures, cross section investigations on FIB milled samples with high resolution in nanometer range and physical defects on the die or package surface.

During SEM inspection, a beam of electrons is focused on a small area of the specimen, resulting in the transfer of energy to the spot. These bombarding electrons, also referred to as primary electrons, remove electrons from the specimen itself. The removed electrons, also known as secondary electrons, are attracted and collected by a positively biased grid or detector, and then translated into a signal.

To produce the SEM image, the electron beam is scanned across the area being inspected, producing many such signals. These signals are then amplified, analyzed, and translated into images of the topography being inspected.

The energy of the primary electrons determines the quantity of secondary electrons collected during inspection. The emission of secondary electrons from the specimen increases as the energy of the primary electron beam increases, until a certain saturation is reached. Beyond this limit, the collected secondary electrons diminish as the energy of the primary beam is increased, because the primary beam is already activating electrons deep below the surface of the specimen. Electrons coming from such depths usually recombine before reaching the surface for emission.

Aside from secondary electrons, the primary electron beam results in the emission of backscattered (or reflected) electrons from the specimen. Backscattered electrons possess more energy than secondary electrons, and have a definite direction. As such, they can not be collected by a secondary electron detector, unless the detector is directly in their path of travel. All emissions above 50 eV are considered to be backscattered electrons.

Backscattered electron imaging is useful in distinguishing one material from another, since the yield of the collected backscattered electrons increases monotonically with the specimen's atomic number. Backscatter imaging can distinguish elements with atomic number differences of at least 3, i.e., materials with atomic number differences of at least 3 would appear with good contrast on the image. For example, inspecting the remaining Au on an Al bond pad after its Au ball bond has lifted off would be easier using backscatter imaging, since the difference in the atom number of Al and Au is quite big.

An SEM may be equipped with an Energy dispersive X-ray spectroscopy (EDX) analysis system enabling performation of the compositional analysis on specimens. EDX analysis is useful in identifying materials and contaminants, as well as estimating their relative concentrations on the surface of the specimen.

Transmission Electron Microscopy (TEM)

TEM is a unique tool in characterization of materials crystal structure and microstructure simultaneously by diffraction and imaging techniques. In a conventional transmission electron microscope, a thin specimen is irradiated with an electron beam of uniform current density. Unlike the SEM which relies on dislodged or reflected electrons from the specimen to form an image, the TEM collects the electrons that are transmitted through the specimen. Like the SEM, a TEM uses an electron gun to produce the primary beam of electrons that will be focused by a two or three stage condenser lens system into a very thin, coherent beam. An objective lens provides the formation of either image or diffraction pattern of the specimen. The electron intensity distribution behind the specimen is magnified with a three or four stage lens system and viewed on a fluorescent screen. The image can be recorded by direct exposure of a photographic emulsion or an image plate or digitally by a CCD camera. The acceleration voltage of up to date routine instruments is 120 to 200 kV. Medium-voltage instruments work at 200-500 kV to provide a better transmission and resolution, and in high voltage electron microscopy (HVEM) the acceleration voltage is in the range 500 kV to 3 MV. Acceleration voltage determines the velocity, wavelength and hence the resolution (ability to distinguish the neighboring microstructural features) of the microscope. The greatest consideration when performing TEM analysis is sample preparation. The quality of sample preparation contributes greatly to whether the micrograph will be good or not, so analysts are required to exercise the necessary diligence in preparing the sample for TEM analysis.

Electrons of 0.072 Angstrom wavelength at 100 kV excitation transmitted through about 0.1 micrometer thin foil specimen are diffracted according to Bragg's law, $n\lambda = 2dsin\theta \approx 2d\theta$, forming a diffraction pattern (consisting of a transmitted and diffracted beam spots) on the display screen of the microscope. Although the real diffraction phenomena is due to complex interactions of charged electrons with the periodic potential field of the lattice, Bragg's Law or Laue Conditions are sufficient approximations for usual practical applications. A diffraction pattern is, in the simplest sense, a Fourier transform of the periodic crystal lattice, giving us information on the periodicities in the lattice, and hence the atomic positions.

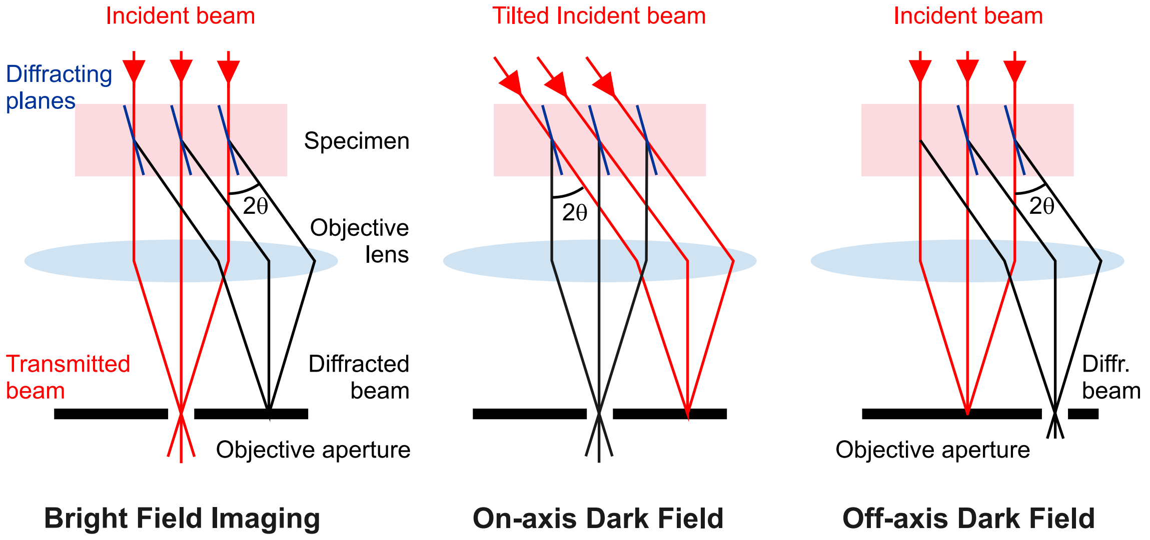

Figure 3.9: Bright field and dark field.

Reciprocal Lattice is a concept, a tool used together with Ewald sphere construction for geometrical interpretation of the Bragg law or Laue conditions that describe the diffraction conditions. According to this, diffraction pattern is the planar section of the reciprocal lattice perpendicular to beam direction, which is also the zone of planes appearing as spots in the pattern.

Electron diffraction patterns produced in transmission electron microscope can be of three different types:

1. Ring Pattern,
2. Selected Area Diffraction Pattern,
3. Convergent-Beam Electron Diffraction Pattern.

The image of the specimen in conventional microscopy, on the other hand, is formed selectively allowing only the transmitted beam (Bright Field Imaging) or one of the diffracted beams (Dark Field Imaging) down to the microscope column by means of an aperture. The origin of the image contrast is the variation of intensities of transmitted and diffracted beams due to the differences in diffraction conditions depending on the microstructural features on the electron path.

3.2.4 Electroluminescence and photoluminescence measurements

The luminescence measurements were performed at two measuring tools:

- Forschungszentrum Dresden-Rossendorf (FZD)

  An electrical characterization of the light emitting devices was performed at the experimental setup depicted in Fig. 3.10. The basis of the setup is the optical microscope Nikon Eclipse E200. The sample is mounted under the extra long working distance objective with magnification of 50x and numerical aperture (NA) of 0.55 and a super long working distance objective with magnification 20x, NA = 0.35. The light is guided through the microscope and coupled into the optical fiber,

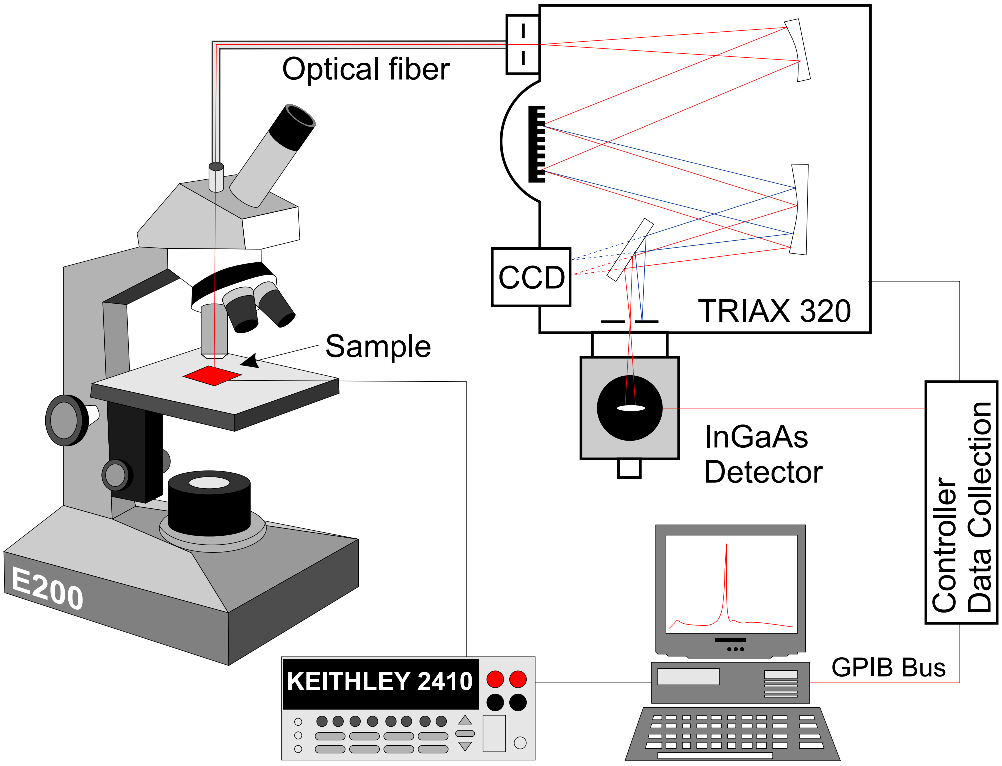

Figure 3.10: Scheme of electroluminescence setup.

which ends in a monochromator Triax Series 320. For detecting of the light intensity in the near infrared region (usually 1000-1300 nm) a nitrogen cooled InGaAs detector is used. A constant dc current is supplied using the Keithley 2410 source. The whole measurement process is controlled by computer.

- Leibniz Institute for Solid State and Materials Research Dresden (IFW)

  The photoluminescence and electroluminescence measurements of MCLEDs were performed in Institute for Integrative Nanosciences IFW in Dresden. The sample was excited by 635 nm picosecond pulses generated by a PicoQuant, LDH-P-C-635B laser head controlled by a PDL-800B driver or by a HeNe laser with emission wavelength of 632 nm through a 20x microscope objective (NA = 0.4) with spot diameter of ca. 9μm. The emitted light is then collected by the same microscope objective and dispersed by a 500 mm monochromator equipped with an InGaAs-CCD detector. The electroluminescence measurements were done at the same experimental setup. A constant DC current of 50 mA was applied to the diodes. All measurements were performed at room temperature.

UniMCO simulation software

UniMCO is a software package for the design and analysis of light-emitting diodes (LED), organic LED (OLED), semiconductor resonant-cavity LED (RCLED) devices, VCSEL laser, solar cell devices, and thin-film optical coatings with arbitrary multilayer structures, i.e., the devices can consist of any number of layers of any thickness, and of any material. UniMCO provides an extensive database of optical constants for over 250 materials, from the commonly used materials in LED, OLED, RCLED and VCSEL to intricate models that incorporate the effects of temperature and composition variations. It is also possible for users to input their own optical properties into the database through table or ASCII data file. UniMCO is especially powerful for modeling of microcavity-based OLED and RCLED devices [107]. The UniMCO graphical user interface allows users to quickly define the multilayer structure using either the default structure library or layout tool with five built-in-blocks, including substrate, distributed Bragg reflector (DBR), spacer, emitter, and metal blocks. A general multilayer device structure can consist of any number of DBR and spacer blocks, while each DBR block can consist of any number of alternative layers of quarter-wave stacks, and each spacer can have any number of layers of any thickness, and of any materials.

The accuracy of the light output simulation depends on how well the intrinsic luminescence of the material (EL0) is known. UniMCO requires the bare EL0 as input, namely the EL0 should come from the emitting dipoles in a space filled with the emitting medium without any interfaces. For OLED devices, the device dimension is comparable to wavelength, resulting in a strong modification to the bare EL0 spectrum due to the interface effect (or weak microcavity effect). In order to obtain the true (bare) EL0 for the simulation, one has to remove the interface effect from experimental spectrum of a test structure. UniMCO implemented a powerful EL0 extraction module, which can automatically extract the true EL0 by removing this interface effect from experimental data.

The UniMCO's optimization module allows users to optimize their device designs. The thickness variation and the location of the emission zone can have a significant effect on the device performance. Starting from an arbitrary device structure, the UniMCO optimizes the structure automatically and gives the best layer thickness and location of the emission zone. UniMCO's optimization module can be used not only for microcavity-based devices, but also for the standard non-cavity devices.

UniMCO enables to design, specify, optimize, simulate, and create solutions for LED, OLED, RCLED, VCSEL, and optical thin film coatings within a single framework. Output results can be analyzed and plotted to assist users in completing the design process. The versatile UniMCO software package is independent on the detailed device structures.The interactive visualization tool allows users to view, analyze and print 1D 'slices' through multi-dimensional optical functions; with this visualization tool, it is possible to vary a given parameter and see the resulting effect on the optical functions in real time. The optical field, reflectivity, transmittance, phase shift, absorption, and light output can be viewed as either surface or contour plots with various color maps.

Chapter 4

Experiments, results and discussion

In the first experiments the properties, homogenity, the thickness variation over the wafer and the deposition rates of single Si and SiO_2 layers, produced by magnetron sputter deposition, have been investigated. The goal was to find optimal deposition parameters, which allows the fabrication of high quality multilayered stacks based on Si and SiO_2 , forming a distributed Bragg reflectors (DBR).

The next part describes the investigation of the first microcavity enhanced silicon light emitting pn-diodes. In this case, the microcavity, also called resonant cavity, is formed by placing the emitting layer between the optical resonator, consisting of a metallic $CoSi_2$ mirror at the bottom and the top distributed Bragg reflector based on 2.5 pairs of SiO_2 /Si.

In the last part of this chapter the process development and the properties of the pn-diodes, produced in very thin silicon membranes are described. In order to get the microcavity LED, in the final fabrication step, the Bragg reflectors were deposited on the top and at the bottom of this thin membranes containing the light emitting Si pn-diodes.

4.1 Used substrates

In the experimental part of this work two different types of substrates were used. The Czochralski silicon wafers were delivered by Silchem Handelsgesellschaft mbH. The silicon on insulator (SOI) wafers were produced by IceMOS Technologies Ltd.

4.1.1 Silicon substrates

In the first experiments, focused on the investigation of single and multilayers of sputter deposited Si and SiO_2 , the silicon substrates with the diameter of 3" and 4" (76.2 mm and 100 mm) have been used. The properties, dimensions and characteristics of Czochralski silicon wafers according to their specifications are summarised in the Tab. 4.1.

Czochralski process

High-purity, semiconductor-grade silicon (only a few parts per million of impurities) is melted down in a crucible, which is usually made of quartz. Dopant impurity atoms such as boron or phosphorus can be added to the molten intrinsic silicon in precise amounts in order to dope the silicon, thus changing it into n-type or p-type extrinsic silicon, in order to influence its electrical conductivity. A seed crystal, mounted on a rod, is dipped

Si wafer specification		
Diameter [mm]	76.2	100
Type	N/Phos	N/Phos
Orientation	⟨100⟩	⟨100⟩
Resistivity [Ωcm]	1–10	1–5
Thickness [μm]	381±25	525±25
Total thickness variation (TTV) [μm]	<5	<5
Finish	single side polished	single side polished
Particles	<10 @ 0.5 μm	<10 @ 0.3 μm
Surface roughness [nm]	0.6±0.1	0.7±0.1

Table 4.1: Specifications of silicon wafers

into the molten silicon. The seed crystal's rod is pulled upwards and rotated at the same time. By precisely controlling the temperature gradients, rate of pulling and speed of rotation, it is possible to extract a large, single-crystal, cylindrical ingot from the melt. Occurrence of unwanted instabilities in the melt can be avoided by investigating and visualizing the temperature and velocity fields during the crystal growth process. This process is normally performed in an inert gas atmosphere, such as argon, and in an inert high purity chamber, such as quartz.

4.1.2 Silicon-On-Insulator (SOI) substrates

In order to fabricate an effective resonator needed for Si based microcavity enhanced LED, it is necessary to control the thickness of the emitting layer and the multilayered Bragg reflectors. The Si LEDs were fabricated by standard Si planar technology on SOI substrates with defined thickness of the top Si device layer.

Silicon-On-Insulator (SOI) is a major technology breakthrough for manufacturing faster chips that consume less power. SOI has brought rapid advancements in Analog, RF, Low power and Low voltage applications. A cost effective way to fabricate these engineered wafers has been explored for decades. Two mostly used ways of manufacturing SOI wafers are the SIMOX (**S**eparation by **Im**plantation **Ox**ygen) (Fig. 4.1a) and Smart Cut^{TM} methods (Fig. 4.1b). SOI substrates produced by both methods were tested. Because the SOI wafers made by Smart Cut^{TM} technology possess less defects in the top Si device layer, we have decided to use these for Si-MCLED fabrication.

Smart Cut^{TM}

The Smart Cut^{TM} process is based on the principles of ion implantation and wafer bonding [139–141]. This process requires two starting silicon wafers to produce a single SOI wafer. The technique starts with oxidation of a silicon wafer (wafer A). The oxide formed will become the buried oxide (BOX) in the final SOI wafer. Ion implantation of protons (hydrogen ions) through the formed oxide into the underlying silicon forms a layer of small hydrogen bubbles. Now, this wafer A is bonded to another clean silicon wafer (wafer B). The wafer B will be the substrate (handle wafer) of the final SOI wafer. The bonded wafer pair is now heated so that the wafers cut along the hydrogen implanted bubble layer. The removed portion of the silicon wafer will now become the substrate

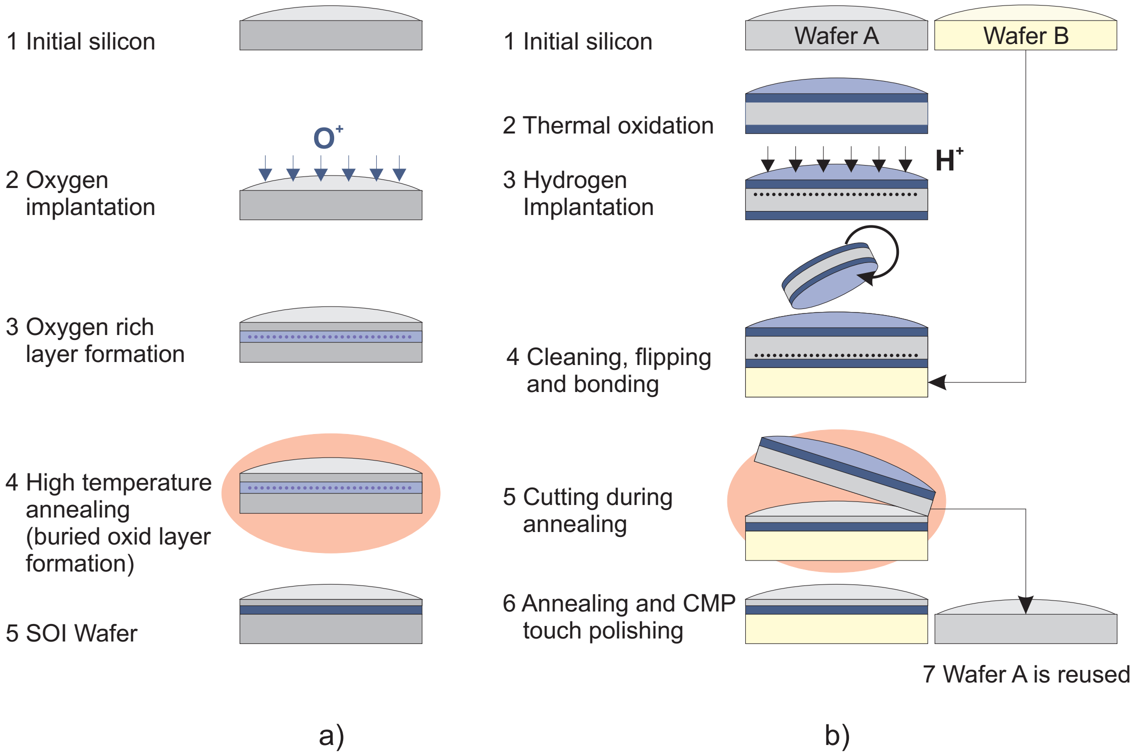

Figure 4.1: Process of SOI wafer fabrication by a) SIMOX technology: the oxygen implantation (2), formation of an buried oxygen rich (supersaturated) Si layer (3), high temperature annealing (4) and formation of the buried SiO_2 layer by phase separation and annealing of implantation damage in the top device layer. b) Smart Cut^{TM}: hydrogen implantation of wafer A that has been oxidized (2-3), flipping and bonding of wafer A together with wafer B (4), wafer cutting during annealing along the bubble layer (5), final SOI wafer after annealing and chemical mechanical touch polishing (CMP), wafer A is used again as substrate for another SOI fabrication procedure (6).

SOI wafer specification			
	Handle layer	Buried oxide	Device layer
Diameter [mm]	100	100	100
Growth/Type	CZ	Thermal	CZ
Type	N/Antimony		N/Phos
Orientation	$\langle 100 \rangle$		$\langle 100 \rangle$
Resistivity [Ωcm]	1–20		1–5
Thickness [μm]	400 ± 5	0.2 ± 0.01	2 ± 0.5
TTV[1] [μm]	<2	<0.002	<1
Finish	back side polished		polished

Table 4.2: Specifications of SOI wafers

for another smart cut wafer. The SOI wafer is now annealed, polished and prepared for further CMOS processing steps (Fig. 4.1b).

4.2 Fabrication and characterization of distributed Bragg reflectors

The goal of this work is to improve the properties of the silicon LED by a resonant microcavity. The optical resonator, designed for the resonant wavelength 1150 nm, is formed by a high reflectivity mirror at the bottom of the active layer (Si diode) and a semitransparent mirror at the top. In order to create an effective optical resonator, good candidates for the top and the bottom mirrors are distributed Bragg reflectors (DBRs).

A DBR is a periodic grating that can be formed on a wafer from alternating layers of differing index of refraction. The thickness of each optical layer corresponds to one quarter of the wavelength for which the mirror is designed. The advantage is that a DBR consisting of layers of semiconductor and dielectric material, Si and SiO_2 , can be formed using the well established semiconductor fabrication technique of magnetron sputter deposition. The theory of the DBR was described in detail in Sec. 2.4.1.

In this section the properties of single SiO_2 and Si layers and finally of the multilayered stack of SiO_2 /Si forming the DBR in dependence on deposition parameters are investigated.

4.2.1 Deposition and characterization of SiO_2

Deposition parameters

The technology of RF sputtering from a fused silica target is well known since 1966 [142]. It has been shown [143], that deposition of SiO_2 films from a fused silica target in Ar/O_2 gas mixtures can lead to high quality oxides. A very important role is played by the process parameters, that have a big influence on the properties of sputtered oxides. A detailed investigation of the sputter process under different sputter conditions and the characterisation of deposited films (deposition rates as a function of atmosphere, temperature and power applied to SiO_2 target) are reported in [144, 145, 143].

---

[1] Total thickness variation

In this work the SiO_2 films are used as a part of distributed Bragg reflectors and as insulating layers. For SiO_2 deposition we used an 8 inch (200 mm) pore-free glassy SiO_2 targets of 5N purity at a chamber base pressure in the order of 10^{-5} Pa. It is important that the surfaces of all components inside the chamber are free of metallic particles, since metal contamination by re-sputtering would degrade the oxide quality.

The process of deposition was realised in a mixture of argon/oxygen with a mass flow ratio of 3:20 (6 sccm O_2, 40 sccm Ar), which helps to compensate the oxygen deficiency in SiO_2 films sputtered in pure argon [146] and greatly reduces the density of oxide defects and interface states. Too high oxygen concentrations (over 40%) would lead to increased electron trapping [147]. Substoichiometry causes a variety of oxide defects such as the neutral oxygen vacancy centers and the related charged paramagnetic E' centers, which manifest themselves in an increased etch rate in buffered hydrofluoric acid (BHF) and in poor electrical oxide quality.

Low total pressure during the sputtering process (0.66 Pa) and a small distance between substrate and target decrease the probability of collisions between gas atoms and sputtered particles. During the sputter deposition the substrate-target distance was set to 55 mm. Jelenkovic [147] has shown, that a short distance between substrate and target leads to very smooth and dense films under compressive stress. This is due to small loss of kinetic energy of the sputtered particles, which results in a higher surface mobility.

The sputter rate of SiO_2 is influenced by the flux, energy, mass and angle of Ar ions incident on the silica target. The silica target has a low thermal conductivity. High fluxes and energies result in a increased target temperature. The target then acts as a source of substrate heating. Due to the small distance between target and substrate (55 mm) and relative long deposition times, the substrate reaches temperatures of about 50°C. At the same time the higher kinetic energy of sputtered particles and reflected neutralized Ar atoms increases the re-sputtering from the substrate and enhances the substrate surface mobility. Both effects yield a more dense film structure. On the other hand the sample bombardment with highly energetic particles increases the density of interface states [147].

The use of substrate heating or a low negative substrate bias results in further lowering of the defect density and the concentration of incorporated argon ions. On the other hand temperatures above 300°C lead to an increase of the stress. This effect is completely accounted to the difference in thermal expansion coefficients of the substrate and the film. But even high deposition temperatures (350°C - 500°C) are too low to anneal radiation induced atomic defects in the oxide. Therefore, if a high electrical quality is required, high temperature post-deposition annealing (1000°C - 1100°C) is necessary. A similar situation occurs by using a negative substrate bias above 80 V, which leads to an increase of the stress due to atomic displacement of the film by incident Ar ions. The experiments were performed by varying the substrate power, using 0 W, 100 W and 250 W, which corresponds to a negative substrate bias of 0 V, 60 V and 120 V respectively.

Deposition rate and thickness distribution

In the first experiment the *deposition rate* (Fig. 4.2a) was investigated by varying the target RF power in the range between 250 W and 1000 W. The SiO_2 films were deposited on a set of two inch wafers. The sputter condition, offering a good quality of SiO_2 films, were chosen from the literature [143, 142, 144–147]: gas flow: 40 sccm Ar, 6 sccm O_2, total pressure 0.66 Pa and target-substrate distance 55 mm. The deposition rate of SiO_2 increases linearly with the target power. The thickness was measured by VASE in the central region of wafers.

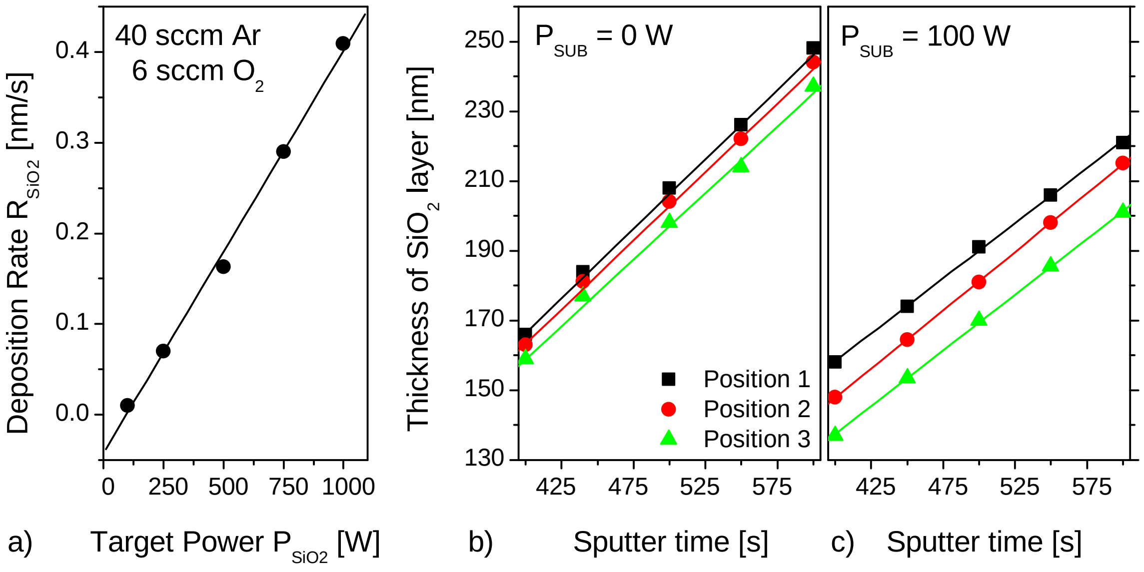

Figure 4.2: a) Deposition rate of SiO_2 films sputtered from a fused silica target as a function of target RF power (40 sccm Ar, 6 sccm O_2, 0.66 Pa, d = 55 mm). Thickness of SiO_2 films as a function of sputter time at P_{RF} = 1000 W using a substrate power of 0 W (b) and 100 W (c). The positions 1 (black dots), 2 (red dots) and 3 (green dots), indicated in Fig.4.3, correspond to central area of the 3 inch wafer, 15 mm from the centre and 30 mm from the centre (at the wafer edge), respectively. The dots are the measured values and the lines correspond to linear fits.

In further experiments, the influence of substrate RF bias on the deposition rate and the film thickness distribution across the 3 inch n-Si < 100 > wafer were investigated. The same sputter parameters were used as before. The target power was set to 1000 W. The variable parameters were the deposition time and the substrate RF power (0 W, 100 W and 250 W).The thickness was determined by X-ray-reflectometry (XRR), VASE, TEM and surface profiling (DEKTAK profilometer).

Fig. 4.2b and 4.2c show the SiO_2 films thickness as a function of sputter time (deposition rate) using the substrate power of 0 W and 100 W, respectively. This corresponds to a substrate bias 0 V and 60 V at 0.66 Pa, respectively. The set of samples were prepared by magnetron sputtering at different sputter times between 400 s and 600 s. One can see that the deposition rate decreases with applied substrate bias, due to the known fact, that Ar ions bombard the surface of the substrate with higher energy causing a higher sputter rate of atoms from the growing SiO_2 film.

The next aim was to look at the *thickness distribution* of the deposited films across the wafer. The results are shown in Fig. 4.3. The films were deposited on 3 inch wafers with the same sputter parameters for 490 s. The thickness of the films was measured by VASE. It obvious that with increasing substrate bias not only the deposition rate decreases, but also the thickness variation increases, always with the maximum in the centre of the wafer. The reason for this behavior is the local charging of the non-conductive target, that causes the distortion of the electrical potential at its surface. In this case the highest erosion is not located in one ring between two magnet rings in the drift path $E \times B$ (Fig. 3.3b) as in the case of conductive targets, but two erosion rings at the SiO_2 target appear. This has been observed by Seifarth [148].

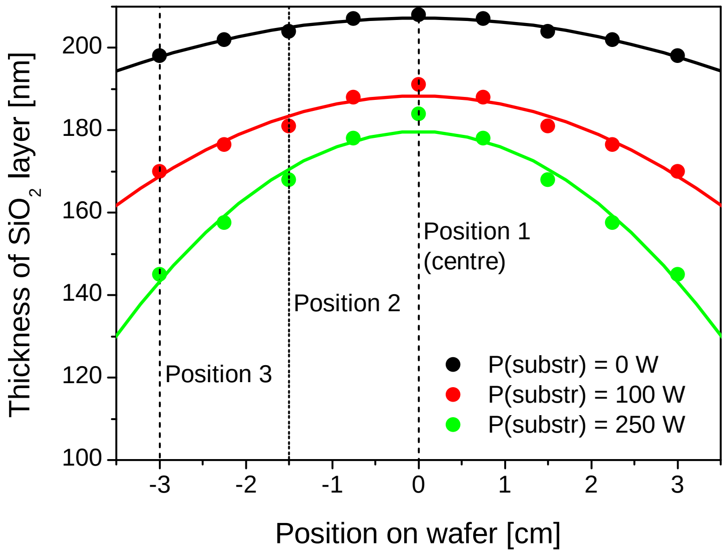

Figure 4.3: Thickness distribution of SiO_2 films, sputtered 490 s (40 sccm Ar, 6 sccm O_2, P_{RF} = 1000 W, 0.66 Pa, d = 55 mm) over 3 inch (75 mm) Si $< 100 >$ wafer, applying substrate power of 0 W (black dots), 100 W (red dots) and 250 W (green dots). The lines are polynomial fits to the measured data.

Properties of deposited SiO_2 films

The deposited SiO_2 films (target power P_{RF} = 1000 W, substrate power P_{SUB} = 0 W) are quite smooth (see Fig. 4.4). AFM scans along the diagonal of a 2000 nm wide area showed peak-to-valley *roughnesses* of 2.35 nm for the 150 nm thick film and 3.83 nm for 300 nm layer.

In another experiment, the influence of the substrate RF bias on the *optical constants* of SiO_2 films deposited on silicon substrates was investigated. The deposition conditions were as before (40 sccm Ar, 6 sccm O_2, P_{RF} = 1000 W, 0.66 Pa, d = 55 mm, P_{SUB} = 0 W/100 W/250 W). The optical constants were determined by spectroscopic ellipsometry in the visible range using Sellmeier's model (see A.1.4), and assuming that the extinction

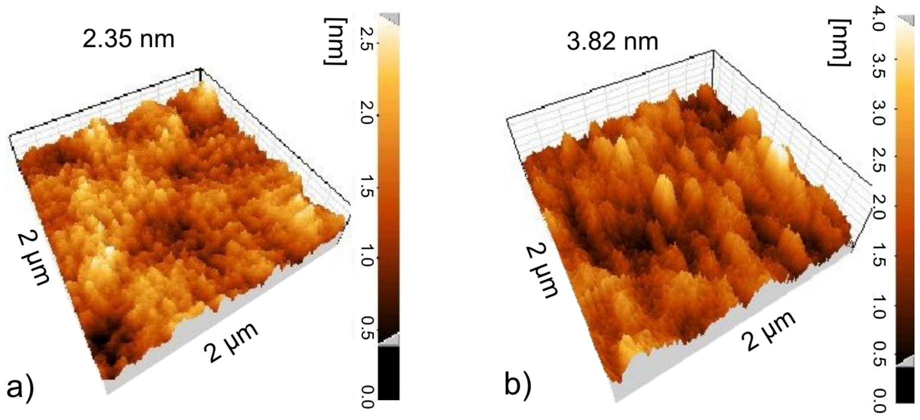

Figure 4.4: AFM image of a) 150 nm and b) 300 nm thick SiO_2 layers. The peak-to-valley values are 2.35 and 3.82 nm, respectively.

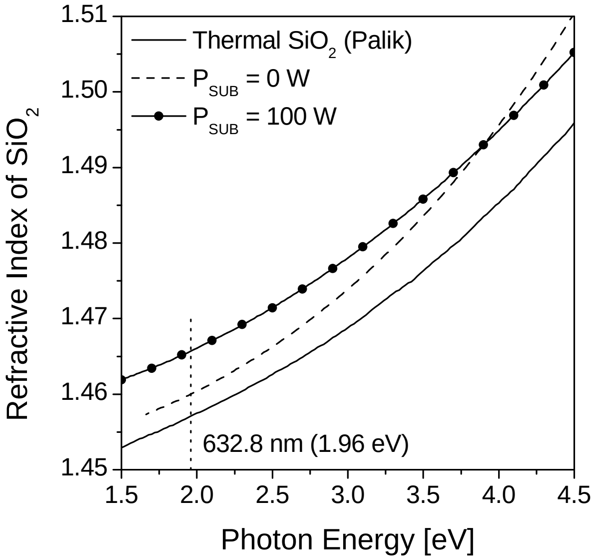

Figure 4.5: Refractive index of oxide films deposited from a silica target in Ar/O_2 atmosphere without using a substrate bias (dashed line), with applied substrate bias of P_{SUB} = 100 W (circle symbols), compared to refractive index of thermal oxide [95] (solid line).

coefficient $k \approx 0$. The refractive index of deposited SiO_2 films at the wavelength 632.8 nm (1.46) is generally higher than the one of thermal oxide (1.457 [95]). The use of an RF substrate bias of 100 W and 250 W even increases the refractive index up to 1.466 and 1.468 (Fig. 4.5b) at $\lambda = 632.8$ nm, respectively. Post deposition high temperature annealing (30 min, 1000°C, N_2) leads to relaxation of the SiO_2 network structure, which causes a decrease of the refractive index close to the value of thermal oxide.

The increased refractive index values of sputtered SiO_2 films have been attributed to an increased *density* resulting from the plasma particle bombardment of the growing film. A dependence, based on the Lorentz-Lorenz relation, between the refractive index n and the density ρ at 632.8 nm of plastically densified amorphous SiO_2 and their crystalline phases [149, 150] has been found:

$$n = 1.029 + (0.195 \pm 0.021)\,\rho \qquad (4.1)$$

This formula is relevant only for thermally grown oxides and SiO_2 films deposited in Ar atmosphere with addition of O_2. The reason is that the films deposited from a fused silica target in pure Ar are slightly oxygen-deficient and have therefore higher refractive index, what is not attributed to a higher compaction. According to equation 4.1 the density of the thermal SiO_2 [95] is $\rho = 2.195\ g/cm^3$. Sputter deposited SiO_2 films (with $n = 1.46$) have a density of $\rho = 2.21\ g/cm^3$. This value increases to $\rho = 2.241\ g/cm^3$ for the films deposited using a substrate bias of 100 W ($n = 1.466$). Lisovskii has published results of IR spectroscopic investigation of various SiO_2 films and has experimentally proved the hypothesis concerning the higher density of sputter-deposited SiO_2 films [151, 152].

Photoluminescence (PL) measurements

For PL phenomena, two important processes are the formation of photo-excited carriers (excitation process) and the radiative recombination of the photo-excited carriers

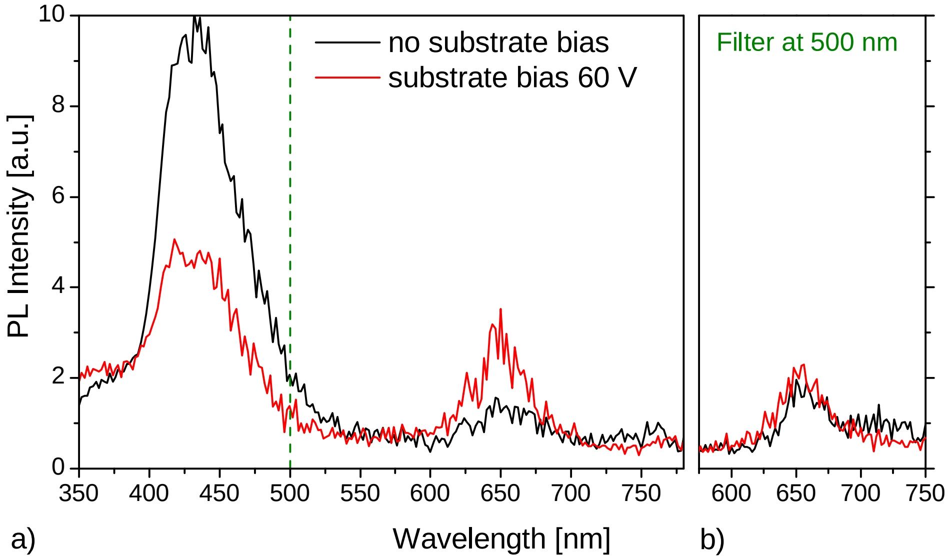

Figure 4.6: Photoluminescence spectrum of a 200 nm SiO_2 film sputtered by using standard parameters (black line) and by applying 100 W substrate power (red line). The excitation wavelength is 325 nm. a) The peak at 430 nm is related to oxygen deficiency center (ODC). By using a substrate power of 100 W, this defect type was reduced by about 50 %. b) Spectrum measured after applying a glass filter at 500 nm. The peak at 650 nm belongs to non-bridging oxide hole centers. This defect did not change.

through PL centers, in this case the defects in a-SiO_2 (luminescence process). For the photoluminescence experiments a laser with a wavelength of 325 nm was used for excitation. The photoluminescence spectrum obtained shows two distinct peaks (Fig. 4.6). The peak at 650 nm (1.9 eV), called also the red luminescence R, is due to an oxygen-excess defect that forms a non-bridging oxygen hole center (NBOHC) [153–155]. The peak at 430 nm (2.9 eV) is attributed to the singlet luminescence of two-fold-coordinated silicon (divalent) centers associated with an oxygen deficiency center (ODC) [156, 157].

4.2.2 Deposition of Si

Layers of amorphous silicon (a-Si) were deposited on a silicon substrate covered with 200 nm SiO_2 in Ar atmosphere at a total pressure 0.66 Pa. The DC target power was set to 250 W. The distance between substrate and target was constant 55 nm. The deposition rates (thickness vs. time) for DC magnetron sputtering of Si with substrate power 0 W and 100 W, determined from XRD, VASE, DEKTAK and TEM measurements are shown in Fig. 4.7. The deposition rate in this case is higher for the films, where an additional substrate bias has been applied.

Characterisation of deposited Si films

Fig. 4.8 shows the distribution of the thickness over the 3 inch wafer. The layers were deposited for 203 s on 200 nm thick thermal oxide film using the same parameters as before (50 sccm Ar, 0.66 Pa, d = 55 mm, P_{DC} = 250W). The only variable parameter was the substrate power P_{SUB} = 0 W/100 W/250 W. The situation here is different from that one for the sputtered SiO_2 films. In the case of DC sputtering there is a equipotential

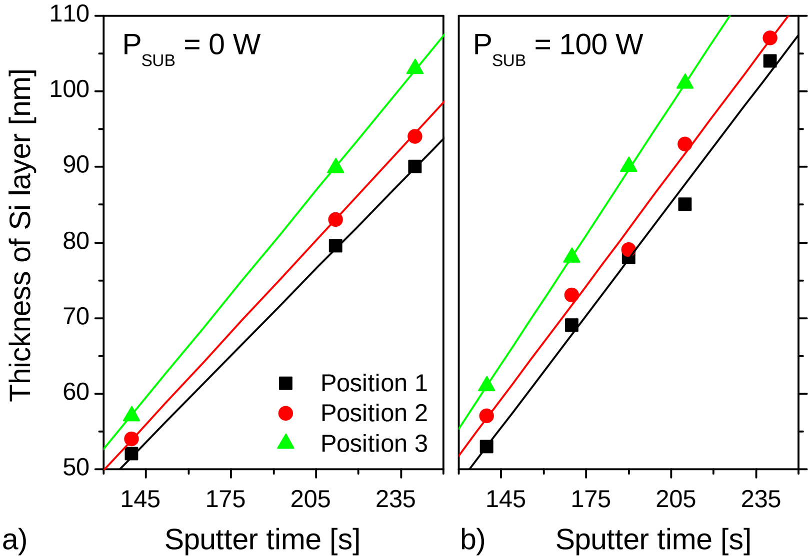

Figure 4.7: Thickness of Si films as a function of sputter time for DC mode sputtering from a Si target (50 sccm Ar, 0.66 Pa, d = 55 mm) at P_{DC} = 250 W using a substrate power of 0 W (a) and 100 W (b). The positions 1 (black dots), 2 (red dots) and 3 (green dots) are indicated in Fig.4.8. They correspond to central area of the 3 inch wafer, 15 mm from the centre and 30 mm from the centre (at the wafer edge), respectively. The dots are the measured values and the lines correspond to linear fits.

plane on the surface of the conductive target. The maximal erosion rate is in the $E \times B$ drift loop (fig. 3.3). Visual check of the 8 inch Si target showed an erosion groove with 50 mm diameter, situated in the middle of the target. The deposition rate has a maximum below this ring and a minimum in the centre.

The density of silicon single crystals (c-Si) has been accurately measured by researchers from US National Bureau of Standards (NBS), for the purpose of obtaining a solid density standard to replace water, which is the commonly adopted density standard. The density is given to be 2.329 g/cm^3. In the case of polysilicon, the density is a function of the grain size, but it does not radically differ from c-Si. The density of poly-Si is 2.3–2.33 g/cm^3. The densities of a-Si films are generally lower than the density of crystalline silicon. Depending on deposition techniques and parameters (rate, pressure, substrate temperature, atc.), the density can vary from 1.71 to 2.2 g/cm^3 [158]. Using some special deposition methods like xenon ion beam assisted deposition [159], is it possible to obtain very dense a-Si films with 2.38 g/cm^3. Furthermore, silicon, like water, has a liquid phase density (2.52 g/cm^3) greater than its solid phase density [160]. The density of a-Si films fabricated by sputter deposition, where no substrate bias has been applied is 2.35 g/cm^3. Layers of a-Si deposited with using a substrate power of 100 W increases to a value of 2.48 g/cm^3.

Next the evolution of the surface roughness of the sputtered a-Si film with increasing thickness was investigated. The roughness of films deposited at different times on 200 nm thermal oxide is shown in fig. 4.9. The peak-to-valley roughness value for a 40 nm thin film is 1.95 nm. A silicon layer with a thickness of 120 nm has a roughness of 2.94 nm.

The optical constants are different for silicon with crystalline and amorphous structure [95]. The optical properties of a-Si are sensitive to preparation conditions and to

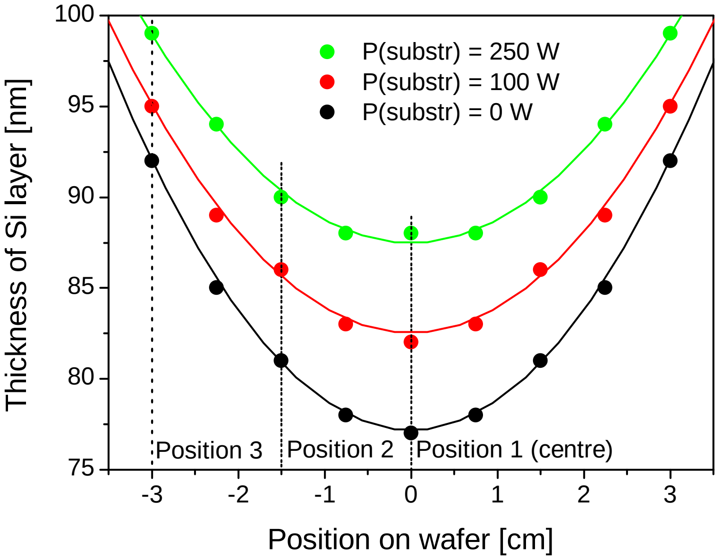

Figure 4.8: Thickness distribution of Si films, sputtered 203 s (50 sccm Ar, P_{DC} = 250 W, 0.66 Pa, d = 55 mm) over 3 inch (75 mm) Si < 100 > wafer, applying substrate power of 0 W (black dots), 100 W (red dots) and 250 W (green dots). The lines are there to guide the eye.

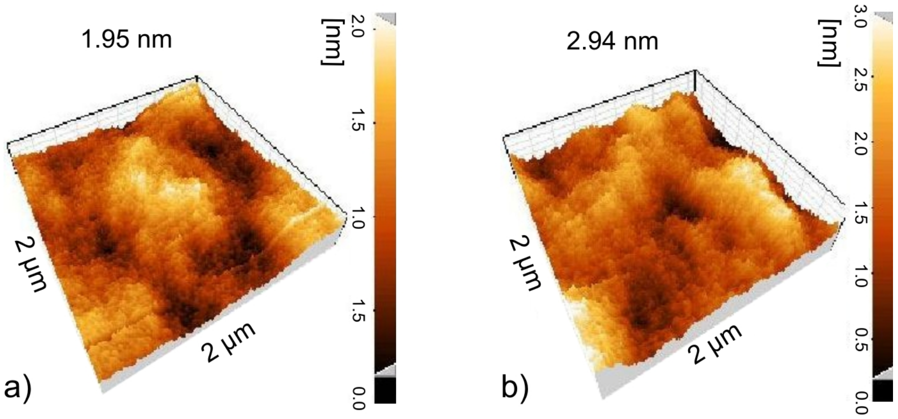

Figure 4.9: AFM images of the surface roughness of sputtered a-Si layers with various thickness: a) 40 nm , roughess 1.95 nm, b) 120 nm, roughness is about 2.94 nm. The a-Si layers are sputtered on the top of 200 nm thermally grown SiO_2 on Si substrate.

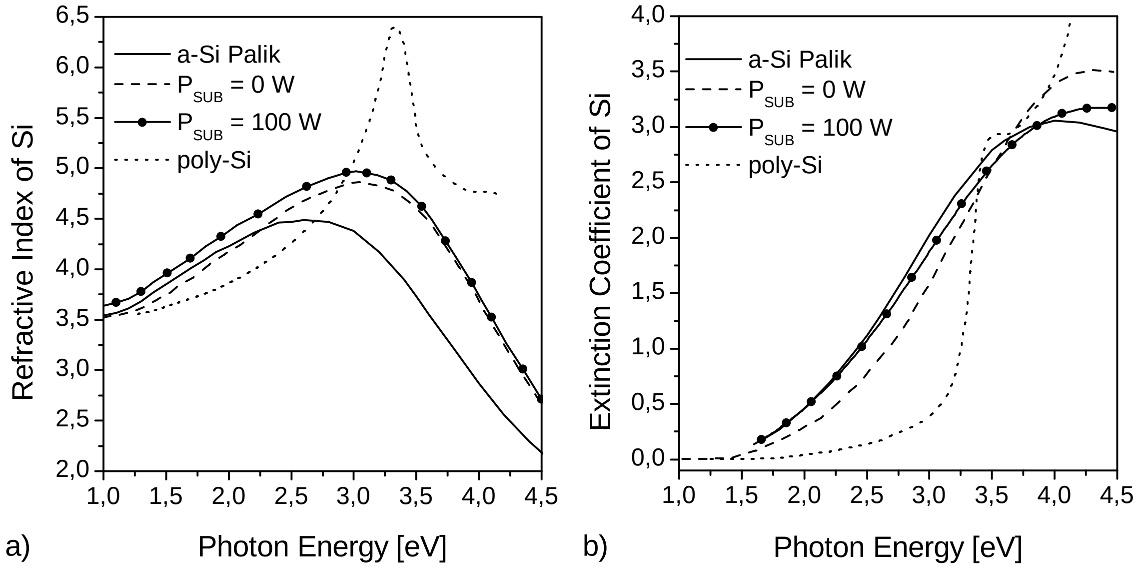

Figure 4.10: a) Index of refraction and b) extinction coefficient of dc-sputtered a-Si with P_{SUB} = 0 W (dashed line), P_{SUB} = 100 W (circle symbols). The solid and the dotted lines correspond to reference data for evaporated a-Si and poly-Si, respectively, taken from [95].

doping with hydrogen. The optical measurements are also strongly affected by surface conditions and oxide films on the Si-surface, substrate temperature, deposition rate and method, impurities, annealing, environment, etc. Variable spectroscopic ellipsometry (VASE) has been used to routinely characterize sputtred amorphous silicon films. Since VASE measurements do not yield quantities of interest directly, the VASE data must firstty be fitted to a model to obtain useful parameters such as film thickness and optical functions. The Tauc-Lorentz (TL) model for the optical functions of amorphous materials [161, 162] has been shown to be very useful in interpreting the measerement results. A four-parameter model (amplitude A, energy E_0, broadening of the main optical transition C and the band gap energy E_g) is usually sufficient to describe the optical functions of the thin a-Si films (see A.1). Extracted optical constants for a-Si deposited with P_{SUB} = 0 W and 100 W are plotted in Fig. 4.10.

4.2.3 Distributed Bragg Reflectors (DBR)

As shown in the literature [1, 89], silicon pn-diodes emit light with the maximum at the wavelength of 1150 nm. The band gap energy of crystalline silicon is $E_g = 1.12eV$, what corresponds to 1100 nm, which means that the light emission mechanisms is band-to-band transition. A challenge is the provision of electrical and optical confinement for enhancing of the diode efficiency and performance. For this purpose distributed Bragg reflectors, forming a resonator, can be used. Distributed Bragg reflectors comprise alternating layers of two materials transparent to this emission wavelength and having different refractive indices: the larger the difference in refractive index between the two materials, the smaller is the number of alternating layers required to achieve a high reflectivity (see section 2.4.1).

	Parameters	Sample A	Sample B	Sample C	Sample D
	Substrate	n-Si	n-Si	n-Si	n-Si
	Wafer diameter	3”	3”	4”	4”
	Target-substrate distance [mm]	55	55	55	55
	Total pressure [Pa]	0.66	0.66	0.66	0.66
SiO_2	Atmosphere Ar/O_2 [sccm]	40 / 6	40 / 6	40 / 6	40 / 6
	Target RF power [W]	1000	1000	1000	1000
	Substrate power [W]	0	100	0	0
	Sputter time [s]	490	490	490	490
Si	Atmosphere Ar [sccm]	50	50	50	50
	Target DC power [W]	250	250	250	250
	Substrate power [W]	0	100	100	100
	Sputter time [s]	213	213	183	183
	Annealing	–	–	–	1050°C 20 min, N_2

Table 4.3: Deposition parameters of samples A, B, C and D

Fabrication

A multilayered system based on Si/SiO_2 is a good solution for fabrication of distributed Bragg reflectors. Both of the materials can be manufactured with a good quality by magnetron sputtering, as shown above. At the emission wavelength of 1150 nm the refractive indices of Si and SiO_2 are 3.575 and 1.46, respectively (Fig. 4.10 and 4.5). According to the definition the thickness of layers in the Bragg reflector stack must be a quarter of the emission wavelength. In this case, there is a need to fabricate a stack comprising alternating layers of 80 nm Si and 200 nm SiO_2 . There are 4 samples analysed in this chapter: A, B, C and D. A summary of deposition conditions can be found in Table 4.5.

TEM

The TEM images in Fig. 4.11 compare the microstructure of samples A, B and D. Layers of amorphous silicon deposited with standard parameters (see sample A in Tab. 4.3) in Fig. 4.11a have visible fibrous structure perpendicular to the substrate surface. This comes from an inhomogeneous density distribution of the silicon atoms. The SiO_2 /Si interface roughness is in the range of 2-3 nm. Fig. 4.11b shows the cross section TEM images of the Bragg reflector stack fabricated with a substrate power of 100 W. No change in the structure of SiO_2 layers is visible. Nevertheless, the applied substrate bias helps to obtain homogeneous and very dense amorphous silicon layers. The interface roughness here is below 1 nm. High temperature annealing causes crystallisation of the amorphous silicon (Fig. 4.11c), which is accompanied by a change of density and thickness of the poly-silicon layers. The crystallisation of the a-Si layers leads again to an increase of the interface roughness between Si and SiO_2 . The thicknesses of all layers for samples A-D obtained from TEM images are summarised in Tab. 4.4.

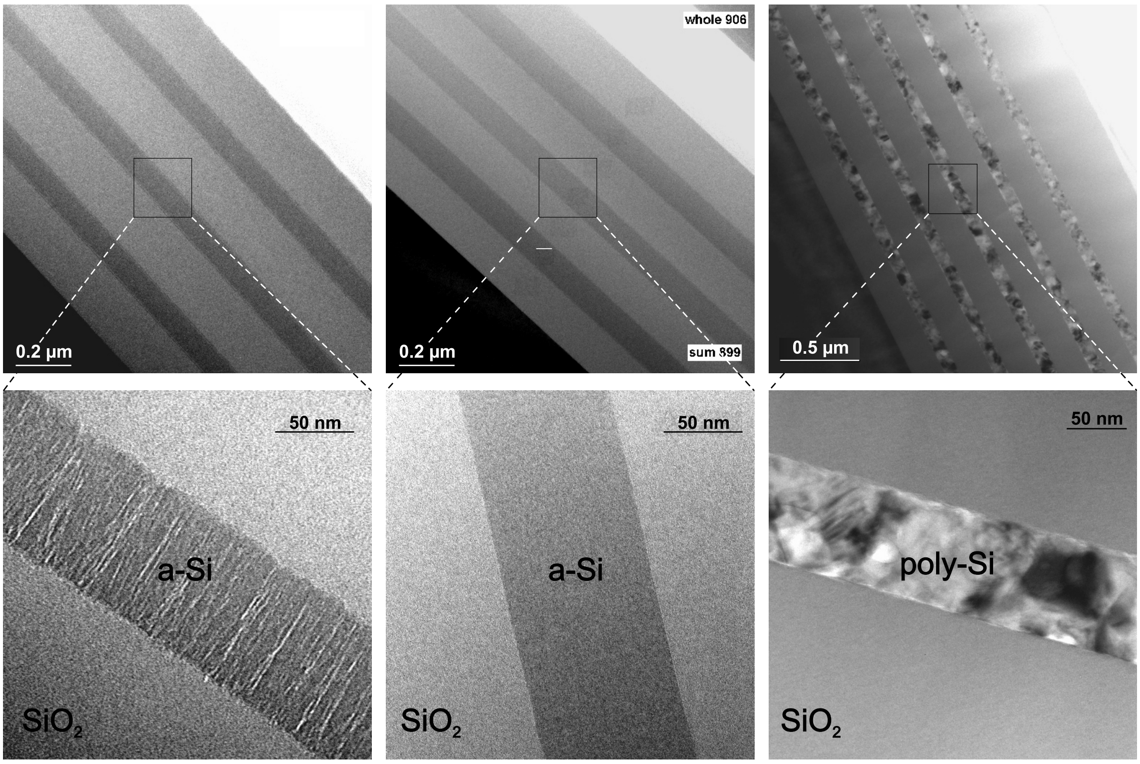

a) Sample A b) Sample B c) Sample D

Figure 4.11: TEM bright-field images of Bragg stacks deposited at a) standard conditions (see sample A in Tab. 4.5), b) using a substrate power 100 W - sample B and c) an image of an annealed stack - sample D (20 min, at 1050°C in N_2)

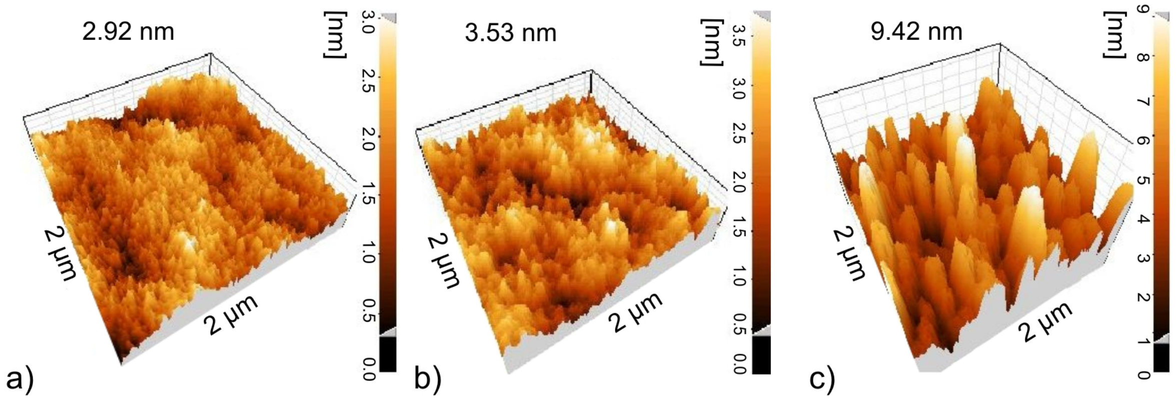

Figure 4.12: AFM image of the surface of a) 80 nm a-Si sputtered on 200 nm thermal SiO_2 with a roughness of 2.92 nm, b) 200 nm SiO_2 (deposited on a bare silicon wafer) with a roughness of about 3.53 nm, c) distributed Bragg reflector consisting of 3.5 pairs of 200 nm SiO_2 and 80 nm Si (sample A), where the roughness is increased to 9.42 nm.

Surface roughness

The roughness (peak-to-peak value) of multilayer stacks based on SiO_2 /Si increases with the number of alternating layers. Fig. 4.12 shows that 3.5 pairs of SiO_2 /Si layer deposited by standard conditions (sample A) reach a surface roughness of 9.42 nm. The same stack deposited with substrate bias of 100 V has surface roughness only of about 2 nm (sample B).

Characterisation of DBRs with VASE

Bragg stacks were first analysed by VASE (see Tab. 4.4). But since the used spectroscopic ellipsometer works in the visible spectral range, the maximal depth that can be investigated, is about 1000 nm. For this reason only the top four layers could be determined by VASE. Nevertheless the optical constants of oxide and amorphous silicon deposited with and without substrate bias, obtained from previous investigations (Sec. 4.2.1 and 4.2.2), have been used as input parameters for reflectivity calculations. This program calculates the reflectance spectra and determines the microscopic and macroscopic quantities (thickness, etc.).

Reflectance measurements

Reflectance measurements have been performed by a Fourier transform infrared spectrometer (FTIR) Bruker Equinox 55 using a tungsten lamp, a quartz beam splitter and an InGaAs detector for the near infrared wavelength region. The standard spectral resolution of the spectrometer is better than 0.5 cm^{-1} and it was suitable for most measurements. As a reference a silver metal mirror has been used.

Fig. 4.13 shows the reflectance spectra of different SiO_2 /Si stacks. The left graph compares samples A (black curve) and B (red curve) consisting of 3.5 pairs of low-index material (L) SiO_2 and high-index material (H) Si, which is commonly written as $L(3 \times HL)^2$, where the substrate power during the deposition was set to 0 W and 100 W, respectively. The shift between this two spectra is about 65 nm. The first reason is that the deposition rates of Si and SiO_2 are a function of applied substrate bias. With increased substrate bias the deposition rate of SiO_2 decreases (Fig 4.2). In the case of silicon, the deposition rate is higher for the samples sputtered with applying a substrate bias (Fig 4.7). The second reason is the difference between refractive indices of the layers deposited with and without substrate bias (Fig. 4.10). Taking these facts into account and using optical constants obtained from ellipsometric measurements, an accurate determination of the layers thicknesses in the stack was possible. The summary of thicknesses of SiO_2 /Si layers in stacks A and B obtained from TEM, VASE and reflectance measurements can be seen in Tab. 4.4. Since the difference in refractive indices between SiO_2 and Si is relatively large, already 3.5 pairs give a calculated reflectivity of 99.96 %. The measured value of maximal reflectance of sample A is 94.9 % and 96 % for sample B. The difference between calculated and measured reflectivity is probably due to the finite absorption of Si layers, which is neglected in the simulation. The slightly increased reflectivity of the sample B seems to originate from structural properties. Silicon in the Bragg stack fabricated with standard parameters (sample A, see fig. 4.11a) has a columnar structure and the SiO_2 /Si interfaces are relatively rough. The situation is different for sample

---

[2] L - low refractive index material (SiO_2), H - high refractive index material (Si), $L(3 \times HL) = LHLHLHL = 3.5 \times SiO_2/Si$

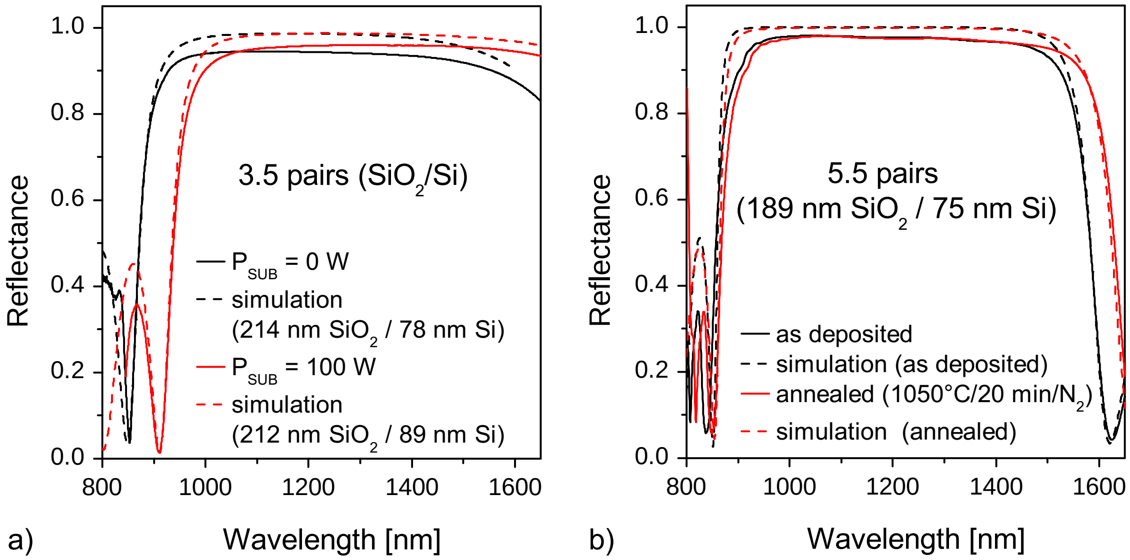

Figure 4.13: Measured (solid lines) and simulated (dashed lines) reflectance spectra of distributed Bragg reflectors consisting of *a)* 3.5 and *b)* 5.5 pairs of SiO_2 /Si. The left graph compares samples A (black line) and B (red line), deposited with P_{SUB} = 0 W and 100 W, respectively. The right figure shows the change of reflectance of sample C (black line) after 20 min annealing at 1050°C in N_2 atmosphere - sample D (red line). The fits obtained from SCOUT simulations using optical constants from VASE measurements (see Fig. 4.5 and 4.10) agree well with measured data. The thicknesses 214 nm SiO_2 / 78 nm Si and 212 nm SiO_2 / 89 nm Si in *a)* and 189 nm SiO_2 / 75 nm Si in *b)* are only average values. For more details see Tab. 4.4 (reflectance).

B, where during the deposition the substrate power was set to 100 W. TEM images (Fig 4.11) show homogeneous amorphous silicon structure having a sharp interface to the neighboring SiO_2 layers.

An increase in the thickness of SiO_2 from layer to layer in DBR stacks of about 1.5% can be observed from the Tab.4.4. This fact has not been further investigated in this work.

Figure 4.13b shows the behavior of a deposited Bragg stack consisting of 5.5 pairs of SiO_2 /Si (sample C) and the same stack after annealing at 1050°C, 20 min in N_2 atmosphere (sample D). The reflectance spectrum of the as-deposited stack is narrower than the spectrum of the annealed sample. Because the refractive index of a-Si is higher than of poly-Si in the near infrared wavelength region, one would expect that the annealing process leads to a shift of the spectra to smaller wavelengths. However, as already mentioned before, the density of silicon decreases of about 8% during the polycrystallisation. The proof is the increased thickness of the silicon layers of about 6 nm. The change in the thickness of the oxide layers is negligible. This fact results of course in a lot of stress at the SiO_2 /Si interfaces. The simulation (dashed lines), using optical constants, obtained from VASE measurements for a-Si (with P_{SUB} = 100 W), poly-Si and SiO_2 , agrees well with the measured data (solid lines). The thicknesses of the SiO_2 /Si layers in the stack C and D obtained from TEM, VASE and reflectance measurements are summarised in the Tab. 4.4. SCOUT reflectivity calculations for the stack based on 5.5

		Sample A Thickness [nm]			Sample B Thickness [nm]		
Layer	Material	TEM	VASE	Reflectance	TEM	VASE	Reflectance
air							
7	SiO_2	221	219	220	215	214	215
6	Si	78	78	77	89	91	90
5	SiO_2	214	210	212	215	213	214
4	Si	79	78	78	87	88	88
3	SiO_2	213	–	212	213	–	212
2	Si	77	–	78	89	–	88
1	SiO_2	210	–	210	206	–	206
Si substrate							
		Sample C Thickness [nm]			Sample D Thickness [nm]		
Layer	Material	TEM	VASE	Reflectance	TEM	VASE	Reflectance
air							
11	SiO_2	400	402	400	406	404	400
10	Si	76	75	75	81	79	80
9	SiO_2	190	191	190	187	189	190
8	Si	74	73	75	82	81	81
7	SiO_2	192	–	190	188	–	190
6	Si	78	–	77	86	–	82
5	SiO_2	191	–	187	187	–	187
4	Si	73	–	76	82	–	82
3	SiO_2	188	–	187	187	–	187
2	Si	77	–	78	84	–	82
1	SiO_2	184	–	184	184	–	184
Si substrate							

Table 4.4: The thicknesses of the SiO_2 /Si layers in the stack A, B, C and D obtained from TEM, VASE and reflectance measurements

Parameters	SiO_2	Si
Target-substrate distance [mm]	55	55
Total pressure [Pa]	0.66	0.66
Atmosphere Ar/O_2 [sccm]	40 / 6	50 / 0
Target power [W]	1000 (RF)	250 (DC)
Substrate power [W]	0	100
Sputter time [s]	490	183

Table 4.5: Summary of deposition parameters.

pairs of SiO_2 /Si, which can also be written as $L(5 \times HL)^3$, give a value of 99.99 %. The measured reflectivity reaches 98 %.

4.2.4 Conclusions

The investigations on sputter deposited single and multilayers based on Si and SiO_2 have shown that the mechanical and optical properties of the deposited material strongly depend on the deposition process parameters. The most critical variable parameter was the substrate bias. The conclusion of characteriastion of the Si and SiO_2 films deposited with and without substrate bias is that biasing of the substrate during the deposition leads to:

- Si - higher density, lower roughness, higher deposition rate and slightly higher refractive index
- SiO_2 - higher density, less defects, lower deposition rate and higher refractive index; but higher thickness variation over the wafer and instability of the deposition process.

In this work are the SiO_2 /Si multilayers used as the distributed Bragg reflectors to form the optical resonators. The deposition parameters of Si and SiO_2 are summarised in the Tab. 4.5.

4.3 Design of Si pn-junction LED

For the fabrication of LED on n-doped Si substrates two different designs were proposed. Their schematic illustrations are summarised in Fig. 4.14.

The p^+-areas in design 1, formed by ion implantation of boron, have a round shape. We decided to design a mask set with three different diode diameters of $d_{1,2,3}$ = 28, 52, 1100 μm. In this case the p^+-area is contacted from the top and the n-contact is situated on the back side of the substrate. Under DC conditions the electron current is perpendicular to the surface. The electron-hole recombination occurs at the pn-junction situated at the bottom of the p^+-area. The implementation of this design for MCLED is rather complicated, because of the problem with the integration of the n-contacts with bottom mirror. This works well only if the bottom mirror is conductive.

From this reason a design 2 was suggested. Differently to the previous design, the n-substrate is contacted from the top (orange phosphorus doped n^+-areas). Under DC

---

[3] L - low refractive index material (SiO_2), H - high refractive index material (Si), $L(5 \times HL) = LHLHLHLHLHL = 5.5 \times SiO_2/Si$

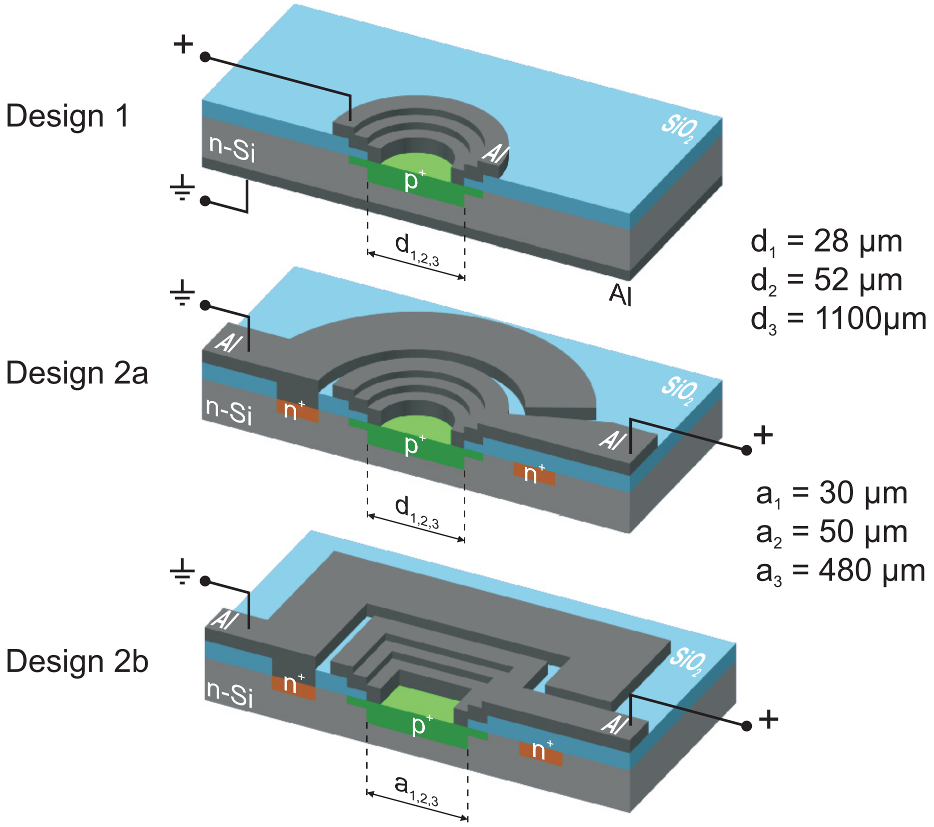

Figure 4.14: LED design.

conditions the electron current predominately flows in lateral direction (parallel to the substrate surface), so the electrons and holes recombine mostly at the boundary interface between the p^+- and n-Si. This effect was proofed by EL measurements. The EL intensity from the edge region of the LED was maximal, while the EL intensity in the middle region was close to zero. In the process of a new mask set development for design 2, two diode shapes were introduced - round and square shown in Fig. 4.14 2a and 2b, respectively. The diameters of the round diodes were kept the same as in design 1. The size length of square shaped diodes is $a_{1,2,3} = 30, 50, 480\ \mu m$.

4.4 Resonant microcavity LED with $CoSi_2$ bottom mirror

The main aim of this work was to fabricate a silicon pn-junction diode and to place this device into an optical microcavity, in order to create a silicon based microcavity enhanced light emitting device (MCLED). In this chapter processing of a device with the LED design 1 (Fig. 4.14) is described. The MCLED was designed to have only one Bragg mirror placed on the top of the active layer. As a bottom mirror we have decided to use a metallic$CoSi_2$ layer. The two main reasons for this decision were: firstly the fabrication of $CoSi_2$ by high fluence Co^+ ion implantation into the Si followed by thermal annealing for silicidation and secondly its metallic properties predestinate it to be used as a bottom contact.

4.4.1 Device preparation

The CoSi$_2$ layer is formed by ion beam synthesis based on Co$^+$ ion implantation (E = 200 keV, $\Phi = 2.2 \times 10^{17}$ cm^{-2}, T = 375°C) into n-doped (100) Si and subsequent annealing at 1100°C for 20 s [163]. The thickness of the Si top layer after CoSi$_2$ formation was too low and therefore the Si layer was overgrown using molecular beam epitaxy to a total thickness of 370 nm, corresponding to $1 \times \lambda_{MC}/n$ at a wavelength of 1150 nm, also called 1λ cavity[4].

Step	Structure	Remarks
1	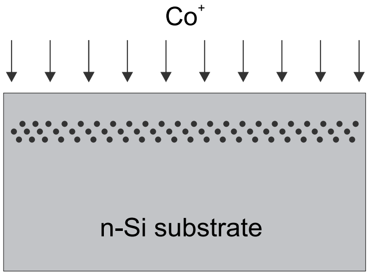	**CoSi$_2$ formation** (bottom mirror and bottom n-contact) a) n-doped (100) Si substrate b) Co$^+$ implantation (E = 200 keV, $\Phi = 2.2 \times 10^{17}$ cm^{-2}, T = 375°C) c) RTA annealing (T = 1100°C, t = 20 s) and CoSi$_2$ formation
2	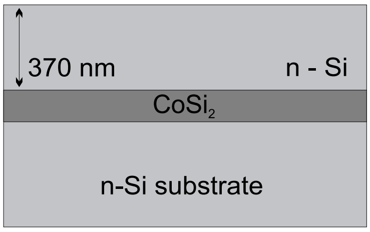	**Si active layer growth by MBE** (Forschungszentrum Jülich, Institute of Thin Films and Interfaces, Jülich, Germany)
3	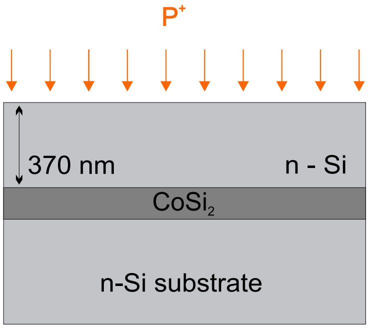	**n-doping** a) P$^+$ implantation (E = 90 keV, $\Phi = 4 \times 10^{12}$ cm^{-2}) b) annealing (T = 950°C, t = 60 s)
4	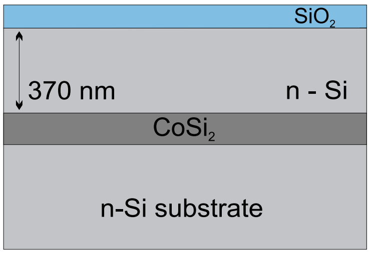	magnetron sputter deposition of 220 nm SiO$_2$

---

[4] λ_{MC} - microcavity (resonant) wavelength, n refractive index of an active layer (Si) at the microcavity wavelength

Step	Structure	Remarks
5	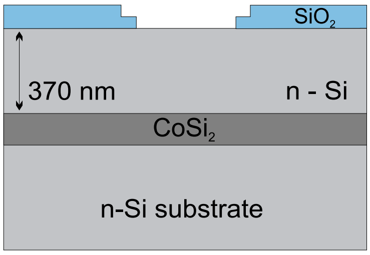	lithographic patterning of the oxide layer (mask 1 and 2)
6	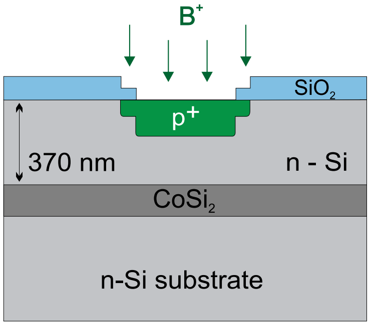	**p^+-doping** a) B^+ ion implantation ($E = 25$ keV, $\Phi = 4 \times 10^{15}$ cm^{-2}) b) annealing (1050°C for 10 min)
7	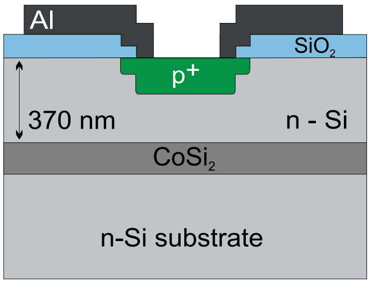	**Front contact** a) magnetron sputter deposition of Al (300 nm) b) lithographic front tide contact patterning (mask 3)
8	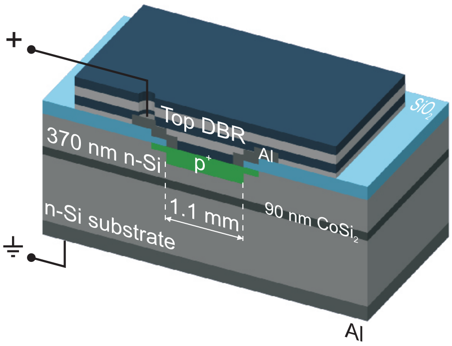	**MCLED** a) Al deposition (300 nm) for back side n-contact b) DBR deposition on the front side (2.5 pairs 185 nm SiO_2 / 75 nm Si) c) p^+-contact hole opening into the DBR by FIB sputtering

Table 4.6: Fabrication process of MCLED with $CoSi_2$ bottom mirror.

The Si layer was uniformly and highly n-doped (1.8×10^{17} cm^{-3}) by implanting P^+ ions ($E = 90$ keV, $\Phi = 4 \times 10^{12}$ cm^{-2}) and subsequent annealing ($T = 950$, $t = 60$ s). The Si pn-diode was formed by B^+ ion implantation ($E = 25$ keV, $\Phi = 4 \times 10^{15}$ cm^{-2}) into the MBE grown n-doped Si/$CoSi_2$ wafer and high temperature annealing at 1050°C for 10 min. An Al ring contact for the p^+-region of 1 mm inner diameter was evaporated and lithographically patterned.

The top Bragg mirror is fabricated by sputter deposition of alternating SiO_2 and a-Si layers of 185 nm and 75 nm layer thickness, respectively. Locally the top Bragg mirror is

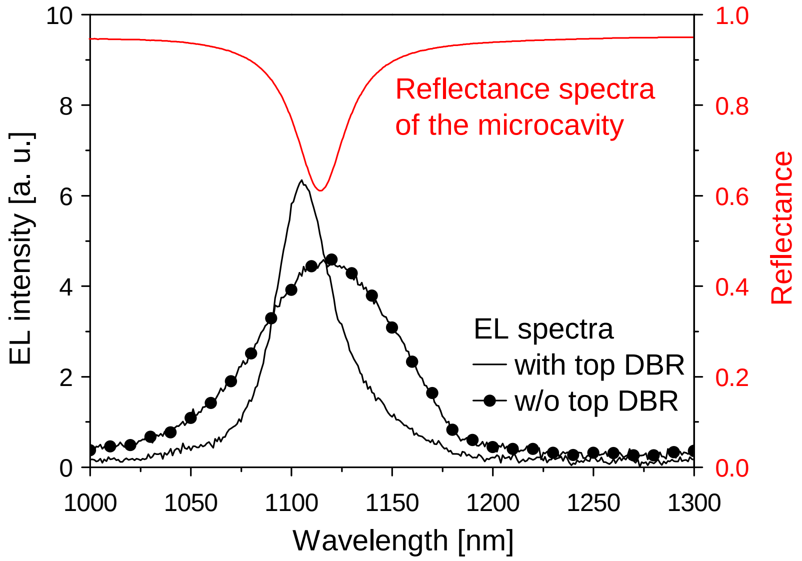

Figure 4.15: Electroluminescence spectrum of Si pn-diode with bottom $CoSi_2$ mirror.

removed above the Al ring to contact the diode from the top, while the bottom contact is provided through the back to the low resistivity n-type substrate. The device preparation sequence is shown schematically in Tab. 4.6.

4.4.2 Electrical Si diode characteristics

The current-voltage characteristics show an Ohmic behavior with a resistivity of 0.34 Ohm. Secondary ion mass spectroscopy of the diode reveals that the B has diffused from the implanted profile with a projected range of $R_p = 60$ nm down to the $CoSi_2$ contact probably due to a high defect density of the MBE grown Si layer. Nevertheless, EL is only observed when a forward bias is applied to the diode. In comparison to diodes with 0.1% power efficiency prepared by the same technique on high-quality Si, the EL intensity of the devices without top Bragg mirror at the same current densities dropped down by 2 orders of magnitude due to the almost short-circuited pn diode.

4.4.3 EL spectra

Figure 4.15 depicts the room-temperature EL spectrum of devices without and with Bragg mirror at a forward current of 500 mA. Additionally, the reflectivity spectrum measured within the front side Al ring contact of the diode is shown. The reflectivity spectrum exhibits a clear signature of a microcavity. The top Bragg mirror has a reflectivity of 94%. At the position matching λ_{MC}=1115 nm the reflectivity drops to 70%. This spectrum is in agreement with the modeling of the MC with a reflectivity of the Si/$CoSi_2$ interface of 75%. The bandgap EL spectrum of the device without Bragg mirror shows the same spectrum as previously reported for high-efficiency diodes [1, 5]. The linewidth of the spectrum is approximately 100 nm. With the top-Bragg mirror the linewidth is decreased by a factor of two while the peak intensity is increased by 46%. The maximum of the EL is shifted by 10 nm to lower wavelengths relative to the minimum in the reflectivity spectrum. This shift is within the range of scattering of the reflectivity minimum position over the processed wafer due to inhomogeneities of the layer thicknesses during sputter deposition.

4.4.4 Conclusions

A proof-of-principle of an electrically driven Si microcavity LED was demonstrated. Several possibilities for a further improvement of the output of the MC can be envisioned:

- Because of the B diffusion, the light emitting region is spread across the microcavity active layer. The coupling of the light emission into the microcavity mode is achieved. However, when the pn-junction is placed exactly in an antinode of the electric field distribution in the MC, the extraction efficiency is higher. This can be achieved by using rapid thermal annealing after the B^+ implantation which prevents the strong B diffusion as observed in the present case.

- The replacement of the bottom $CoSi_2$ mirror with a high reflectivity distributed Bragg reflector decreases the absorption losses.

- Further improvement is expected by better matching of the bottom and top reflectivity of the microcavity, e.g. with a top mirror, which allows a more accurate balancing of the top mirror reflectivity due to a lower refractive index contrast compared to Si/SiO_2 (e.g. SI_3N_4/SiO_2).

- An improvement of the top Si quality with a longer nonradiative lifetime could be gained by wafer-bonding methods.

- A three dimensional confinement could be achieved by lateral patterning of the active layer of the MC into a photonic crystal structure.

4.5 Si based microcavity LED with two DBRs

In the previous section (see Sec. 4.4) the proof-of-principle of an electrically driven Si microcavity LED was demonstrated, however, further improvement by optimisation of this device can be envisioned.

The idea was to replace the bottom metallic $CoSi_2$ mirror with a high reflectivity DBR consisting of a 5.5 pairs of 200 nm SiO_2 / 80 nm Si. The top DBR is formed by 3.5 pairs of the same multilayered system. The resonant cavity is thus asymmetric in order to provide preferential outcoupling of the light from the top. The expected spectral emission enhancement can be estimated from Ref. [6]. The calculations of an ideal device with 1λ-cavity for a resonant wavelength 1150 nm are summarised in Sec. 2.4.4.

However, for the final device we decided to use a 4λ microcavity, corresponding to a Si device layer thickness of about $d = 1300$ nm. This thickness has the advantage that exactly one longitudinal mode would be contained in the natural emission spectrum, even if the thickness slightly deviates from the desired value, since the mode spacing is roughly the same size as the natural linewidth ($\Delta\lambda_n = 110$ nm). Additionally, a device layer thickness of 1300 nm is also a good compromise for the mechanical stability of the device.

In order to get an effective Si pn-junction LED, high quality silicon is required [4, 5, 1, 87]. The main technological problem is to fabricate a stable thin silicon device layer containing the pn-junction with well defined thickness. A feasible solution is the use of a silicon on

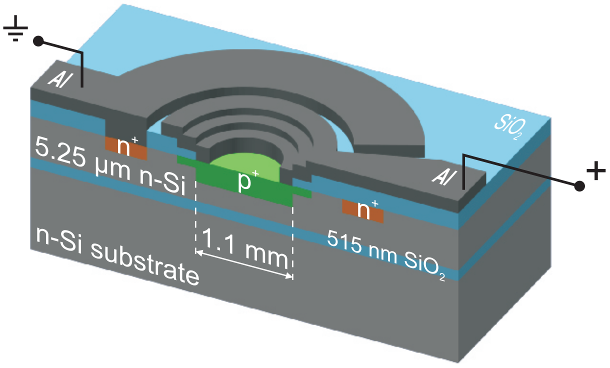

Figure 4.16: Test LED scheme

insulator (SOI) wafer (see Sec. 4.1.2) with a known thickness of the top device layer and to etch away the substrate down to the buried SiO_2 , which acts as an etch stop. After removing the buried SiO_2 , the DBRs are deposited at the top and at the bottom of the membrane.

4.5.1 Test device

In order to test the suitability of the SOI material, commercial 4 inch SOI wafers with a n-type (001) silicon device layer of a thickness of d = 5.25 μm are used as the starting material (resistivity 1. . . 20 Ωcm). The thickness of the buried SiO_2 layer is 515 nm.

The pn-diodes were fabricated using standard silicon planar technology and boron ion implantation into the top n-Si device layer. A boron fluence of $\Phi = 4 \times 10^{15}$ cm^{-2} was implanted at an energy of 25 keV. After furnace annealing at 1050 °C for 20 min, Al contacts were evaporated and lithographically patterned. The cross section sketch of the device is illustrated in Fig. 4.16.

Fabry-Perot fringes, seen from the room-temperature EL measurements (Fig. 4.17), with a period corresponding to the layer thickness of $d = 5.25\ \mu m$ are clearly observed. This demonstrates, that in principle SOI material can be used for the fabrication of the electroluminescent Si devices.

4.5.2 Device fabrication

As start material (step 1 in Tab. 4.7), 400 μm thick commercial 4 inch SOI wafers with a resistivity of the device layer 1. . . 5 Ωcm produced by IceMOS Technologies were used. The thickness of the (001) silicon n-type device layer is smaller than in the above test device, namely 2μm ± 0.5μm. The thickness of the buried SiO_2 layer given by manufacturer is 200 nm ± 5% (see 4.2).

Using multiple oxidation and oxide removal the device layer of the SOI wafer was thinned down to an average thickness of 1300 nm (step 2).

The pn-diodes were fabricated using standard silicon planar technology and boron ion implantation into the top n-Si device layer similar to the test devices (step 3). A boron fluence of 4×10^{15} cm^{-2} was implanted at an energy of 30 keV. In order to contact the top n-Si layer, n^+-regions were formed around the p^+ layer by phosphorus ion implantation ($\Phi = 5 \times 10^{14}$ cm^{-2}, E = 25 keV).

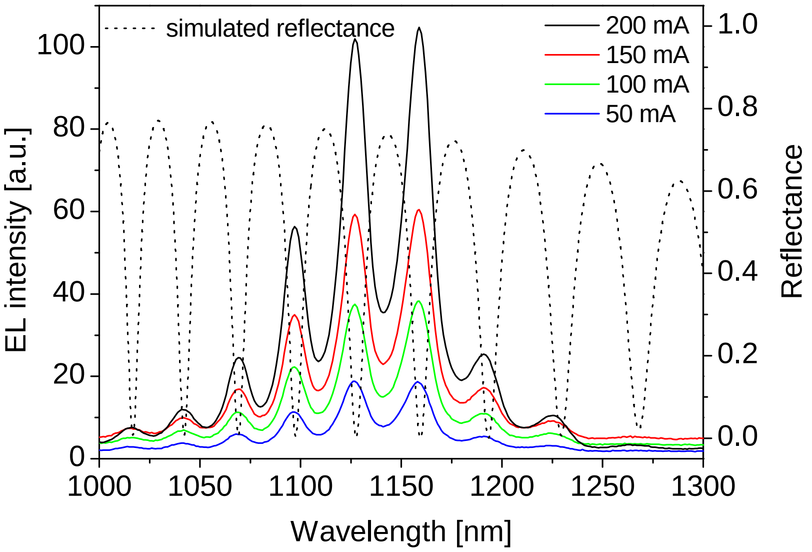

Figure 4.17: Electroluminescence spectrum of Si pn-diode in a 5.25 μm thick SOI device layer for different forward currents and simulated reflectance spectrum.

After furnace annealing at 1050°C for 20 min, Al contacts were evaporated and lithographically patterned (step 4). The cross section scheme of the device can be seen in step 4 (LED on SOI).

The fabrication of the thin Si membranes is connected with very long (6 - 7 hours) KOH wet chemical etching of the Si substrate. The details are described in Sec. 3.1.3. For this purpose a mask layer resistant against the aggressive KOH is needed. Silicon dioxide and silicon nitride are good candidates. However, KOH etching of silicon dioxide is observable. The etch rates of 350-400 nm/hour for 30 % KOH at 80°C are considerably slower (2 orders of magnitude) than that of silicon but a very thick oxide layer of $\geq 2.8\mu m$ is needed when deep etching is performed with SiO_2 as etching mask. The silicon nitride etch rate is less than 1 nm/hour. Therefore, already a relatively thin Si_3N_4 layer can be used as an effective KOH etch mask. A 500 nm silicon nitride film was deposited on the back side of the substrate (step 5). Windows into the silicon nitride and the silicon dioxide from the back side of the substrate were made by wet etching in concentrated hot phosphoric acid (85% H_3PO_4 at 160°C) and in buffered HF, respectively (step 6a, 6b).

There are in principle two ways how to protect the already processed front side of the wafer during the KOH etching. The first possibility is the use of temporary protective coatings (i.e. ProTEK^{TM}). These coatings are compatible with a variety of semiconductor materials and are able to withstand and survive the etch process without decomposing or lifting off. However, about 5 mm broad edge lifting at the wafer boundary was observed. ProTEK^{TM} coatings are removed after the etch process with ProTEK^{TM} Remover. For deeper cleaning an oxygen plasma process must be used. The removal of the ProTEK^{TM} coating necessitates a lot of mechanical handling, which can be critical for larger membranes (2 mm^2). Additionally an oxygen plasma cleaning cannot be used when Al contacts are already present on the front side.

Step	Structure	Remarks
1	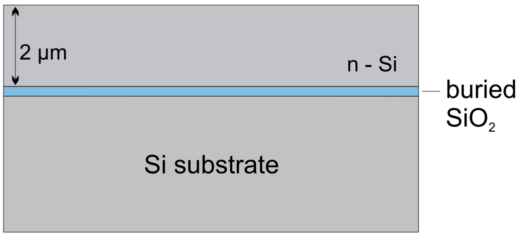	SOI substrate: a) handle wafer: n-type (100) Si, 400 μm$\pm$5 μm b) device layer: n-type (100) Si, 2 μm$\pm$0.5 μm c) buried SiO$_2$: 200 nm$\pm$5 %
2	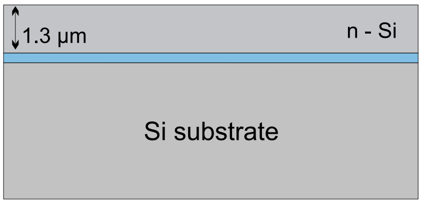	Thinning of the device Si layer: multiple wet oxidation and oxide etching
3	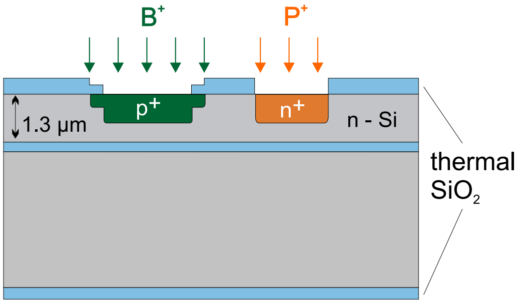	Silicon planar technology: a) oxidation 220 nm SiO$_2$ and lithographical patterning of the oxide (resist masks for B$^+$ and P$^+$ ion implantation) b) p$^+$-doping: B$^+$ implantation Φ = 4$\times$10^{15} cm^{-2}, E = 25 keV c) n$^+$-doping: P$^+$ implantation Φ = 5$\times$10^{14} cm^{-3}, E = 30 keV d) annealing (1050°C, 20 min, N$_2$)
4	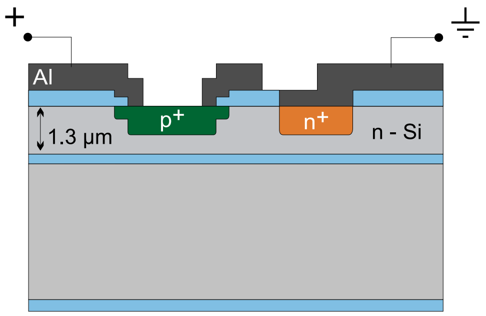	**LED on SOI** Contacts: a) 300 nm Al deposition and lithographical patterning b) annealing (400°C, 30 min, N$_2$)
5	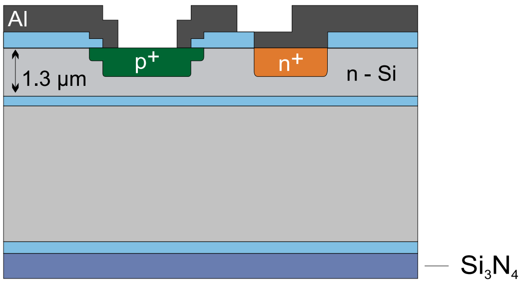	PECVD deposition of 500 nm Si$_3$N$_4$ on the SOI wafer backside

Step	Structure	Remarks
6	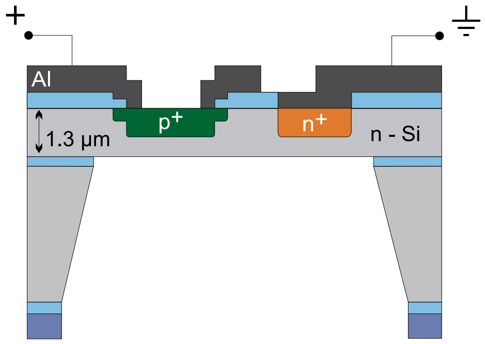	**LED on a thin membrane** back side etching: a) lithographical patterning and etching of nitride b) local etching of oxide c) KOH etching of the Si substrate (etch stop - buried oxide) d) etching of the buried oxide
7	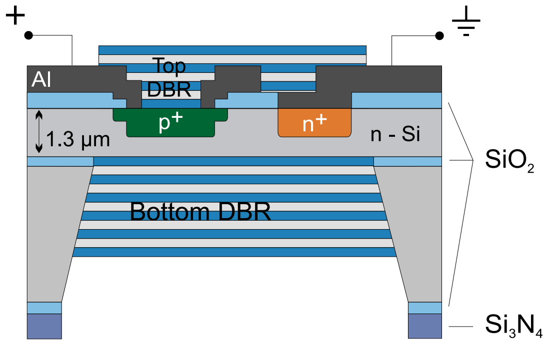	**MCLED** a) bottom DBR: sputter deposition 5.5 pairs of 200 nm SiO_2 / 80 nm Si b) top DBR: local sputter deposition 3.5 pairs of 200 nm SiO_2 / 80 nm Si through a deposition mask
8	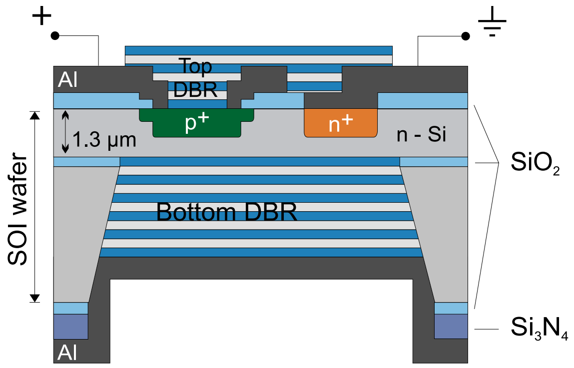	**MCLED** sputter deposition of 1000 nm Al on the wafer back side

Table 4.7: Fabrication process of MCLED.

The second possibility how to protect the front side of the wafer is to use a vacuum wafer handling system from Silicet [164]. The system is composed of a vacuum box and a special vacuum wafer holder. This holder is made for chemical etching of silicon wafers (see App. A.2). The wafers are held securely by means of vacuum seals, thus protecting them reliably from the etching agent. The protected wafer surface inside the wafer holders is ventilated to provide pressure compensation.

The use of this method for wafer surface protection demands careful handling of the wafer. In particular, the 5 mm broad edge area, where the sealing lips of the holder are sucked on the wafer, is usually gripped with tweezers forming micro scratches. The thin layer of protective Si_3N_4 does not adhere on these scratches and the silicon is etched under the sealing lips. If the channels become deep enough, the vacuum under the sealing lips is broken and the etchant penetrates inside of the holder and damages the already processed front side.

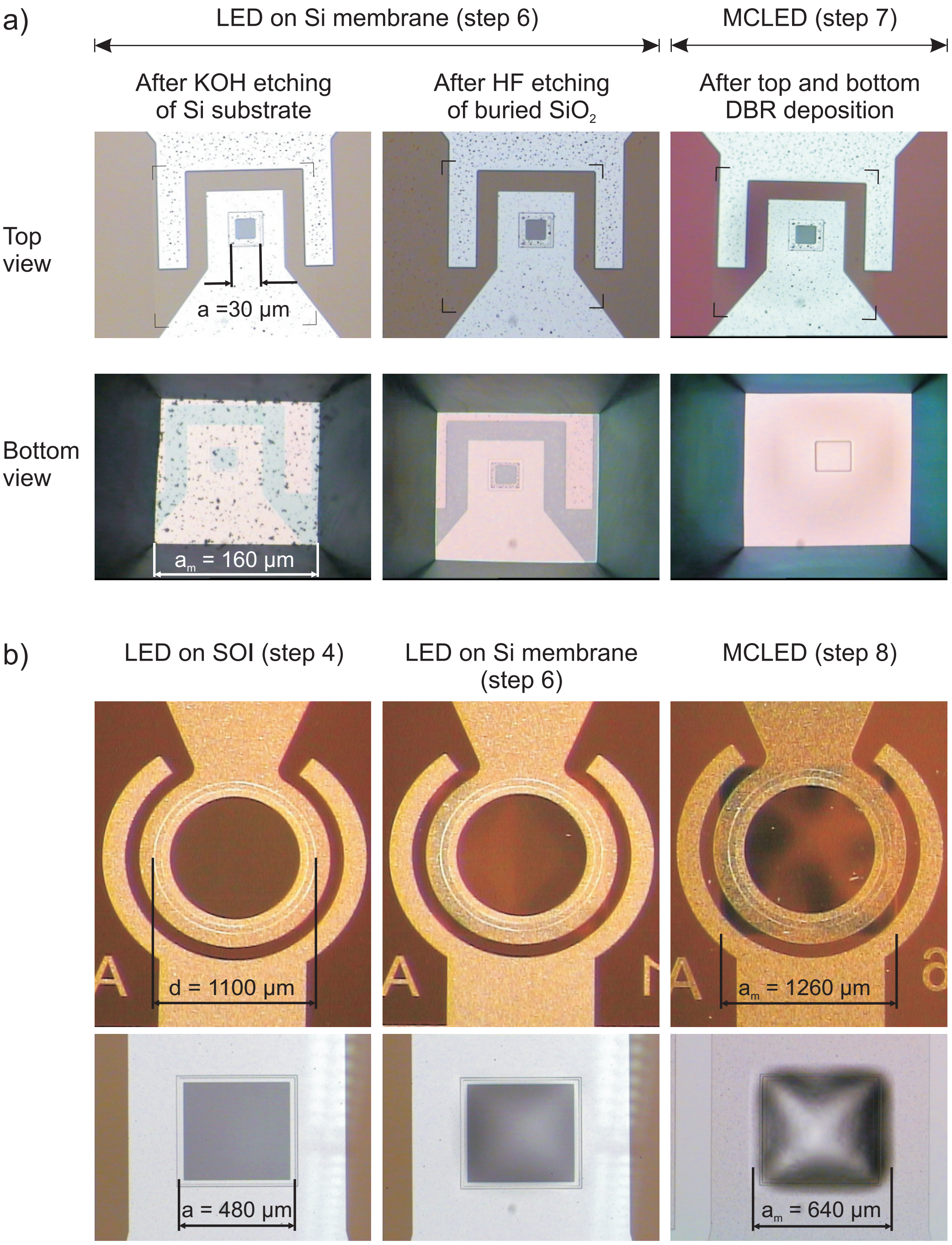

Figure 4.18: Bright field light microscope images of the LED after different fabrication steps. a) First row - top view of the square LED with a = 30 μm. Second row - bottom view. b) First row - top view of the round LED with d = 1100 μm. Second row - top view of the square LED with a = 480 μm. MCLED images in b) clearly show the stress in membranes.

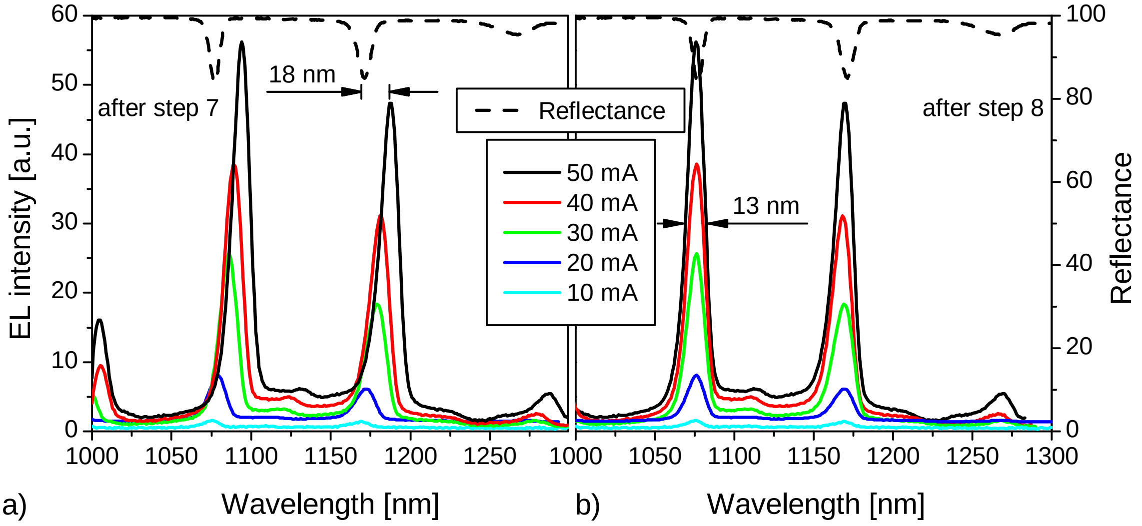

Figure 4.19: Electroluminescence and reflectance spectra of MCLED: a) after fabrication step 7 (bottom DBR / 1650 nm active Si layer / top DBR), b) after fabrication step 8 (1000 nm Al / bottom DBR / active Si / top DBR) for different forward currents.

The Si etching in the KOH/H_2O solution is connected with bubble formation. After ca. 6 hours of KOH etching 400 μm deep windows into the substrate are opened and the etchant reaches the buried oxide, which acts as a KOH etch stop (step 6c). The bubble formation stops. After KOH etching some particles remain on the back side of the membrane (Fig. 4.18 a).

In step 6d the 200 nm buried oxide layer is removed using a buffered HF solution (for details see Sec. 3.1.3). Different etch rates of SiO_2 for different membrane sizes were observed. The etch rate of the SiO_2 is about 75 nm / min. During HF etching of the buried SiO_2 particles remained from the KOH etch process were also removed (Fig. 4.18 a - bottom view).

LEDs on Si membranes are under the stress. The stress is visible in the light microscope images especially for the case of large membranes (Fig. 4.18 b - step 6) and increases after the sputter deposition of the DBRs on the top and the bottom of the membrane (step 7).

The electroluminescence spectrum of this device for different forward currents is shown in Fig. 4.19a. The left figure corresponds to the MCLED after fabrication step 7 consisting of bottom DBR, 1650 nm thick active layer and the top DBR. An increased current leads to a shift of the EL towards higher wavelengths compared to the reflectance spectrum. This spectral shift is due to a refractive-index increase, resulting from the current induced temperature increase. The spectral shift of 18 nm at a forward current of 50 mA (solid black line) corresponds to the change in the refractive index of silicon by about 0.05, which corresponds to a temperature increase by more than 300 K (i.e. up to 600 K). The temperature dependence of the refractive index of silicon at the wavelength 1150 nm is plotted in Fig. 4.19. The data taken from the literature [165] (black symbols) have a linear dependence in the temperature range between 50 K and 300 K. We suppose that for the higher temperatures the tendency is similar (solid red line, linear fit). The influence of the increased thickness of the active layer due to thermal expansion of Si on the optical properties is negligible for this temperature.

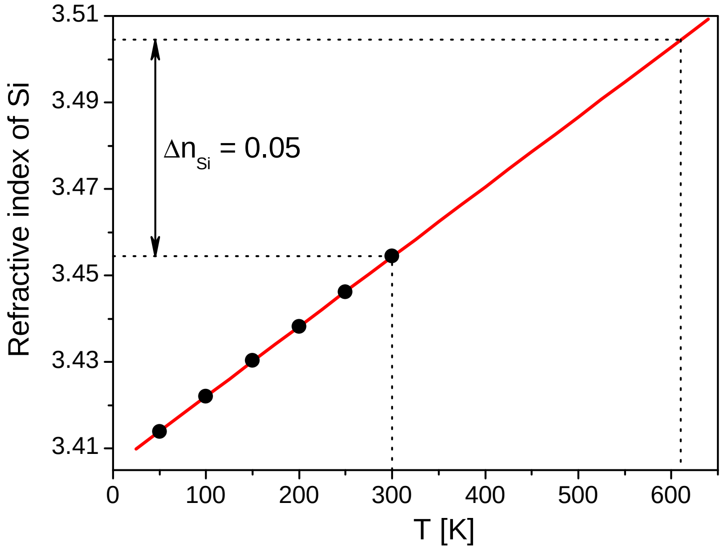

Figure 4.20: Temperature-dependent refractive index of silicon. The black symbols are the values $n = f(T)$ for 1150 nm wavelength [165] and the solid red curve is a linear fit.

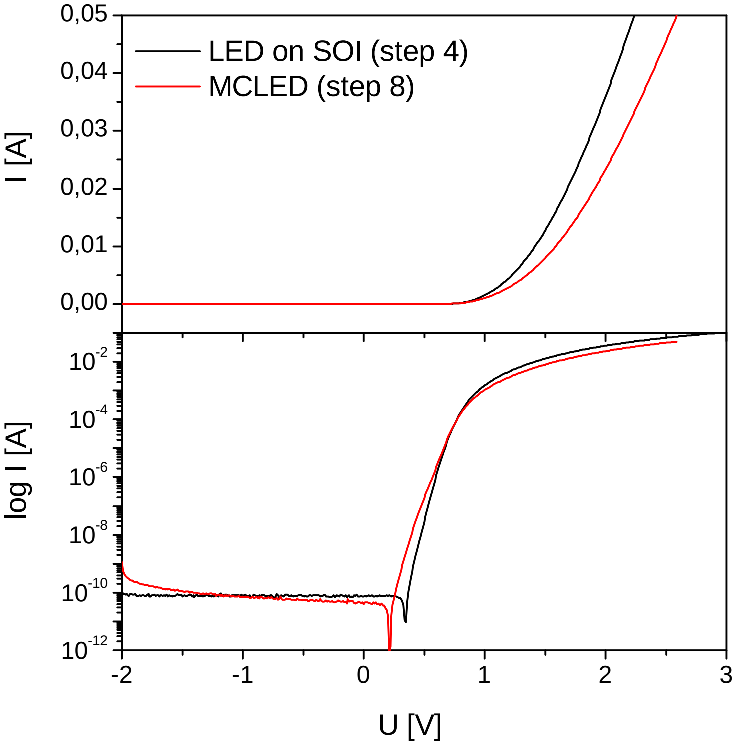

Figure 4.21: I-V characteristics of the device after two different fabrication steps.

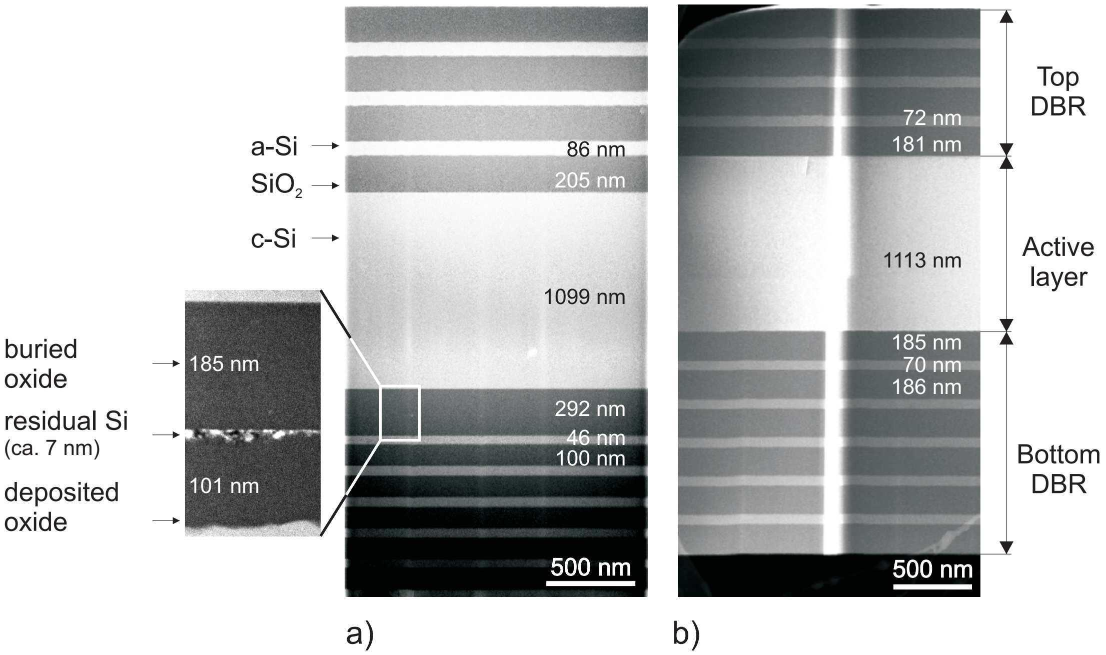

Figure 4.22: TEM cross section images of the two different MCLEDs. a) The top and the bottom DBRs of this MCLED were fabricated with the same deposition parameters. Large differences in SiO_2 and Si layers thicknesses in the top and the bottom DBR stacks are visible. Detail: First layer of the bottom DBR composed of buried oxide, residual Si from the substrate and sputter deposited SiO_2 . The buried SiO_2 could not be removed by BHF etching due to not completely KOH etched Si substrate. b) Deposition times of SiO_2 and Si layers in the bottom DBR stack were doubled.

In order to solve the problem of the spectral shift and to reduce the heating of the membrane, the deposition of a metal layer with a high thermal conductivity can be attempted. A 1000 nm aluminum layer was sputter deposited on the bottom resonator in fabrication step 8. The electroluminescence spectrum of the same device as in Fig 4.19a with a deposited Al layer for different currents is plotted in Fig. 4.19b. No shift is observed anymore.

Fig. 4.21 shows the I-V characteristics of the LED on SOI (after fabrication step 4) and MCLED (after step 8). During the electrical measurements the stress in the multilayered MCLED is probably responsible for the increase of the series resistance. The sputter induced defects in the thermally grown SiO_2 and at its interface to sputter deposited layers lead to an increase of the leakage current for large reverse bias (-2V). Annealing of the defects after sputter deposition of the DBRs was not done in order to avoid membrane breaking.

After nondestructive electrical and optical chracterisation, samples for cross section TEM were prepared (Fig. 4.22a). The cross section TEM investigation showed that the SiO_2 and Si layers in the top and the bottom distributed Bragg multilayered stacks have different thicknesses despite using the same deposition parameters. The layers in the bottom stack are about half as thick as in the top stack. The reason is that the membranes are placed in relatively deep grooves and the effect of shadowing during deposition plays a big role. The membrane area a_m^2 is about 160×160 μm^2 and the grooves etched from the substrate side are about 400 μm deep. The comparison of the sputter deposition on

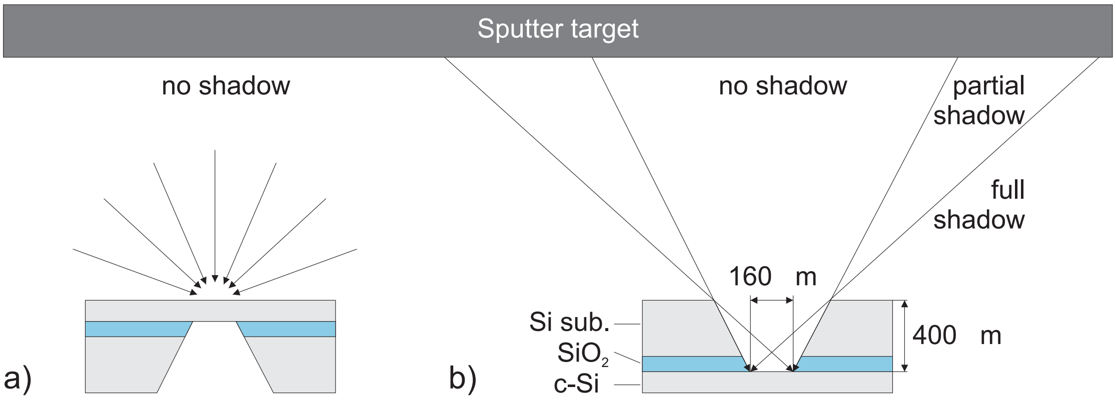

Figure 4.23: Sputter deposition on a planar surface (a) and into a V-groove (b).

a planar surface and into a V-groove is sketched in Fig. 4.23. The geometrical estimation calculated by a 3D graphical program Blender [166] is about 50% of shadowing, which corresponds well to the results.

Additionally a thin layer of Si (about 7 nm) having remained from the substrate was found in some cases on the buried oxide (detail in Fig. 4.22a). This residual Si layer prevented etching of the buried SiO_2 in BHF before bottom DBR layer deposition. During the dipping of the wafer into a buffered HF solution in order to remove the buried oxide layer in the deep grooves, bubbles formed in the grooves inhibit an effective and complete buried SiO_2 etching.

The wrong thicknesses of SiO_2 and Si layers in the bottom DBR together with the remaining buried oxide and residual Si from the substrate lead to the broadening of the electroluminescence peaks, which was much large than expected from the microcavity. The FWHM of the EL maximum in Fig. 4.19 is 13 nm.

A new set of SOI wafers was processed with corrected sputter deposition parameters. The TEM cross section image shown in Fig. 4.22b clearly demonstrates a device with completely removed Si substrate and buried oxide. The thicknesses of the sputtered Si and SiO_2 in the bottom DBR using a doubled deposition time are roughly in the desired thickness range. However, a deviation from the expected 200 nm SiO_2 and 80 nm Si is visible. The reason is the position of the device on the wafer used for TEM characterisation. The TEM image in the Fig. 4.22a is taken from the sample placed in the central region of the SOI wafer. The device used for cross section TEM in the Fig. 4.22b was located more than 20 mm away from the wafer centre, where the deposition rate is slower by about 10 % (see also Fig. 4.8 and 4.3).

4.5.3 LED on SOI versus MCLED

In this section the results of optical and electrical characterisation of silicon light emitting pn-diodes on SOI wafers (after fabrication step 4, Fig. 4.24a) and of the final microcavity enhanced LED (after fabrication step 8, Fig. 4.24b) are compared.

In order to obtain a 4λ-cavity MCLED, the silicon device layer must be 1300 nm thick. The initial Si top device layer of SOI wafers has been thinned down to this value. However, because of its high thickness variation (± 500 nm), it is not possible to control exactly the Si device thickness over the wafer for every diode. The value of 1300 nm is only the average thickness value over the SOI device layer. This is the reason for relatively

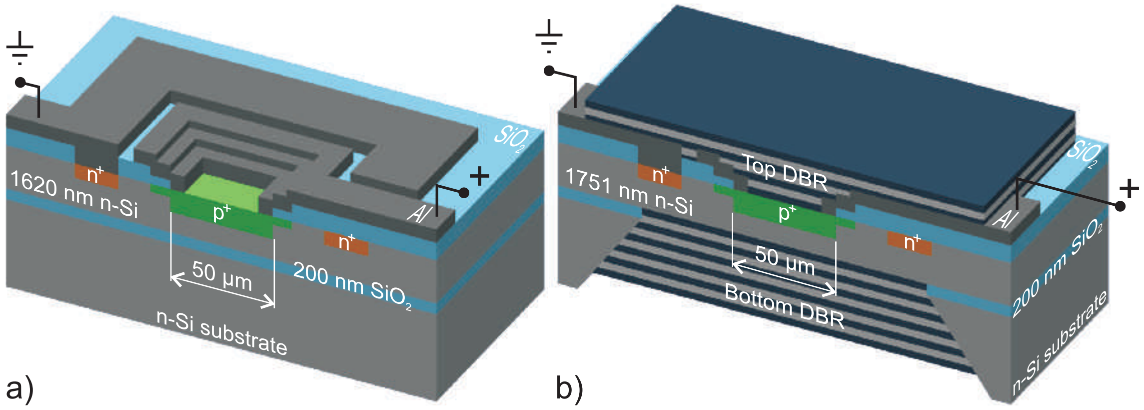

Figure 4.24: Scheme of a) LED on SOI and b) MCLED.

high thicknesses deviations of the active layers of the analysed devices LED on SOI and MCLED from the desired value.

The LED on SOI studied in this section was fabricated on a 1620 nm thick device layer with 200 nm buried oxide.

The MCLED consists of a 1751 nm thick active device layer and two distributed Bragg reflectors. The overview of the thicknesses of all layers in the MCLED stack can be found in Tab. 4.8. The values are obtained from TEM cross section imaging and reflectivity measurements.

In the case of the MCLED the buried oxide layer was not completely etched away and ca. 140 nm buried oxide was left. This is the reason for the 340 nm thick SiO_2 layer No. 9, which slightly shifts the luminescence and the reflectance spectrum to higher wavelengths and diminishes a little the quality of the cavity.

Both of the devices have a square design (Fig. 4.14-2b) with the side length of a = 50 μm (Fig. 4.14). Schematics of the investigated devices: LED on SOI and MCLED are shown in Fig. 4.24 a) and b), respectively.

Measurements of EL, PL and reflectance perpendicular to the device surface

The EL measurements were performed using an experimental setup in the Institute for Solid State and Materials Research (IFW) Dresden (see Sec. 3.2.4). The microscope of the EL setup is equipped with a long-working-distance objective with a magnification of 20x and a numerical aperture of 0.4.

Fig. 4.25 shows the extracted EL (black circles) measured at room-temperature, the PL (red squares) and the reflectance (blue triangles) perpendicular to the device surface (θ'=0°) for a) the LED on SOI and b) the MCLED. In the case of LED on SOI, due to the small thickness of the active layer (1620 nm) and its relatively high refractive index compared to the surrounding media (air and buried oxide), this device already behaves as a 5λ Fabry-Perot resonator with the resonant wavelength at 1148 nm, having the full width at half maximum (FWHM) of 32 nm. The peaks are separated by $\lambda_{FSR} = 105$ nm. The measured extracted EL spectrum of MCLED plotted in Fig. 4.25 b) shows four sharp peaks (in the spectral range between 950 nm and 1300 nm). The highest resonance peak at 1146 nm with a FWHM of 8 nm corresponds to the 5.5 λ cavity of the MCLED shown in Fig. 4.24 with the thickness of the active layer of 1751 nm. The peaks are separated by $\lambda_{FSR} = 88$ nm.

No.	Layer	Thickness [nm]	Structure
1	SiO_2	185	Top DBR
2	a-Si	73	
3	SiO_2	188	
4	a-Si	75	
5	SiO_2	180	
6	a-Si	80	
7	SiO_2	195	
8	c-Si	$L_{cav} = 1751$	Device layer
9	SiO_2	340	Bottom DBR
10	a-Si	68	
11	SiO_2	198	
12	a-Si	63	
13	SiO_2	195	
14	a-Si	70	
15	SiO_2	198	
16	a-Si	68	
17	SiO_2	195	
18	a-Si	68	
19	SiO_2	200	

Table 4.8: Layer stack of MCLED.

The PL of both of the diodes was measured at the same experimental setup. The samples were excited by 635 nm picosecond pulses generated by a PicoQuant, LDH-P-C-635B laser head controlled by a PDL-800B driver. The position of the PL peaks corresponds well with the EL maxima.

The reflectance was measured by Fourier transform infrared spectroscopy. As a reference a silver mirror was used. Fabry-Perot fringes of the LED on SOI with a period corresponding to the layer thickness of 1620 nm are clearly observed (Fig. 4.25 a). In the case of MCLED, having the thickness of the active layer of 1751 nm and a refractive index at 1150 nm $n = 3.542$, the 5.5λ cavity would be expected at a resonance wavelength of 1128 nm. The reason for the 18 nm spectral shift ($5.5\lambda_{res} = 1146$ nm) is the 140 nm thick residual oxide remained under the active Si device layer. In both cases the reflectance peak minima are located exactly above the maxima of the EL an of PL spectra.

In the table of Fig. 4.25 c) the optical constants of Si, a-Si and SiO_2 at the wavelength 1150 nm used for EL and R calculations are summarized. The index of absorption is set to zero for computational reasons.

Fit of EL, PL and reflectance spectra

In the next step fits of the measured EL, PL and R data are performed. The thicknesses of the stacks of both of the samples are known from cross section TEM images and from FTIR measurements.

The simulation programs SCOUT and UniMCO, in detail described in Sec. 3.2.2 and 3.2.4, respectively, assume only laterally homogeneous structures. They do not take into account any layer thickness variation, surface roughness or inhomogeneities as well as pn-junction boundaries.

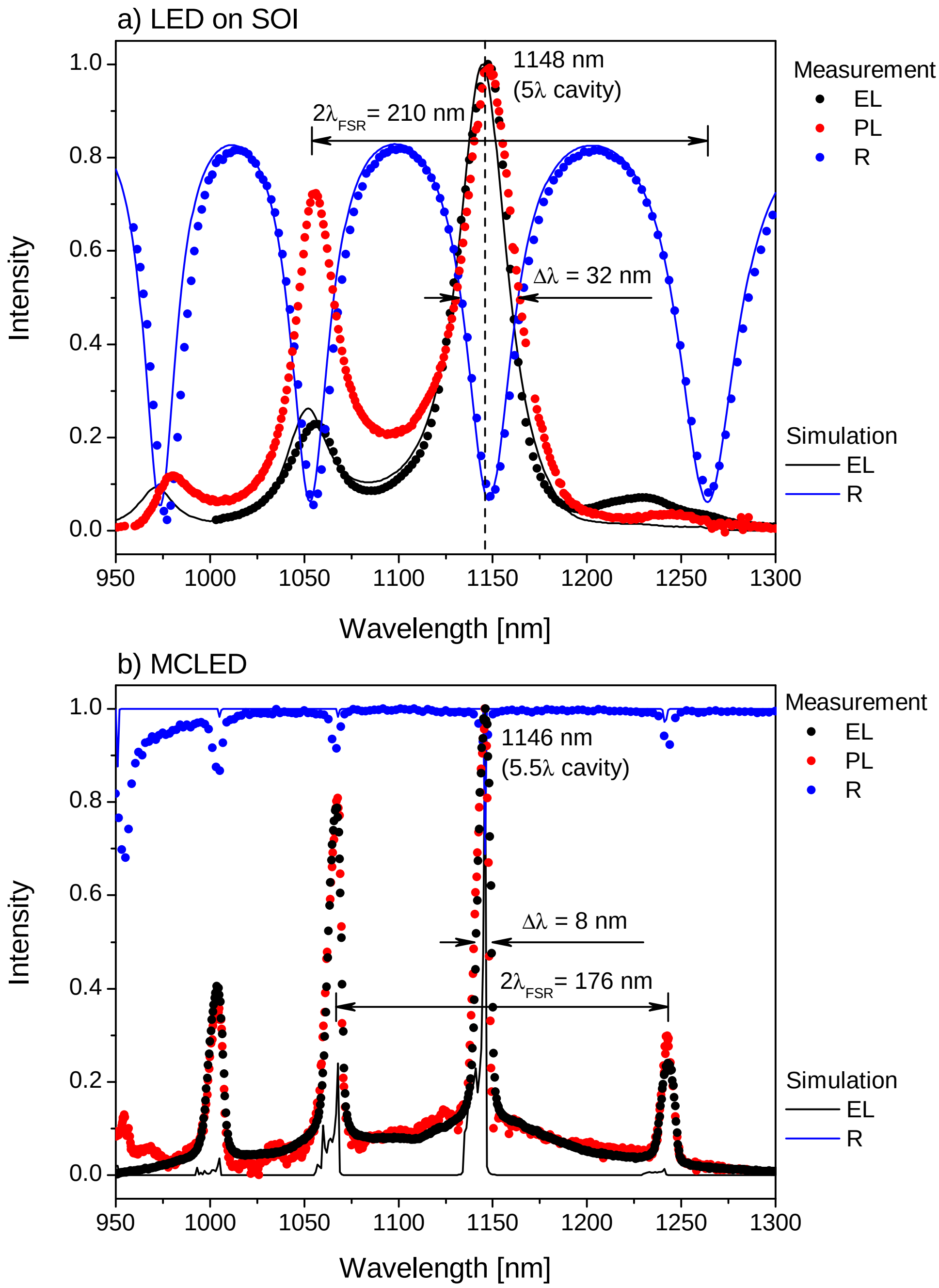

c) Optical constants

Material	Index of refraction ***n*** at 1150 nm	Index of absorption **k** at 1150 nm
Si	3.54193	0
a-Si	3.564	0
SiO_2	1.4486	0

Figure 4.25: Electroluminescence (black), photoluminescence (red) and reflectance (blue) of the LED on SOI (a) and MCLED (b). The dots represent the measured values and the lines are the simulation results. (c) Optical constants of Si, a-Si, SiO_2 at 1150 nm used in R and EL calculations.

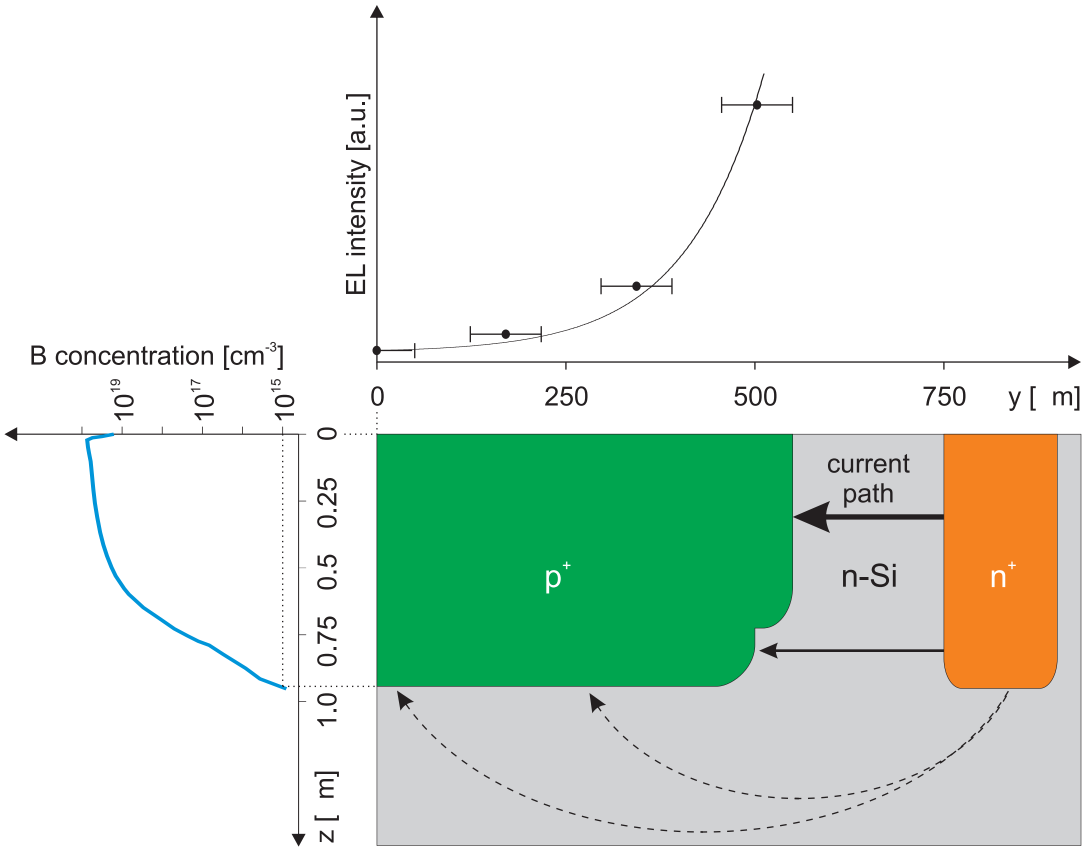

Figure 4.26: Cross section sketch of the pn-diode with radius r=550 μm. The arrows show theoretical current paths. The highest probability of e-h recombination is between the p$^+$-region and n$^+$-region, where the current path is the shortest. Top: EL intensity measured at different distances from the center of the diode (symbols are measured values, black solid line is here to guide the eye). Left: the SIMS measurement of the boron concentration implanted into the silicon (blue solid line), measured in the central part of the diode (y = 0 μm).

In the case of reflectivity measurements the doping profile of the active layer (pn-junction) has no influence on results. The incoming light beam is relatively broad and therefore homogeneously distributed over the diode. It reflects on the interfaces of all layers and is collected by a detector. Inhomogeneities of layer thicknesses in the stack can lead to a decrease of the reflectivity and the thicknesses determined by the simulation are only average values. Palik's optical constants of Si (crystalline silicon) and of SiO_2 , being materials of the active layer and of the buried oxide, respectively, were used [95] in the simulation. The optical constants of sputtered a-Si and SiO_2 forming the multilayered DBR stacks are taken from Fig. 4.10 ($P_{SUB} = 100$ W) and 4.5 ($P_{SUB} = 0$ W), respectively. The optical constants of Si, a-Si and SiO_2 at the wavelength 1150 nm used for EL and R calculations are summarized in the table c) of Fig. 4.25. The fits in both cases (LED on SOI and MCLED) correspond well with the measured data (solid blue lines in Fig. 4.25 a) and b).

The situation is different for the electroluminescence spectra. The p^+- and n^+-contacts are placed on the top and around the pn-junction (Fig. 4.26). The current flows mostly parallel to the surface, which is the shortest path. For this reason the recombination takes place preferentially at the side of the pn-junction. This fact was also experimentally observed. The EL measurements across the area of a pn-diode with the largest diameter of $d = 1100$ μm have shown that the EL intensity is largest at the pn-junction boundary (Fig. 4.26 top). In the central region of the pn-junction ($y = 0$) with a diameter of ca. 100 μm and at a current of 100 mA only a very weak electroluminescence was observed.

The SIMS measurement (measured in the center of the pn-diode $y = 0$) of the boron concentration profile implanted into the silicon with an energy of 25 keV, a fluence of 4×10^{15} cm^{-2} and annealed for 20 min at 1050 °C in N_2 is shown in Fig. 4.26 - left. The resistivity of the n-type device layer of the SOI wafer is 1-5 Ωcm, which corresponds to a phosphorous concentration of 10^{15} cm^{-3}. After annealing the boron atoms diffuse into a depth of about 950 nm (pn-junction). However as already mentioned before in this case due to the diode design the recombination preferentially takes place parallel to the surface.

The result of this observation is that for the EL calculation of the diodes with an inhomogeneous emitting layer the emission depth (somewhere between 0 nm and 950 nm) and the average emitting layer thickness have to be found.

- Determination of the emission depth (parameter x_{EZ} in Fig. 2.19) in the active layer: In the first step the electric field amplitude was calculated (red solid line in Fig. 4.27). The calculation was done for the wavelength a) 1148 nm in the case of the LED on SOI sample and b) 1146 nm for the MCLED corresponding to the resonance maximum at an emission angle of 0°. In further electroluminescence calculations the pn-junction was located in the antinode of the electric field amplitude (green solid lines), in both cases at $x_{EZ} = 485$ nm far from the surface of the silicon device (active) layer (yellow area). Independent of the depth, the placement of the pn-junction into another antinode (± 162 nm) leads to the same EL simulation results.

- Estimation of the thickness of the emitting layer (parameter d_{EZ} in Fig. 2.19): The thickness of the light emitting zone d_{EZ} in the EL calculations was varied from 1 nm to 500 nm. As an input light spectrum for the calculation, the normalised measured EL data of a Si pn-LED, fabricated with the same parameters on bulk silicon wafers (published by J. Sun in [1, 89]) have been used. The calculated EL spectra were normalised and compared with the EL measurements of the diodes having the same size and design. Fig. 4.28 a) and b) show the generated EL data as a function of the wavelength and of the thickness of the light emitting zone d_{EZ} for a) LED on SOI and b) MCLED, respectively. The highest intensity would be obtained for narrow emitting zones ($d_{EZ} \rightarrow 0$). The best agreement between the calculated EL and measured data of a) the LED on SOI and b) the MCLED were achieved for the thickness of the emitting zone of d_{EZ} = 375 nm (also seen as a light yellow area in Fig. 4.27). However, in the case of MCLED the measured peaks with the FWHM of 8 nm are significantly broader than the calculated value of 1 nm (measurement - black symbols, simulation - dashed black line in Fig. 4.29e). This is partially due to the broad light collection angle of the objective in the EL experimental setup, as will be discussed in the following.

Angular dependence of the electroluminescence

The measurement of the angular dependence of the EL was performed at the experimental setup of the IFW. During the measurement the sample was fixed in a special holder with the possibility of tilting the sample. The results of extracted EL of LED on SOI (a-d) and MCLED (e-h) measured under the angles of θ' = 0°, 5°, 10° and 15° are plotted in Fig. 4.29 as black, red, green and blue symbols, respectively.

In order to fit the measured data, the same EL calculation as before, has been performed, but for the angle range of -88°. . . 88° in steps of 1°.

The measured and the calculated data of EL for angles θ' = 0°, 5°, 10° and 15° of LED on SOI (a) and MCLED (b) are shown in the Fig. 4.29 as symbols and dashed lines, respectively. The data were normalised with respect to the data measured/calculated for the angle 0° (normal to the device surface). The measurements differ from the simulations for higher angles especially in the case of the MCLED. The maxima of the measured spectra become broader and the intensity is lower. The reason is that during the measurement the microscope objective collects not only a discrete angle but a certain angular range. Nevertheless, the shift of the peak to shorter wavelength is consistent with simulation.

In the next step the average extracted EL spectra for θ' = 0° ± 0°, 0° ± 5°, 0° ± 10°, 0° ± 15°, 0° ± 20° and 0° ± 25° were calculated and compared to the experimental values. The same was done for the angles θ' = 5°, 10° and 15°. The best fit was obtained for the angular range ± 25° (solid lines in Fig. 4.29 and solid black lines in Fig. 4.25), which corresponds well with an acceptance angle of the optical system of $2\phi = 48.16°$ equipped with a long working distance objective (20x) having a numerical aperture of NA = 0.4. The data were again normalised with respect to the data for 0°±25°. A very good agreement between the EL measurement and the simulation (0°±25°) for different angles is obtained in the case of the sample LED on SOI (a). Certain differences between the measurement and the simulation for 0°±25° of the sample MCLED (b) are visible. This is due to the simplifications in the calculation (no absorption or inhomogeneities). Nevertheless the position of the peaks and their width in the simulation is very close to measurements. The FWHM of the resonant maximum increases by factor of 4 (from $\Delta\lambda$ = 1 nm to $\Delta\lambda$ = 4 nm), if in the simulation a collection angle of ±25° is taken into account. This value is only by a factor of 2 smaller than the measured value of $\Delta\lambda$ = 8 nm.

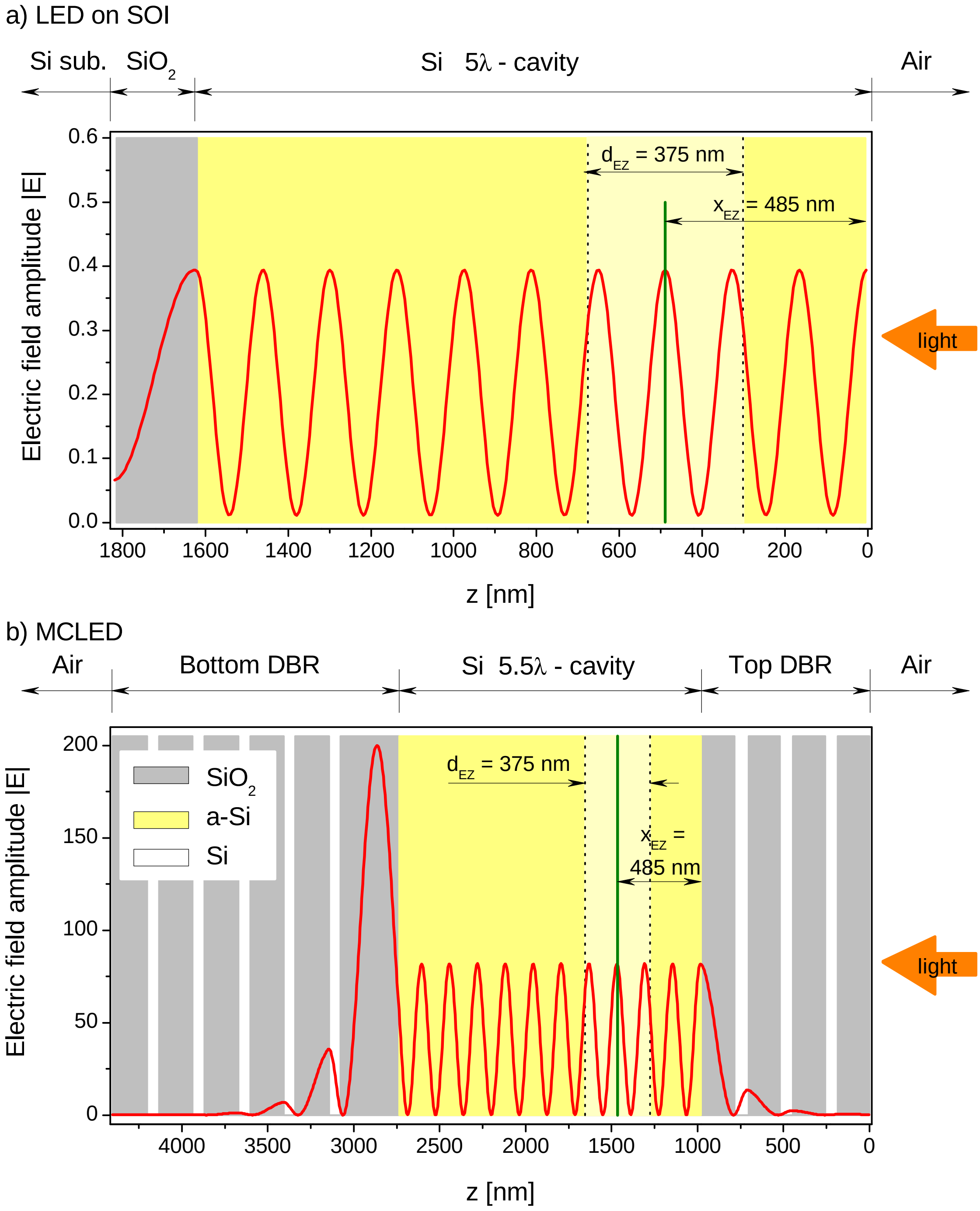

Figure 4.27: Calculated electric field amplitude (red solid line) of a) the LED on SOI and b) the MCLED. In the further EL calculation the position of the emitting zone was placed into an antinode of the electric field amplitude into the depth of $x_{EZ} = 485$ nm under the surface of the active layer (green solid line) and has a thickness of $d_{EZ} = 375$ nm (black dashed lines).

a) LED on SOI

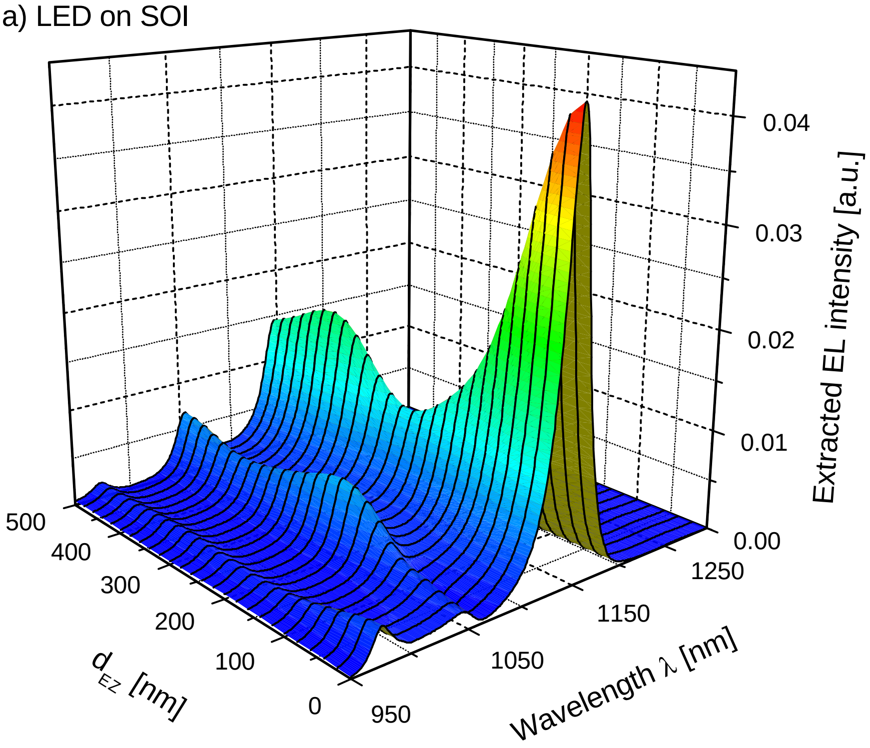

b) MCLED

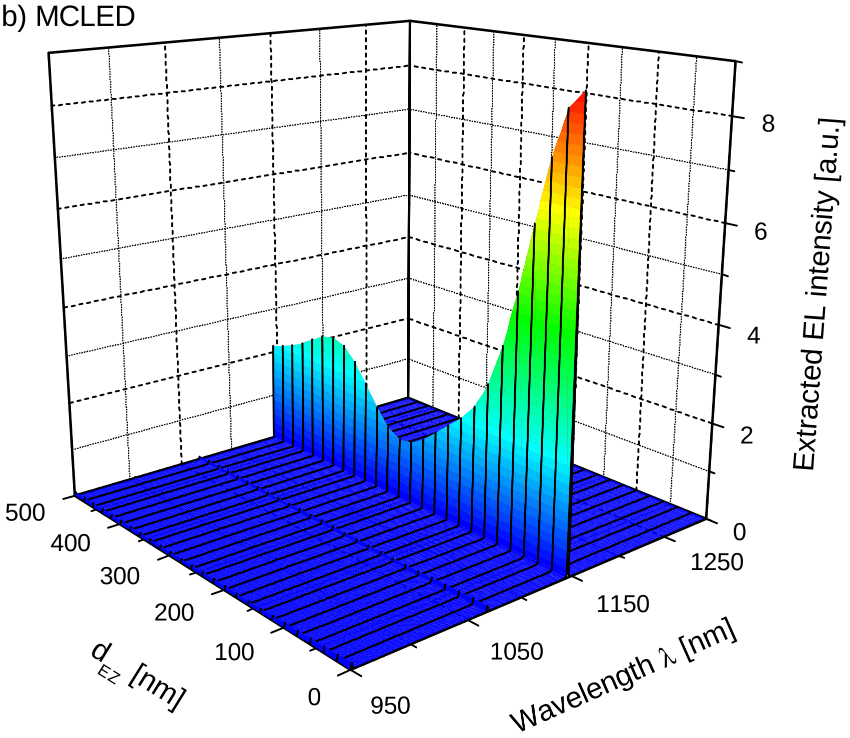

Figure 4.28: Calculation of the electroluminescence as a function of the wavelength and the thickness d_{EZ} of the light emitting zone.

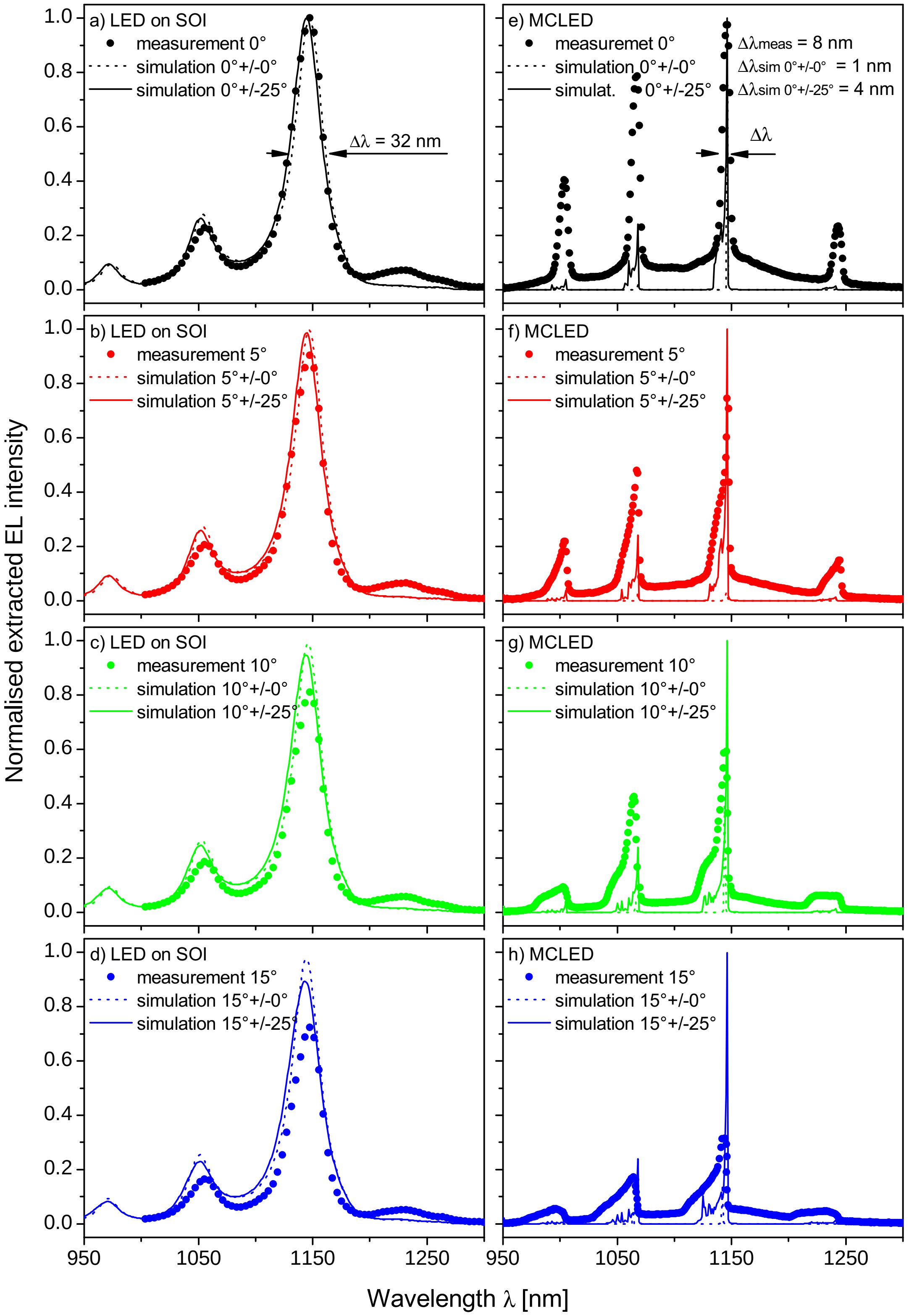

Figure 4.29: Comparison between EL measurements (symbols) and calculations (dashed lines for $\theta` = 0°\pm0°$, solid lines for $\theta` = 0°\pm25°$) of extracted EL for $\theta' = 0°$, 5°, 10° and 15° (relative to the surface normal) of LED on SOI (a-d) and MCLED (e-h).

Enhancement

Up to now only the normalised measurement results have been shown. However, an interesting question remains, whether the enhancement can be quantitatively measured or calculated.

The absolute emission intensity of silicon pn-diodes strongly depends on the quality of the wafer material. Since the silicon material of the SOI device layer was not available in the fortm of a bulk material (wafer) for the diode fabrication, it is not possible to evaluate the enhancement by the Fabry-Perot resonator directly from the measurements.

In Fig. 4.30 the measured EL spectrum of the MCLED (black symbols) is compared with the EL spectrum of the LED on SOI (green symbols). Both of theese devices have been fabricated on the same SOI wafer and the EL measurements have been performed using the same experimental setup by keeping the same measurement parameters and temperature.

The solid lines in Fig. 4.30 correspond to the calculated extracted EL spectra for a collection angle of $\alpha = \pm 25°$. The shape of the simulated EL spectrum of the LED on SOI (green solid line) corresponds well to the shape of the measured EL peak. Therefore the measured EL spectrum of the LED on SOI was scaled in such a way that the measurement and the simulation match together. The measured EL spectrum of the MCLED was scaled with respect to the EL measured for the LED on SOI. The solid black line corresponds to the EL simulation of the MCLED. The position and the width of the resonant peaks in simulation match well with the measured data (4.5λ resonant peak at 1003 nm, 5λ at 1065 nm, 5.5λ at 1146 nm and 6λ and 1242 nm). However, the absolute EL intensities do not fit perfectly to the experimental data. The differences are mainly due to the absorption of the materials, inhomogeneity of the emitting layers, layer thickness variations (of all individual layers) and roughness. In order to enable the calculation of the enhancement and of the efficiency by the use of the Fabry-Perot resonator, additionally an extracted EL of a simple Si-LED has been calculated (red solid line). In the calculation the emitting zone was placed 485 nm under the surface of a 400 μm thick silicon layer (typical thickness a bulk Si wafer) into the antinode of the electric field amplitude. The thickness of the emitting zone was set to $d_{EZ} = 375$ nm. The used input EL$_0$ data are again the normalised EL data of the pn-LED fabricated on a different n-type Si substrate material with $\rho = 1 \ldots 20\ \Omega cm$ and with the same fabrication parameters as the LED on SOI and MCLED devices.

From the comparison of the measured and the simulated spectra in Fig. 4.30 (measured with the collection angle of $\theta' = 0°\pm25°$ and simulated for the extraction angle of $\theta' = 0°\pm25°$) the following conclusions can be drawn:

- The finesse of the measured resonant emission peak is 3.3 in the case of the LED on SOI and 11 for the MCLED. The simulation gives the values of $F(\text{LEDonSOI})_{sim0°\pm25°} = 3.4$ and $F(\text{MCLED})_{sim0°\pm25°} = 22$, which is a factor of two larger than measured. In the case of the LED on SOI, the finesse of the simulated spectrum corresponds well with the measured spectra.

- The quality factors (peak position/peak width) determined from the measured EL spectra are $Q(\text{LED})_{meas} = 10$, $Q(\text{LEDonSOI})_{meas} = 36$ and $Q(\text{MCLED})_{meas} = 143$. From the simulation the following results of the quality factors are obtained: $Q(\text{LED})_{sim0°\pm25°} = 10$, $Q(\text{LEDonSOI})_{sim0°\pm25°} = 37$, $Q(\text{MCLED})_{sim0°\pm25°} = 287$. There is a good agreement between the simulation and measurement, except the factor of two for the MCLED.

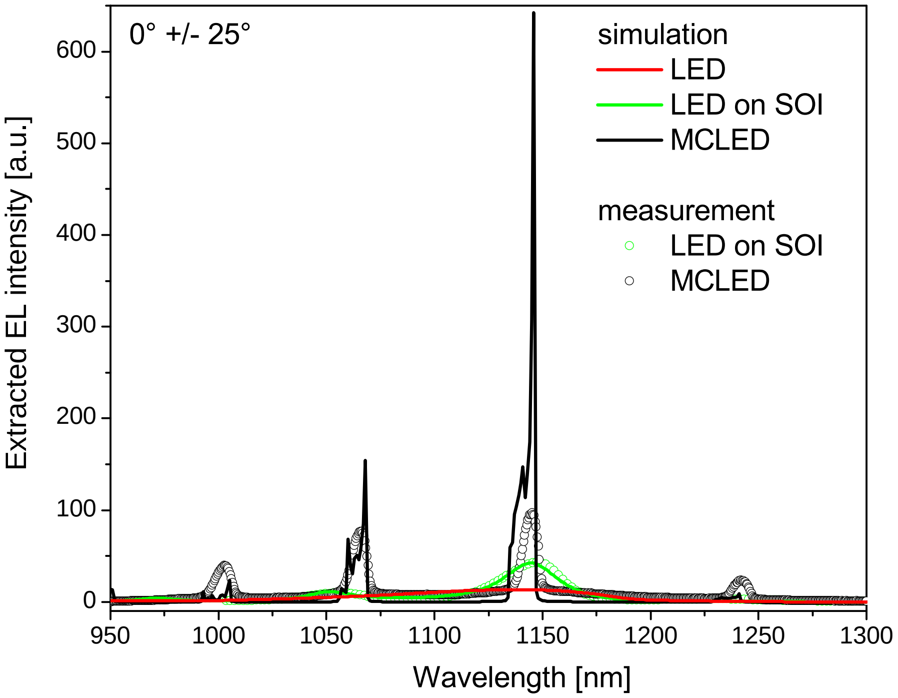

Figure 4.30: Direct comparison of the measured (symbols) and simulated (solid) extracted EL spectra of LED (red), LED on SOI (green) and MCLED (black) for collection angle ±25°.

- Compared to the bulk Si-LED, the EL intensity at the resonance wavelength of λ = 1148 nm of the LED on SOI is enhanced only by the value of G_e = 3.3 due to the weak Fabry-Perot effect of this device structure. There is a good agreement between measured and simulated data.

- In the case of the MCLED, at the resonance wavelength of λ = 1146 nm the expected simulated spectral emission enhancement is $G_{e(sim0^\circ \pm 25^\circ)} = 49.4$ (compared to the bulk Si-LED). The measured emission spectrum at the resonance wavelength, however, is only enhanced by a factor of 7.5, mainly limited by the absorption and the inhomogeneities of layers in DBRs.

- The emission enhancement of the measured extracted EL intensity integrated over the wavelength range of 950 nm…1300 nm is $G_{int}(\text{LED on SOI})_{meas}= 1.36$ for the LED on SOI and $G_{int}(\text{MCLED})_{meas} = 2.24$ in the case of the MCLED. From the simulation the integrated enhancements are $G_{int}(\text{LED on SOI})_{sim0^\circ \pm 25^\circ} = 1.36$ and $G_{int}(\text{MCLED})_{sim0^\circ \pm 25^\circ} = 1.77$.

The remaining question is: What would be the difference if the extracted EL measured in the direction perpendicular to the surface would be collected only in a very small collection angle $\theta' \pm \delta\theta'; \delta\theta' \rightarrow 0°$? The EL measurements using very small apertures led to the lowering of the EL intensity so that the results could not be interpreted in a meaningful way. However, the information about the extracted EL intensity of the simple bulk silicon LED, the LED on SOI and the MCLED at the extraction angle θ' = 0°±0° can be obtained from the simulation. Fig. 4.31 shows the comparison of the calculated extracted EL intensity of LED on silicon bulk material (red), LED on SOI (green) and

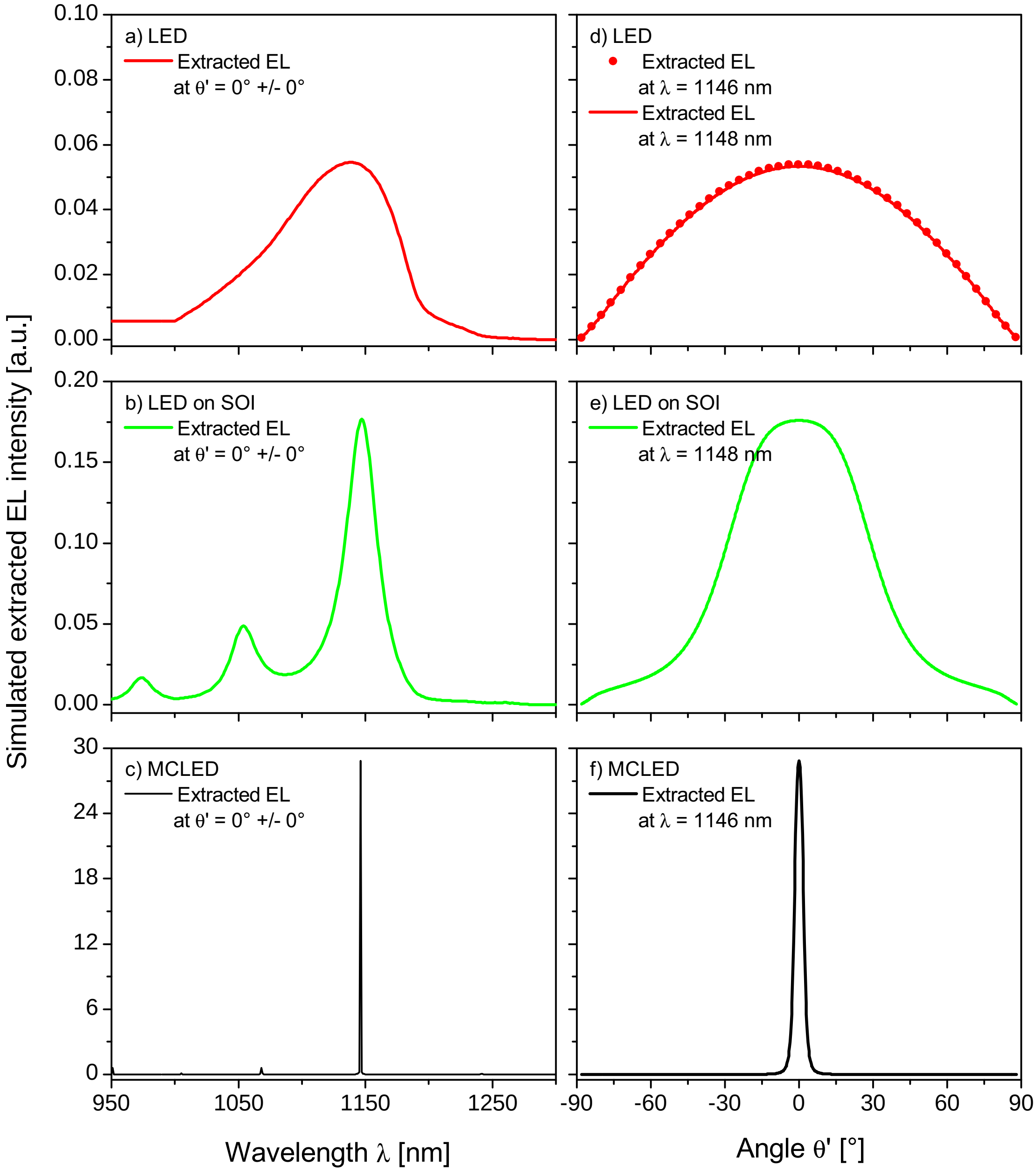

Figure 4.31: Comparison of the calculated extracted EL intensities of silicon bulk LED, LED on SOI and MCLED in dependence on the wavelength at the angle $\theta' = 0°$ (a-c) and on the angle at the resonant wavelength (d-f). The Fabry-Perot effect visibly leads to the narrowing of the extracted EL spectra and the increasing of the EL intensity (c, f) even for a non-ideal MCLED system with the structure plotted in Fig. 4.24.

MCLED (black) as a function of the wavelength λ at θ' = 0°±0° (a-c) and as a function of angle θ' at the wavelength: (d) LED: 1146 nm and 1148 nm, (e) LED on SOI: 1148 nm and (f) MCLED: 1146 nm. The Fabry-Perot effect leads to the significant narrowing of the extracted EL spectra and an increasing of the EL intensity even for non-ideal cavity systems (b, c, e, f).

The comparison of the extracted EL spectra calculated for the extraction angle of θ' = 0°±0° of the LED on SOI and the MCLED with those of the LED on a silicon bulk material leads to the following conclusions:

- The finesse $F_{sim0^\circ\pm0^\circ}$ of the LED on SOI and of the MCLED are 3.5 and 87, respectively.
- The quality factors Q of the devices are $Q(\text{LED})_{sim0^\circ\pm0^\circ}= 10$, $Q(\text{LEDonSOI})_{sim0^\circ\pm0^\circ}= 38$ and $Q(\text{MCLED})_{sim0^\circ\pm0^\circ}= 1146$.
- The spectral emission enhancement $G_{e(sim0^\circ\pm0^\circ)}$ are 3.2 for the LED on SOI and 529 in the case of the MCLED.
- The integrated emission enhancements $G_{int(sim0^\circ\pm0^\circ)}$ of the LED on SOI and of the MCLED are 1.36 and 4.6, respectively.

The calculations of the extracted EL spectra integrated over the whole angular range $(-88^\circ \ldots + 88^\circ)$ as a function of the wavelength and over the wavelength range (950 nm…1300 nm) in dependence on the emission angle are plotted in Fig. 4.32 a) and b), respectively. Again comparing LED and MCLED, a strong emission enhancement mainly at the resonant wavelength (but also couple of other modes are enhanced) and preferentially at the angle normal to the surface (θ' = 0°) is visible. In the case of LED on SOI a slight enhancement of the integrated extracted EL intensity (ca. by a factor of two) at the resonant wavelength of 1146 nm is observable, however the angular distribution of the extracted EL integrated over the wavelength has still a Lambertian distribution.

Compared to the LED on a bulk silicon material, the calculated extracted emission enhancement integrated over the whole angle and wavelength range $G_{int} = f(\lambda, \theta')_{sim}$ are 1.32 for LED on SOI and 1.76 for MCLED.

4.5.4 Conclusions

A microcavity enhanced LED fabricated on a thin silicon membrane with two distributed Bragg reflectors has been demonstrated. The thickness of the active layer of this device is 1751 nm, which corresponds to 5.5λ-cavity at the resonant wavelength 1146 nm.

As a reference an LED in the device layer of the same SOI wafer with an active layer thickness of L_{cav} = 1620 nm has been evaluated. Since the thickness of the device layer is in order of the emission wavelength, and due to the relatively high refractive index of silicon compared to the buried SiO_2 at the bottom of the device layer and air at the top (at 1150 nm: $n_{Si} = 3.52$, $n_{SiO2} = 1.46$, $n_{air} = 1$), this device behaves as a low efficient 5λ-cavity Fabry-Perot resonator with the resonant wavelength 1148 nm.

The results of electroluminescence and reflectance measurements of these two light emitting devices were compared to the simulation. From the EL simulations of the LED on a 400 μm thick silicon layer (typical thickness of a Si wafer), LED on SOI and the MCLED the extracted, guided and leaky efficiencies of these devices can be determined and compared.

With respect to LED efficiencies the following results have been obtained:

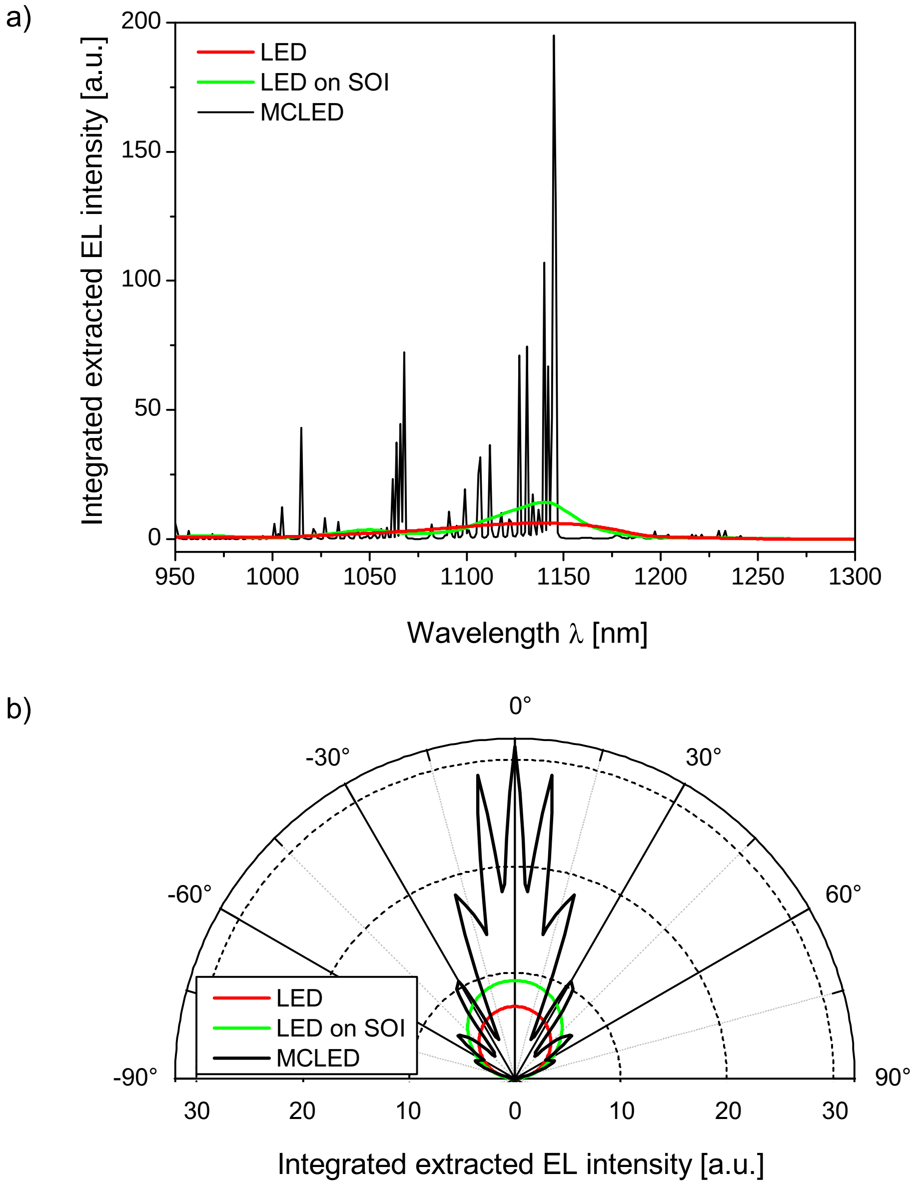

Figure 4.32: Calculated extracted EL intensity of simple Si-LED (red lines), LED on SOI (green lines) and MCLED (black lines) integrated over the angular range (-88°. . . +88°) as a function of the wavelength (a) and integrated over the wavelength range (950 nm. . . 1300 nm) in dependence on the extracted emission angle θ’ (b).

- The extracted efficiency η_{extr} of the simple Si-LED is only 3% and 97% are absorbed by the substrate as leaky efficiency η_{leaky}.
- The LED on a 1620 nm thin SOI device layer show a small increase of the extracted efficiency to $\eta_{extr} = 4\%$. According to the calculation 84% are leaky and 12% are guided efficiencies.
- In the case of the MCLED an extraction efficiency can be expected up to 26% for the ideal case of a 1λ cavity with SiO_2 /a-Si layers in the top and the bottom DBR having exact thicknesses of quarter of the emission wavelength (see Sec. 2.4.4). However, in case of our non-ideal MCLED stucture is the calculated extraction efficiency $\eta_{extr} = 5\%$. Nevertheless, it is a significant enhancement compared to the LED on a bulk silicon material, what clearly demonstrates the improvement due to the Fabry-Perot resonant effect. From the calculation can be concluded that 47% are guided and 48% are leaky efficiencies.

Finally, for the overview all measured and calculated results from the extracted EL intensity spectra of the devices LED (on a bulk silicon material), LED on SOI and MCLED are summarised in Tab. 4.9

Device		LED	LED on SOI	MCLED
Resonance peak at [nm]	measurement	1138	1148	1146
	calculation for 0° ± 0°	1138	1148	1146
	calculation for 0° ± 25°	1138	1148	1146
Resonance peak height [$a.u.$]	measurement	—	43	97.2
	calculation for 0° ± 0°	0.055	0.177	29
	calculation for 0° ± 25°	13	43	642
FWHM $\Delta\lambda$ [nm]	measurement	110	32	8
	calculation for 0° ± 0°	110	30	1
	calculation for 0° ± 25°	110	31	4
Peak separation λ_{FSR} [nm]	measurement	—	105	88
	calculation for 0° ± 0°	—	104	87
	calculation for 0° ± 25°	—	105	88
Finesse F	measurement	—	3.3	11
	calculation for 0° ± 0°	—	3.5	87
	calculation for 0° ± 25°	—	3.4	22
Quality factor Q	measurement	10	36	143
	calculation for 0° ± 0°	10	38	1146
	calculation for 0° ± 25°	10	37	287
Spectral emission enhancement G_e	measurement	—	3.3	7.5
	calculation for 0° ± 0°	—	3.2	529
	calculation for 0° ± 25°	—	3.3	49.4
Integrated emission enhancement G_{int}	measurement	—	1.36	2.24
	calc. over λ for 0° ± 0°	—	1.36	4.60
	calc. over λ for 0° ± 25°	—	1.36	1.77
	calc. over λ for 0° ± 88°	—	1.32	1.76
Extrac. efficiency η_{extr} [%]	calculation for 0° ± 88°	3	4	5
Guided efficiency η_{guided} [%]	calculation for 0° ± 88°	0	12	47
Leaky efficiency η_{leaky} [%]	calculation for 0° ± 88°	97	84	48

Table 4.9: Summary of the results.

Chapter 5

Summary and outlook

5.1 Summary

This thesis was focused on the development of microcavity enhanced silicon light emitting diodes (MCLED), their design, fabrication, and experimental as well as theoretical analysis.

Based on the theoretical background described in Chapter 2 and the measured electroluminescence (EL) spectrum of simple bulk silicon pn-diodes published by Sun [1] an ideal Si based 1λ MCLED has been simulated for a resonance wavelength 1150 nm. According to the calculations using this approach the quality factor of the device can be enhanced by a factor of 115 to the value of $Q = 1150$ at the resonance with a full width of the half maximum of 1 nm. The calculated enhancement of the extracted emission spectrum of the MCLED in the direction perpendicular to the LED surface is $G_e = 1930$. The extraction efficiency increases from the value of 3% (simple Si LED) up to 26% (MCLED).

The realisation of the aim of this work was split into the following steps: a) structural and optical investigations of single SiO_2 and amorphous Si (a-Si) layers fabricated by magnetron sputter deposition, b) deposition and characterisation of multilayer stacks of SiO_2 /a-Si forming the distributed Bragg reflectors and c) design, fabrication and characterisation of the completely processed MCLED.

In the first experiments the properties, homogeneity, the thickness variation over the wafer and the deposition rates of single a-Si and SiO_2 layers, produced by magnetron sputter deposition, have been investigated. The goal was to find optimal deposition parameters, which allow the fabrication of high quality multilayer stacks based on a-Si and SiO_2 , forming a distributed Bragg reflectors (DBR). The investigations have shown that the structural and optical properties of the deposited material strongly depend on the deposition process parameters. The most critical variable parameter during the sputter deposition was the substrate bias. The use of a substrate bias of about 60 V (substrate power 100 W) leads to an increase of the density of silicon films and the deposition rate as well as to a slightly higher refractive index. Additionally, the surface roughness of the silicon films becomes lower. The magnetron sputter deposition of SiO_2 films using a substrate power of 100 W results in a higher density, fewer defects, a lower deposition rate and a higher refractive index of the deposited SiO_2 films. However, a higher layer thickness variation over the wafer and an instability of the deposition process were observed. The conclusion of this investigation was that in the further work the a-Si films were deposited with the use of the substrate bias and SiO_2 films without it.

Subsequently, the optical properties of the distributed Bragg reflectors (DBRs) were investigated. A DBR as a periodic structure can be formed on the substrate by deposition of alternating layers with different index of refraction. The thickness of each optical layer corresponds to one quarter of the wavelength for which the mirror is designed. In order to get the DBRs well tuned for the resonant wavelength 1150 nm, the thicknesses of the SiO_2 and a-Si layers must be 198.47 nm and 80.67 nm, respectively. In real DBR systems thickness deviations of about 10% over the wafer and also from layer to layer were observed, which degradates slightly the properties of the DBRs. The use of a substrate bias during the deposition of the a-Si layers results in their higher density and lower roughness, and thus in an increase of the reflectivity of the DBRs by about 1%. The choice of the magnetron sputter deposition process for the fabrication of the DBRs was done because of itis a well established semiconductor fabrication technique. The compatibility with the CMOS technology was one of the key issues of this work.

In a MCLED the spontaneous internal emission is controlled by placing the emitter inside an optical cavity with a thickness of the order of its emitting wavelength. The resulting interference effects increase the part of the emission that can be extracted. In this work two different concepts have been followed a) MCLED with a bottom $CoSi_2$ mirror and top DBR, and b) MCLED with two DBRs.

In the first concept the 1λ thick silicon light emitting layer was embedded between metallic $CoSi_2$ mirror at the bottom and 2.5 pairs SiO_2 /a-Si DBR at the top. The whole system is placed on a bulk Si substrate and was fabricated by cobalt implantation into the silicon wafer, where after annealing a 90 nm thin $CoSi_2$ layer was formed. Using molecular beam epitaxy the thickness of the Si top layer was overgrown to a total thickness of 370 nm, corresponding to an approximately 1λ MC at a wavelength of 1150 nm. The result of the investigation of this system is that due to the B diffusion, the light emitting region is fully spread across the microcavity active layer. The coupling of the light emission into the microcavity mode was achieved. However, a further enhancement of the extracted efficiency could be possible by placing the pn-junction exactly into an antinode of the electric field distribution in the MC.

The second concept was based on silicon pn-diode placed between two DBRs. The expectation was that the replacement of the $CoSi_2$ bottom mirror by the DBR decreases the light absorption losses. The fabrication process development became a challenge, since the pn-diodes had to be produced in thin silicon membranes with the thickness in the order of μm. In order to be able to control the thickness of the membranes, the MCLEDs were fabricated on 4 inch SOI (silicon on insulator) wafers with a 2 μm thick silicon device layer on the top of the buried oxide. The critical point was the high thickness variation of the silicon device layer of ±25% over the wafer. This fact led to the decision to design and to tune the device for a 4λ cavity corresponding to a Si device layer thickness of about d = 1300 nm, which is a good compromise between the optical properties and the mechanical stability of the MCLED. The final device analysed and described in this work has a thickness of the emitting silicon layer of 1751 nm, which corresponds to a 5.5λ cavity with the resonance maximum at 1146 nm. As a reference an LED fabricated on a 1620 nm thick device layer of the SOI substrate without DBRs was used. Due to the small thickness of the active silicon device layer and its relatively high refractive index, compared to the surrounding media (air and 200 nm buried oxide), this device already behaves as a 5λ Fabry-Perot resonator with the resonant wavelength at 1148 nm. Further, using the theory from Chapter 2 the comparison of calculations with measured reflectance and electroluminescence spectra of both devices was made. The structures (thicknesses of all layers) of the LED on SOI and of the MCLED were determined using the ellipsometry, TEM and FTIR.

- The calculations of the reflectance fit well with the measurements in both cases.
- It was experimentally observed that in the planar diode design, with p^+- and n^+-contacts on the top, the current mainly flows parallel to the surface along the shortest path between the p^+ and n^+ areas placed around the pn-junction. For this reason the recombination takes place preferentially at the boundary of the pn-junction and not at the bottom in the pn-junction depth of 950 nm. To simulate the electroluminescence of the devices with the used planar design was complicated and certain simplifications had to be made. In the calculation only laterally homogeneous structures without thickness variation, surface roughness or inhomogeneities can be assumed. The absorption index κ of all materials was set to zero. Best agreement between the measured and the calculated extracted EL spectra was obtained, when the emitting zone with a thickness of 375 nm was placed into an antinode of the electric field amplitude.
- The shape of the simulated EL spectrum of the LED on SOI fits well with the measured results.
- The experimentally obtained positions of the 5λ, 5.5λ and 6λ resonant peaks of MCLED in the EL spectra are in a good agreement with calculation results. However, the measured 5.5λ resonant peak is 8 times broader as expected from the simulation. The main reason is the large light collection angle of the microscope in the experimental setup, which was $\pm 25°$. This was proven by additional angular measurements of the EL.
- From the direct comparison of the measured EL spectra of the LED on SOI and MCLED the following conclusions can be drawn : 1) At the resonant wavelength 1146 nm the emission spectrum of the MCLED is enhanced by a factor of 2.6. 2) the resonant peak width is 4 times smaller than in the case of LED on SOI and 14 times smaller compared to the simple LED on a bulk silicon material (FWHM = 110 nm). 3) The quality factor of the MCLED is $Q = 144$, which is 14 times higher compared to the simple Si-LED. 4) The spectral emission enhancement of MCLED integrated over the wavelength and measured perpendicular to the diode surface is 2.24 and 1.6 times higher compared to the simple Si-LED and LED on SOI, respectively.
- The calculated extracted efficiency of a simple Si-LED is about 3%. Already the approach of LED on SOI increases the extracted efficiency to the value of 4%. The highest extracted efficiency of about 5% was obtained for the investigated MCLED.

5.2 Outlook

A proof-of-principle of an electrically driven Si microcavity LED was demonstrated. Two different Si based MCLED devices have been fabricated and characterized. High absorption losses of the MCLED with a bottom metallic $CoSi_2$ mirror and one top DBR were decreased by using the MCLED designed with two DBRs. However, several possibilities for a further improvement of the extracted light efficiency can be envisioned:

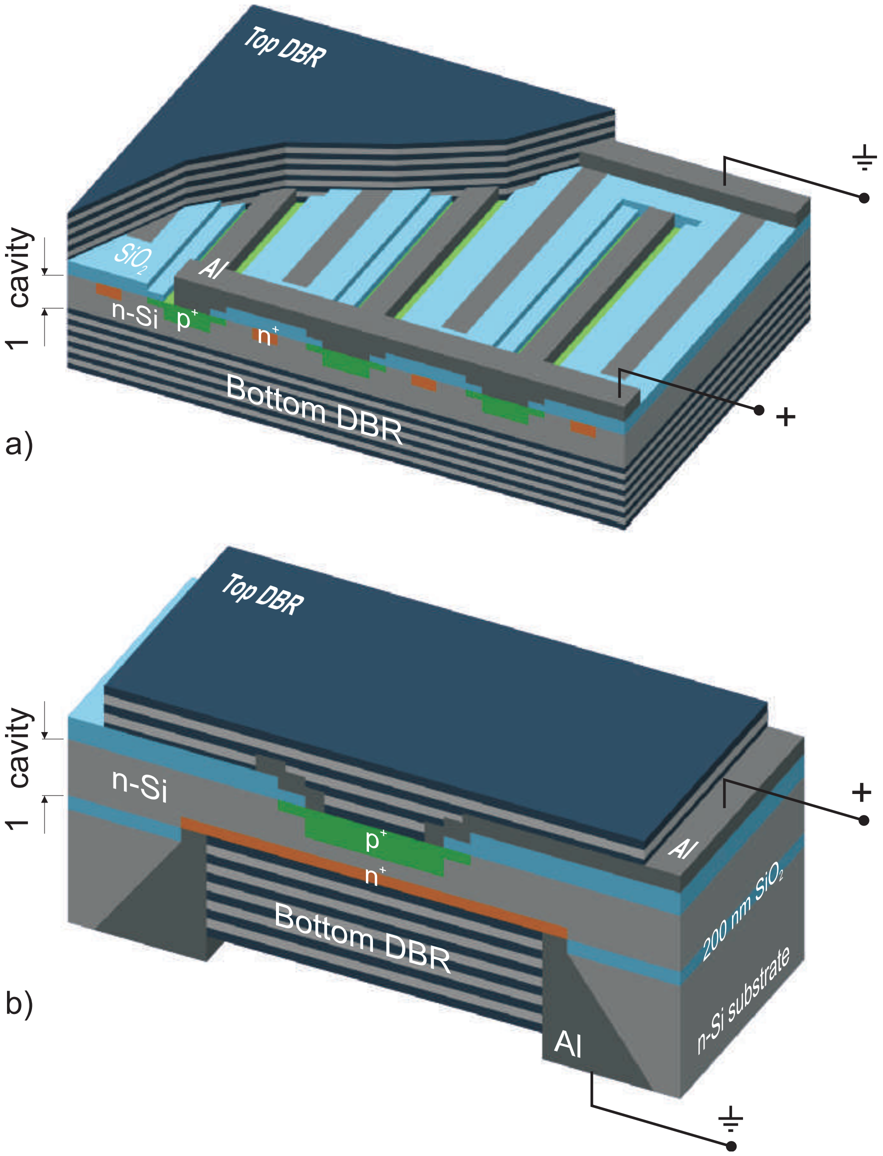

Figure 5.1: a) Interdigital structure of the laterally (horizontally) contacted MCLED. b) Vertically contacted MCLED.

- The cavity length should be as short as possible, which maximizes the integrated intensity. In the case of the Si-MCLED the use of 1λ cavity would be ideal ($L_{cav} = 325$ nm for $\lambda_{res} = 1150$ nm).

- Because of the broad boron profile with a pn-junction depth of 950 nm and because of the planar diode design (with p^+- and n^+-contacts on the front side), the light emitting region is spread across the microcavity active layer and therefore the coupling of the light emission into the microcavity mode is achieved for more than one antinode. However, placing the pn-junction exactly into one antinode of the electric field amplitude would enhance the EL intensity by the factor of two compared to the broad active region smeared out over many periods of the standing optical wave. This can be achieved by low energy boron implantation (ion energy 1 keV) and subsequent rapid thermal annealing after the B^+ implantation which can significantly reduce the pn-junction depth.

- By using Si_3N_4/SiO_2 DBRs, having a smaller refractive index contrast, a more accurate fine tuning of the reflectivities could be achieved (but more layers are needed).

- An improvement of the electrical properties of the MCLEDs can be expected to reduce the stress in the multilayer stacks deposited on both sides of the silicon membrane (e.g. CVD deposition of Si_3N_4/SiO_2).

- In order to increase the extracted light efficiency per area the proposed solution is the use of an interdigital structure with multiple pn-MCLEDs (see Fig. 5.1a). As already discussed above, the recombination of the laterally contacted MCLED (p^+- and n^+-contacts on the top of the device) takes place preferentially at the boundaries of the pn-junction and not at the flat bottom of the pn-junction. It would be advantageous to shrink the size of the devices in x-dimension and to keep it long in y-dimension.

- Another solution could be a vertically contacted MCLED with p^+-contact on the top and n^+-contact on the bottom of the active device layer - membrane (Fig. 5.1b). In this approach a shallow phosphorous or arsenic implantation had to be done at the bottom of the silicon membrane (n^+-contact). After the metallisation windows up to the device layer have to be opened by anisotropic RIE etching and the multilayered DBR stack has to be deposited on the back side of the device layer.

- In the future, a better confinement could be achieved by lateral patterning of the active layer of the MC into a 2D or 3D photonic crystal structures.

Appendix A

A.1 The parametrization of optical constants

A.1.1 Kramers-Kronig relations

Real and imaginary part of the complex index of refraction $\tilde{n} = n + ik$ (n: refractive index, k: extinction coefficient) are not independent quantities, the same holds for real and imaginary parts of the complex dielectric function $\tilde{\epsilon} = \epsilon_1 + i\epsilon_2 (\epsilon_1 = n^2 - k^2, \epsilon_2 = 2nk)$. The Kramers-Kronig relation, resulting from the requirement that a material cannot respond to an electric field prior to its application, connects the real and imaginary parts of the complex dielectric function $\tilde{\epsilon} = \epsilon_1 + i\epsilon_2$ as follows:

$$\epsilon_1(E) = 1 + \frac{2}{\pi} P \int_0^{\infty} \frac{E' \cdot \epsilon_2(E')}{E'^2 - E^2} dE' \tag{A.1}$$

Here E is the energy of light and P is the Cauchy principal value of the integral taken at E = E'. In the analysis of optical constants parameterized dispersion formulas are employed. Many of them comply with the Kramers-Kronig relations. This is achieved by choosing a particular function to describe either the real or the imaginary part of the optical constants, and calculating the other part from the Kramers-Kronig relations. Parameterizations used for the optical constants of Si and SiO_2 are relevant for the present work and briefly discussed below.

A.1.2 Forouhi-Bloomer dispersion formula

A model proposed by Forouhi and Bloomer (F-B) has been applied successfully to describe the dispersion of amorphous dielectrics and amorphous semiconductors, in particular amorphous Ge and Si. From a derived expression for the extinction coefficient, the refractive index is obtained by Kramers- Kronig integration. The F-B equations are:

$$k(E) = \sum_{i}^{q} \frac{A_i (E - E_g)^2}{E^2 - B_i E + C_i} \tag{A.2}$$

$$n(E) = n(\infty) + \sum_{i=1}^{q} \frac{B_{0i} E + C_{0i}}{E^2 - B_i E + C_i} \tag{A.3}$$

$$B_{0i} = \frac{A_i}{Q_i} \left(-\frac{B_i^2}{2} + E_g B_i - E_g^2 + C_i\right) \tag{A.4}$$

$$C_{0i} = \frac{A_i}{Q_i} \left((E_g + C_i) \frac{B_i}{2} - 2 E_g C_i\right) \tag{A.5}$$

$$Q_i = \frac{1}{2}(4C_i - B_i^2)^{1/2} \tag{A.6}$$

where E$_g$ represents the optical energy band-gap, B$_i$/2 is equal to the ith term (peak) energy, A$_i$ and C$_i$ denote amplitude and broadening terms (all in units of eV). A characteristic feature of the F-B equations is their simplicity.

A.1.3 Tauc-Lorentz dispersion formula

Jellison and Modine presented a Kramers-Kronig consistent parameterization for the optical functions of amorphous semiconductors and insulators in the interband region [90, 91]. Based on experimental results, the authors consider their more sophisticated model to be superior to the F-B-model. The model is formulated as follows:

$$\epsilon_2(E) = \begin{cases} 2nk = \frac{AE_0C(E-E_g)^2}{(E^2-E_0^2)^2+C^2E^2} \cdot \frac{1}{E}, & E > E_g \\ 0, & E \leq E_g \end{cases} \tag{A.7}$$

$$\begin{aligned} \epsilon_1 = \epsilon_1(\infty) &+ \frac{AC}{\pi\zeta^4} \cdot \frac{\alpha_{ln}}{2\alpha E_0} ln\left(\frac{E_0^2 + E_g^2 + \alpha E_g}{E_0^2 + E_g^2 - \alpha E_g}\right) \\ &- \frac{A}{\pi\zeta^4} \cdot \frac{a_{atan}}{E_0}\left[\pi - atan\left(\frac{2.E_g + \alpha}{C}\right) + atan\left(\frac{-2.E_g + \alpha}{C}\right)\right] \\ &+ 2 \cdot \frac{AE_0}{\pi\zeta^4\alpha} \cdot E_g \cdot (E^2 - \gamma^2) \cdot \left[\pi + 2 \cdot atan\left(2 \cdot \frac{\gamma^2 - E_g^2}{\alpha C}\right)\right] \\ &- \frac{AE_0C}{\pi\zeta^4} \cdot \frac{E^2 + E_g^2}{E} \cdot ln\left(\frac{|E - E_g|}{E + E_g}\right) \\ &+ 2 \cdot \frac{AE_0C}{\pi\zeta^4} \cdot E_g \cdot ln\left[\frac{|E - E_g|.(E + E_g)}{\sqrt{(E_0^2 - E_g^2)^2 + E_g^2.C^2}}\right] \end{aligned} \tag{A.8}$$

$$\alpha_{ln} = (E_g^2 - E_0^2)E^2 + E_g^2C^2 - E_0^2(E_0^2 + 3E_g^2) \tag{A.9}$$

$$\alpha_{atan} = (E^2 - E_0^2)(E_0^2 - E_g^2] + E_g^2C^2 \tag{A.10}$$

$$\zeta^4 = (E^2 - \gamma^2)^2 + \frac{\alpha^2C^2}{4} \tag{A.11}$$

$$\alpha = \sqrt{4E_0^2 - C^2} \tag{A.12}$$

$$\gamma = \sqrt{E_0^2 - C^2/2} \tag{A.13}$$

The fit parameters A,E$_0$,C and E$_g$ denoting amplitude, energy and broadening of the main optical transition and the band gap energy respectively are all in units of energy (eV).

A.1.4 Sellmeier dispersion formula

The Sellmeier dispersion formula is used to parameterize the optical constants of transparent dielectrics in the region of normal dispersion. The model reflects the response of isotropic and uniformly distributed identical charged harmonic oscillators to the excitation by a plane electro-magnetic light wave. Far from the resonance, the absorption is small and the oscillators affect mainly the real part of the dielectric function ϵ_1:

$$\epsilon_1 = n^2 = 1 + \sum_{j=1}^{M} A_j \frac{\lambda^2 \lambda_j^2}{\lambda^2 - \lambda_j^2} \tag{A.14}$$

In the visible spectral region, typical values for SiO_2 are M=1, $A_1 = 0.000126$ nm^{-2} and $\lambda_1 = 93.4$ nm.

A.2 Wafer holder

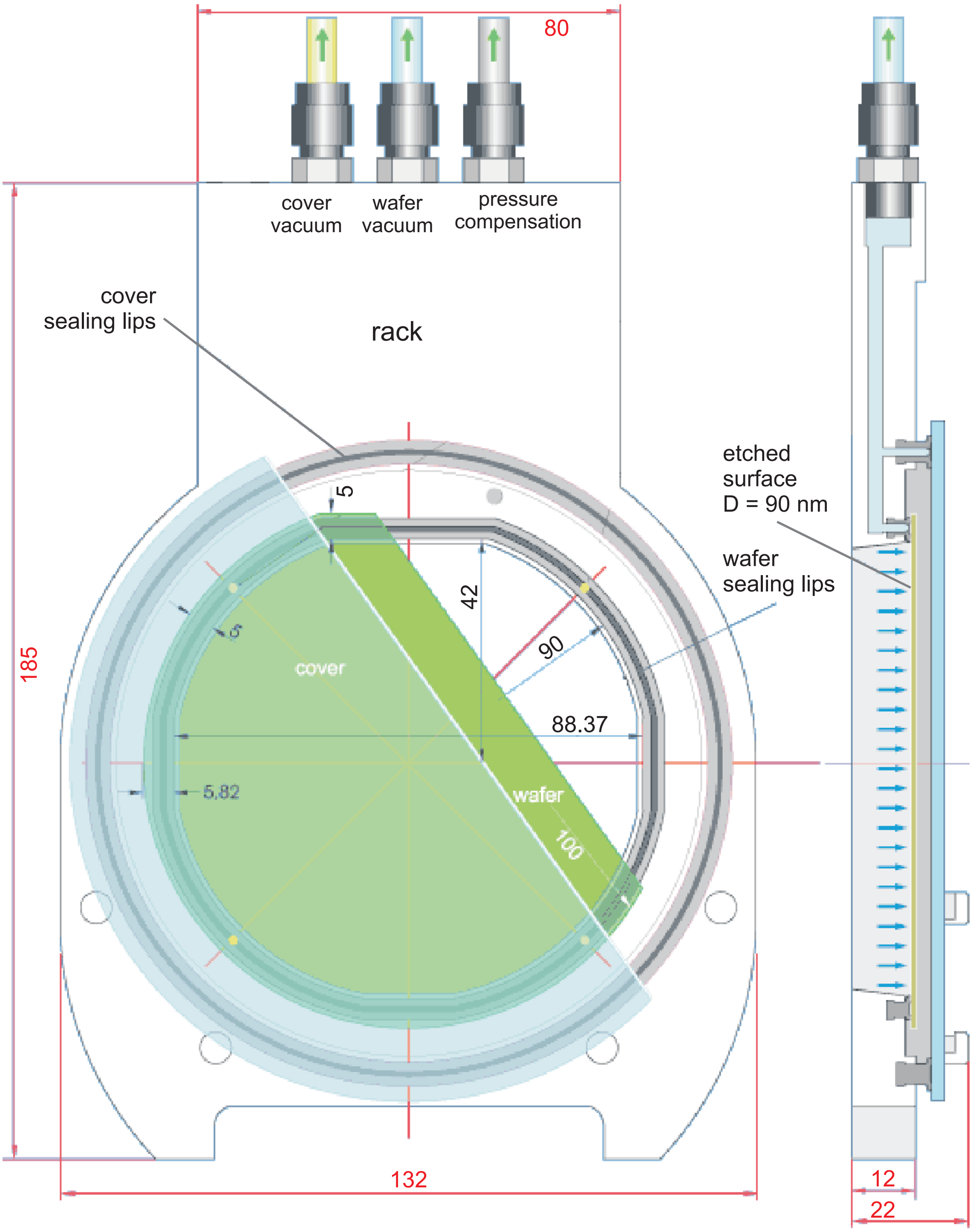

Figure A.1: waferholder

Bibliography

[1] J. M. Sun, T. Dekorsy, W. Skorupa, B. Schmidt, and M. Helm, Appl. Phys. Lett. **83**, 3885 (2003).

[2] L. Canham, Nature **408**, 411 (2000).

[3] V. Kveder, E. Steinman, S. Shevchenko, and H. Grimmeiss, Phys. Rev. B **51**, 10520 (1995).

[4] M. A. Green, J. Zhao, A. Wang, P. J. Reece, and M. Gal, Nature **412**, 805 (2001).

[5] W. Ng, M. Lourenco, R. Gwilliam, S. Ledain, G. Shao, and K. Homewood, Nature **410**, 192 (2001).

[6] E. F. Schubert, *Light-Emitting Diodes* (Cambridge University Press, Cambridge, UK 2003).

[7] H. Benisty, H. D. Neve, and C. Weisbuch, IEEE J. Quantum Electron. **34**, 1612 (1998).

[8] D. Sotta, E. Hadji, N. Magnea, and E. Delamadeleine, Journal of Applied Physics **92**, 2207 (2002).

[9] F. Iacona, G. Franzò, E. C. Moreira, and F. Priolo, Journal of Applied Physics **89**, 8354 (2001).

[10] M. Araki, H. Koyama, and N. Koshida, Appl. Phys. Lett. **69**, 2956 (1996).

[11] S. Chan and P. Fauchet, Appl. Phys. Lett. **75**, 274 (1999).

[12] M. Zelsmann, E. Picard, T. Charvolin, E. Hadji, M. Heitzmann, B. Dal'zotto, M. E. Nier, C. Seassal, P. Rojo-Romeo, and X. Letartre, Appl. Phys. Lett. **83**, 2542 (2003).

[13] M. E. Kurdi, S. David, P. Boucaud, C. Kammerer, X. Li, V. L. Thanh, S. Sauvage, and J. M. Lourtioz, J. Appl. Phys **96**, 997 (2004).

[14] C. D. Presti, A. Irrera, G. Franzò, I. Crupi, F. Priolo, F. Iacona, G. Di Stefano, A. Piana, D. Sanfilippo, and P. G. Fallica, Appl. Phys. Lett. **88**, 1 (2006).

[15] N. E. J. Hunt, E. Schubert, R. Logan, and G. J. Zydzik, Appl. Phys. Lett. **61**, 2287 (1992).

[16] S. Ossicini, L. Pavesi, and F. Priolo, in *Light Emitting Silicon for Microphotonics* (Springer 2004).

[17] L. Pavesi and D. J. Loakwood, in *Silicon Photonics* (Springer 2004).

[18] M. S. Tyagi, in *Introduction to Semiconductor Materials and Devices* (John Wiley & Sons 1991), Kap. Light emitting diodes.

[19] J. H. Round, Electrical World **49**, 309 (1907).

[20] O. V. Losev, Telegrafi ya i Telefoniya bez Provodov **44**, 485 (1928).

[21] O. V. Losev, Phil. Mag. **6**, 1024 (1928).

[22] O. V. Losev, Physik. Zeitschr. **30**, 920 (1930).

[23] N. Zheludev, Nature Photonics **1**, 189 (2007).

[24] R. Braunstein, Physical Review **99**, 1892 (1955).

[25] J. R. Biard, E. L. Bonin, W. N. Carr, and G. E. Pittman, PGED Electron Device Conference (1962).

[26] The Quartz Watch, http://invention.smithsonian.org/centerpieces/quartz/inventors/biard.html, 2008.

[27] Massachusetts Institute of Technology, http://web.mit.edu/invent/a-winners/a-holonyak.html, 2004.

[28] J. R. Haynes and H. B. Briggs, Physical Review **86**, 647 (1952).

[29] J. I. Pankove, J. E. Berkeyheiser, H. P. Maruska, and J. Wittke, Solid State Communications **8**, 1051 (1970).

[30] H. P. Maruska, W. C. Rhines, and D. A. Stevenson, Materials Research Bulletin **7**, 777 (1972).

[31] S. Nakamura, Microelectronics Journal **25**, 651 (1994).

[32] S. Nakamura, Journal of Crystal Growth **145**, 911 (1994).

[33] S. Nakamura, Diamond and Related Materials **5**, 496 (1996).

[34] S. Nakamura, Materials Science and Engineering B **43**, 258 (1996).

[35] S. Nakamura and G. Fasol, in *The blue laser diode* (Springer, Berlin 1997).

[36] S. Nakamura, M. Senoh, S. ichi Nagahama, N. Iwasa, T. Yamada, T. Matsushita, H. Kiyoku, Y. Sugimoto, T. Kozaki, H. Umemoto, M. Sano, and K. Chocho, Journal of Crystal Growth **189–190**, 820 (1998).

[37] R. N. Hall, Phys. Rev. **87**, 387 (1952).

[38] W. Shockley and W. T. Read, Phys. Rev. **87**, 835 (1952).

[39] C. W. Wilmsen, H. Temkin, and L. A. Coldren, in *Vertical-Cavity Surface-Emitting Lasers: Design, Fabrication, Characterization, and Applications* (Cambridge University Press 2001).

[40] I. Schnitzer, E. Yablonovitch, C. Caneau, and T. J. Gmitter, Applied Physics Letters **62**, 131 (1992).

[41] H. Benisty, J.-M. Gerard, R. Houdre, J. Rarity, and C. Weisbich, *Confined Photon systems. Fundamentals and applications, lecture notes of QED phenomena and applications of microcavities and photonic crystals, 1998, Cargese, Corsica, France, Lecture Notes in Physics* (Springer Berlin 1999), Kap. Physics of Light Extraction Efficiency in Planar Microcavity Light-Emitting Diodes.

[42] I. Schnitzer, E. Yablonovitch, C. Caneau, T. J. Gmitter, and A. Scherer, Applied Physics Letters **63**, 2174 (1993).

[43] G. Davies, Physics Reports **176**, 83 (1989).

[44] X. yuan Hou, H. lei Fan, L. Xu, F. long Zhang, M. qian Li, M. ren Yu, and X. Wang, Applied Physics Letters **68**, 2323 (1996).

[45] D. C. Bensahel, L. T. Canham, and B. Bensahel, in *Optical Properties of Low Dimensional Silicon Structures* (Kluwer, Dordrecht 1993).

[46] P. M. Fauchet, C. C. Tsai, L. T. Canham, I. Shimizu, and Y. Aoyagi, in *Microcrystalline Semiconductors: Materials Science and Devices* (Materials Research Society, Pittsburgh 1993).

[47] D. J. Lockwood, Solid State Communications **92**, 101 (1994).

[48] Z. C. Feng and R. Tsu, in *Porous Silicon* (Materials scientists, Singapore 1994).

[49] L. Canham, in *Properties of Porous Silicon* (Institution of Engineering and Technology 1997).

[50] M. V. Wolkin, J. Jorne, P. M. Fauchet, G. Allan, and C. Delerue, Phys. Rev. Lett. **82**, 197 (1999).

[51] H. Mizuno, H. Koyama, and N. Koshida, Applied Physics Letters **69**, 3779 (1996).

[52] G. Polisski, H. Heckler, D. Kovalev, M. Schwartzkopff, and F. Koch, Applied Physics Letters **73**, 1107 (1998).

[53] A. Richter, P. Steiner, F. Kozlowski, and W. Lang, Electron Device Letters, IEEE **12**, 691 (1991).

[54] B. Gelloz and N. Koshida, Journal of Applied Physics **88**, 4319 (2000).

[55] S. Chan and P. M. Fauchet, Optical Materials **17**, 31 (2001).

[56] A. Irrera, D. Pacifici, M. Miritello, G. Franzo, F. Priolo, F. Iacona, D. Sanfilippo, G. D. Stefano, and P. G. Fallica, Physica E: Low-dimensional Systems and Nanostructures **16**, 395 (2003).

[57] L. Pavesi, L. Dal Negro, C. Mazzoleni, G. Franzò, and F. Priolo, Nature **408**, 440 (2000).

[58] L. D. Negro, M. Cazzanelli, N. Daldosso, Z. Gaburro, L. Pavesi, F. Priolo, D. Pacifici, G. Franzo, and F. Iacona, Physica E: Low-dimensional Systems and Nanostructures **16**, 297 (2003).

[59] L. D. Negro, M. Cazzanelli, L. Pavesi, S. Ossicini, D. Pacifici, G. Franzò, F. Priolo, and F. Iacona, Applied Physics Letters **82**, 4636 (2003).

[60] L. Khriachtchev, M. Räsänen, S. Novikov, and J. Sinkkonen, Applied Physics Letters **79**, 1249 (2001).

[61] M. H. Nayfeh, S. Rao, N. Barry, J. Therrien, G. Belomoin, A. Smith, and S. Chaieb, Applied Physics Letters **80**, 121 (2002).

[62] J. Ruan, P. M. Fauchet, L. Dal Negro, M. Cazzanelli, and L. Pavesi, Appl. Phys. Lett. **83**, 5479 (2002).

[63] K. Luterova, K. Dohnalova, V. Svrcek, I. Pelant, J.-P. Likforman, O. Cregut, P. Gilliot, and B. Honerlage, Applied Physics Letters **84**, 3280 (2004).

[64] L. Khriachtchev, M. Rasanen, and S. Novikov, Applied Physics Letters **83**, 3018 (2003).

[65] J. Valenta, I. Pelant, and J. Linnros, Applied Physics Letters **81**, 1396 (2002).

[66] M. E. Castagna, S. Coffa, M. Monaco, A. Muscara, L. Caristia, S. Lorenti, and A. Messina, Mater. Sci. Eng. B **105**, 83 (2003).

[67] S. Wang, S. Coffa, R. Carius, and C. Buchal, Materials Science and Engineering B **81**, 102 (2001).

[68] L. Rebohle, T. Gebel, R. Yankov, T. Trautmann, W. Skorupa, J. Sun, G. Gauglitz, and R. Frank, Optical Materials **27**, 1055 (2005).

[69] J. Sun, W. Skorupa, T. Dekorsy, M. Helm, L. Rebohle, and T. Gebel, J. Appl. Phys. **97**, 123513 (2005).

[70] J. Sun, W. Skorupa, T. Dekorsy, M. Helm, L. Rebohle, and T. Gebel, Appl. Phys. Lett. **85**, 3387 (2004).

[71] J. Sun, S. Prucnal, W. Skorupa, T. Dekorsy, M. Helm, L. Rebohle, and T. Gebel, Appl. Phys. Lett. **89**, 091908 (2006).

[72] S. Prucnal, J. M. Sun, W. Skorupa, and M. Helm, Applied Physics Letters **90**, 181121 (2007).

[73] G. Franzo, F. Iacona, V. Vinciguerra, and F. Priolo, Materials Science and Engineering B **69–70**, 335 (2000).

[74] J. M. A. Podhorodecki and, J. Wojcik, E. Irving, and P. Mascher, Journal of Luminescence **121**, 230 (2006).

[75] A. Irrera, G. Franzo, F. Iacona, A. Canino, G. D. Stefano, D. Sanfilippo, A. Piana, P. Fallica, and F. Priolo, Physica E: Low-dimensional Systems and Nanostructures **38**, 181 (2007).

[76] D. Pacifici, A. Irrera, G. Franzo, M. Miritello, F. Iacona, and F. Priolo, Physica E: Low-dimensional Systems and Nanostructures **16**, 331 (2003).

[77] M. Zacharias, J. Heitmann, M. Schmidt, and P. Streitenberge, Physica E: Low-dimensional Systems and Nanostructures **11**, 245 (2001).

[78] P. G. Kik and A. Polman, Materials Science and Engineering B **81**, 3 (2001).

[79] G. Franzo, E. C. Moreira, D. Pacifici, F. Priolo, F. Iacona, and C. Spinella, Nuclear Instruments and Methods in Physics Research Section B: Beam Interactions with Materials and Atoms **175–177**, 140 (2001).

[80] W. Wang, H. Isshiki, S. Yugo, R. Saito, and T. Kimura, Journal of Luminescence **87–89**, 319 (2000).

[81] S. Coffa, IEEE Spectrum 36 (2005).

[82] M. Paniccia and S. Koehl, IEEE Spectrum 30 (2005).

[83] H. Rong, R. Jones, A. Liu, O. Cohen, D. Hak, A. Fang, and M. Paniccia, Letterrs to Nature **433**, 725 (2005).

[84] P. K. Basu, Resonance **12**, 37 (2007).

[85] N.A.Sobolev, A.M.Emelyanov, E.I.Shek, and V.I.Vdovin, Solid State Phenomena **95-96**, 283 (2004).

[86] G. Pan, R. Ostroumov, Y. Lian, K. Tu, and K. Wang, .

[87] M. Kittler, T. Arguirov, A. Fischer, and W. Seifert, Optical Materials **27**, 976 (2005).

[88] E. O. Sveinbjörnsson and J. Weber, Applied Physics Letters **69**, 2686 (1996).

[89] J. M. Sun, T. Dekorsy, W. Skorupa, B. Schmidt, A. Mücklich, and M. Helm, Phys. Rev. B **70**, 1 (2003).

[90] J. M. Sun, T. Dekorsy, W. Skorupa, B. Schmidt, and M. Helm, Appl. Phys. Lett. **82**, 2823 (2003).

[91] E. F. Schubert, Y.-H. Wang, A. Y. Cho, L.-W. Tu, and G. J. Zydzik, Applied Physics Letters **60**, 921 (1992).

[92] L. W. Tu, Appl. Phys. Lett. **57**, 2045 (1990).

[93] G. M. Smith, D. V. Frobes, J. J. Coleman, and J. T. Verdeyen, IEEE Photonics Technology Lett. **5**, 873 (1993).

[94] S. L. McCall, A. F. J. Levi, R. E. Slusher, S. J. Pearton, and R. A. Logan, Appl. Phys. Lett. **60**, 289 (1992).

[95] E. D. Palik, in *Handbook of optical constants of solids* (Academic Press Inc.,U.S. 1985), Vol. 1.

[96] L. A. Coldren and S. W. Corzime, *Diode lasers and photonic integreted circuits* (John Wiley & sons, New York 1995).

[97] Y. A., *Quantum electronics* (John Wiel and Sons, New York 1989).

[98] G. Björk, Y. Yamamoto, and H. Heitmann, in *Confined electrons and photons* (E. Burstein and C. Weisbuch, Plenum Press, New York 1995), Kap. Spontaneous emission control in semiconductor microcavities.

[99] C. Vinegoni, M. Cazanelli, and L. Pavesi, in *Silicon-Based Materials and Devices* (Elsevier Science & Technology 2001), Kap. Porous Silicon Microcavities.

[100] S. J. and S. L.W., Electronic Letters **23**, 781 (1987).

[101] A. Yariv, in *Introduction to Theory and Applications of Quantum Mechanics* (John Wiley & Sons, Inc. 1982), p. 143.

[102] A. M. Vredenberg, N. E. J. Hunt, E. F. Schubert, D. C. Jacobson, J. M. Poate, and G. J. Zydzik, Phys. Rev. Lett. **71**, 517 (1993).

[103] N. E. J. Hunt, E. F. Schubert, R. F. Kopf, D. L. Sivco, A. Y. Cho, and G. J. Zydzik, Applied Physics Letters **63**, 2600 (1993).

[104] E. F. Schubert, N. E. J. Hunt, M. Micovic, R. J. Malik, D. L. Sivco, A. Y. Cho, and G. J. Zydzik, Science **265**, 943 (1994).

[105] E. F. Schubert, N. E. J. Hunt, R. J. Malik, M. Micovic, and D. Miller, Journal of Lightwave Technology **14**, 1721 (1996).

[106] A. Kastler, Nouvelle Revue d'Optique **5**, 133 (1974).

[107] UniCAD, Inc., *UniMCO 4.0 User Manual - The unique CAD tool for LED, OLED, RCLED, VCSEL & optical coating*, 2002-2005.

[108] International Technology Roadmap for Semiconductors, http://public.itrs.net/, 2005.

[109] T. Watanabe, K. Tatsumura, and I. Ohdomari, Phys. Rev. Lett. **96**, (2006).

[110] S. Wolf and R. N. Tauber, in *Silicon Processing for the VLSI Era, Vol. 1: Process Technology* (Lattice Press 2000), Kap. Thermal oxidation of silicon.

[111] B. E. Deal and A. S. Grove, J. Appl. Phys. **36**, (1965).

[112] W. Kern, in *Handbook of Semiconductor Wafer Cleaning Technology* (Noyes Publications, New Jersey 1993), Kap. Wet Chemical Processes.

[113] Transene Company, Inc., http://www.transene.com/aluminum.html, 2008.

[114] L. Fuller, http://www.rit.edu/lffeee, 2008.

[115] Siliconfareast, http://www.siliconfareast.com/wetetch.htm.

[116] A. Heuberger, *Mikromechanik: Mikrofertigung mit Methoden der Halbleitertechnologie* (Springer 1994).

[117] R. A. Barker, T. M. Mayer, and W. C. Pearson, J. Vac. Sci. Technol. B **1**, 37 (1983).

[118] C. Cardinaud, M. C. Peignon, and P. Y. Tessier, Applied Surface Science **164**, 72 (2000).

[119] G. Dang, H. Cho, K. P. Ip, S. J. Pearton, S. N. G. Chu, J. Lopata, W. S. Hobson, L. M. F. Chirovsky, and F. Rena, Journal of The Electrochemical Society **148**, G25 (2001).

[120] S. A. Furman and A. V. Tikhonravov, in *Basics of Optics of Multilayer Systems* (Editions Frontieres, Gif-sur-Yvette, France 1992), Kap. Spectral charcteristics of multilayer coatings: Theory.

[121] E. Gogolides, P. Vauvert, G. Kokkoris, G. Turban, and A. G. Boudouvis, Journal of Applied Physics **88**, 5570 (2000).

[122] D. C. Gray, I. Tepermeister, and H. H. Sawin, J. Vac. Sci. Technol. B **11**, 1243 (1993).

[123] S. M. Rossnagel, J. J. Cuomo, and W. D. Westwood, in *Handbook of Plasma Processing Technology - Fundamentals, Etching, Deposition, and Surface Interactions.* (William Andrew Publishing, Noyes 1995).

[124] B. E. E. Kastenmeier, P. J. Matsuo, G. S. Oehrlein, and J. G. Langan, J. Vac. Sci. Technol. A **16**, 2047 (1998).

[125] M. T. Kim, Journal of The Electrochemical Society **147**, 1204 (2000).

[126] C. Reyes-Betanzo, S. A. Moshkalyov, J. W. Swart, and A. C. S. Ramos, J. Vac. Sci. Technol. A **21**, 461 (2003).

[127] S. Tachi, K. Miyake, and T. Tokuyama, Japanese Journal of Applied Physics **20**, L411 (1981).

[128] S. Tachi, K. Tsujimoto, S. Arai, and T. Kure, J. Vac. Sci. Technol. A **9**, 796 (1991).

[129] Y. Y. Tu, T. J. Chuang, and H. F. Winters, Physical Review B **23**, 823 (1981).

[130] E. Zawaideh and N. S. Kim, Journal of Applied Physics **62**, 2498 (1987).

[131] E. Zawaideh and N. S. Kim, Journal of Applied Physics **64**, 4199 (1988).

[132] B. El-Kareh, in *Fundamentals of semiconductor processing technologies* (Springer 1995), Kap. Wet etching.

[133] K. Seshan, *Handbook of Thin Film Deposition* (Noyes Publication, William Andrew Publishing 2002).

[134] D. M. Dobkin and M. K. Zuraw, *Principles of Chemical Vapor Deposition: What's Going on Inside the Reactor* (Kluwer Academic 2003).

[135] D. L. Smith, *Thin-Film Deposition: Principles And Practice* (Mcgraw-Hill Education 1995).

[136] J. S. Chapin, Sputtering process and apparatus, United States Patent 4166018, 1979.

[137] J. A. Thorton and A. Penford, in *Thin Film Processes* (J.L. Vossen and W. Kern, Academic Press, New York 1978), pp. 75–113.

[138] W.Theiss, *Scout user manual - Spectrum interpretation by simulation*, 2001.

[139] B. Aspar, M. Bruel, H. Moriceau, C. Maleville, T. Poumeyrol, A. M. Papon, A. Claverie, G. Benassayag, A. J. Auberton-Hervé, and T. Barge, Microelectronic Engineering **36**, 233 (1997).

[140] A. J. A. Herve, Electron Devices Meeting 3 (1996).

[141] G. Celler and M. Wolf, Soitec (2003).

[142] P. D. Davidse and L. I. Maissel, J. Appl. Phys. **37**, 574 (1966).

[143] J. U. Schmidt, PhD Thesis, TU Dresden, Dresden, 2004.

[144] C. V. Macchioni, J. Vac. Sci. Technol. A **8**, 1340 (1990).

[145] C. V. Macchioni, J. Vac. Sci. Technol. A **8**, 2302 (1991).

[146] S. Suyama, A. Okamoto, and T. Serikawa, J. Electrochem. Soc. **134**, 2260 (1987).

[147] E. V. Jelenkovic and K. Y. Tong, Microelectronics Reliability **37**, 159 (1997).

[148] H. Seifarth, Personal communication, 2007.

[149] R. A. Devine, J. P. Duraud, and E. Dooryhée, in *Structure and Imperfections in Amorphous and Crystalline Silicon Dioxide* (John Wiley & Sons 2000).

[150] K. E. Oughstun and N. A. Cartwright, Optics Express **11**, 1541 (2003).

[151] I. P. Lisovskii, V. G. Litovchenko, V. G. Lozinskii, and G. I. Steblovskii, Thin Solid Films **213**, 164 (1992).

[152] I. P. Lisovskii, V. G. Litovchenko, V. B. Lozinskii, S. I. Frolov, H. Flietner, W. Fussel, and E. G. Schmidt, Journal of Non-Crystalline Solids **187**, 91 (1995).

[153] K. Raghavachari, D. Ricci, and G. Pacchioni, J. Chem. Phys. **116**, 825 (2002).

[154] T. Tamura, G.-H. Lu, R. Yamamoto, and M. Kohyama, Phys. Rev. B **69**, 1 (2004).

[155] S. Munekuni, T. Yamanaka, Y. Shimogaichi, R. Tohmon, Y. Ohki, K. Nagasawa, and Y. Hama, J. Appl. Phys. **68**, 1212 (1990).

[156] R. Renoud, F. Papin, J.-P. Ganachaud, and J. Bigarré, Physica status solidi (a) **203**, 591 (2006).

[157] L. N. Skuja, A. N. Streletsky, and A. B. Pakovich, Solid State Communications **50**, 1069 (1984).

[158] Y. Tatsumi and H. Ohsaki, in *Properties of amorphous silicon* (INSPEC, London and New York 1989), Kap. Density of c-Si, a-Si and a-Si:H.

[159] P. Barbieri, M. de Oliveira, A. Champia, and F. Marquesa, Journal of Non-Crystalline Solids **352**, 1016 (2006).

[160] M. Langen, T. Hibiya, M. Eguchi, and I. Egry, J. Cryst. Growth **186**, 550 (1998).

[161] G. E. Jellison and F. A. Modine, Appl. Phys. Lett. **69**, 371 (1996).

[162] G. E. Jellison, V. I. Merkulov, A. A. Puretzky, D. B. Geohegan, G. Eres, D. H. Lowndes, and J. B. Caughman, Thin Solid Films **377-378**, 68 (2000).

[163] S. Mantl, Mater. Sci. Rep. **8**, 1 (1992).

[164] SILICET AG, http://www.silicet.de, 2009.

[165] U. of Reading, Temperature-dependent refractive index dispersion profile for Silicon, www.irfilters.reading.ac.uk, 2006.

[166] Blender, www.blender.org, 2009.

List of publications

Scientific articles

Silicon-on-insulator microcavity light emitting diodes with two Si/SiO$_2$ Bragg reflectors
J. Potfajova, J.M. Sun, B. Schmidt, T. Dekorsy, W. Skorupa, and M. Helm, *Journal of Luminescence*, **121**(2),290-292 (2006)

Efficient silicon based light emitters
M. Helm, J. M. Sun, J. Potfajova, S. Winnerl, T. Dekorsy, W. Skorupa, B. Schmidt, and A. Mücklich, *Microelectronics Journal*, **36**(11), 957-962 (2005)

Silicon-based electrically driven microcavity LED
J. Potfajova, J.M. Sun, S. Winnerl, T. Dekorsy, W. Skorupa, B. Schmidt, M. Helm, S. Mantl, and U. Breuer, *Electronics Letters*, **40**(14) , 904-906 (2004)

Conference contributions

Sputter deposition and characterisation of DBR systems for RCLEDs
J. Potfajova, M.Helm, B. Schmidt, T. Dekorsy, J. Sun, and V. Skorupa
Seminar of the Institute of Ion-Beam Physics and Materials Research FZD, June 2004, Schmochtitz, Germany

Resonant cavity Si-LEDs
J. Potfajova, M.Helm, B. Schmidt, T. Dekorsy, J. Sun, and V. Skorupa
Nanoved 2004, September 13-14, 2004, Kosice, Slovakia

Silicon microcavity light emitting diode
J. Potfajova, M.Helm, B. Schmidt, T. Dekorsy, J. Sun, and V. Skorupa
3rd Optoelectronic and Photonic Winter School - Optical Interconnects, 27 February 27 - March 4, 2005, Sardagna (Trento), Italy

Silicon Microcavity LEDs with CoSi$_2$ Metallic Mirrors
J. Potfajova, J.M. Sun, S. Winnerl, T. Dekorsy, W. Skorupa, B. Schmidt, M. Helm, S. Mantl, U. Breuer und M. Wiemer
E-MRS 2005 Spring Meeting, May 31 - June 3, 2005, Strasbourg, France

Si based microcavity LEDs
J. Potfajova, M.Helm, B. Schmidt, T. Dekorsy, J. Sun and V. Skorupa, S. Mantl, and U. Breuer

Seminar of the Institute of Ion-Beam Physics and Materials Research FZD, June 13-15, 2005, Schmochtitz, Germany

Resonant cavity Si light emitting diodes
J. Potfajova, M.Helm, B. Schmidt, T. Dekorsy, J. Sun and V. Skorupa, S. Mantl, and U. Breuer
International Doctoral Seminar 2006, April 23-26, 2006, Smolenice, Slovakia

Silicon-on-insulator microcavity light emitting diodes with two Si/SiO_2 Bragg reflectors
J. Potfajova, M.Helm, B. Schmidt, T. Dekorsy, J. Sun and V. Skorupa
E-MRS 2006 Spring Meeting, May 29 - June 2, 2006, Nice, France

SOI-MCLED with two Si/SiO_2 Bragg reflectors
J. Potfajova, M.Helm, B. Schmidt, T. Dekorsy, J. Sun and V. Skorupa
Seminar of the Institute of Ion-Beam Physics and Materials Research FZD, June 12-14, 2004, Schmochtitz, Germany

Silicon microcavity light emitting diodes
J. Potfajova, M.Helm, B. Schmidt, T. Dekorsy, J. Sun and V. Skorupa
Seminar of the Institute of Ion-Beam Physics and Materials Research FZD, June 11-13, 2004, Schmochtitz, Germany

Si based photonics
J.Potfajova
Doctoral Seminar, September 26-28, 2007, Rabenberg, Germany

Acknowledgements

I would like to express my gratitude to all those who have contributed to my scientific work. This dissertation would not have come into being without their support, encouragement, understanding, and patience.

- In the first row I would like to thank to Dr. Dr. h. c. Peter Joehnk the administrative director of the Forschungszentrum Dresden-Rossendorf who directed my attention to FZD.
- Many thanks to my supervisor Prof. Dr. Manfred Helm the head of Institute of Ion-Beam Physics and Materials Research. He together with Dr. Bernd Schmidt, Prof. Dr. Thomas Dekorsy and Prof. Dr. Jiaming Sun initialised this interesting topic and gave me the opportunity to commence this thesis. He always had an open door for discussions and gave valuable advice where one was about to struggle.
- I am deeply indebted to my direct advisor Dr. Bernd Schmidt whose stimulating suggestions and encouragement combined with his experiences, competence and a remarkable knowledge on current semiconductor developments and technology trends helped me during research, experiments and writing of this thesis.
- I have furthermore to thank Prof. Dr. Thomas Dekorsy and Prof. Dr. Manfred Helm for taking a role of referee.
- Especially, I am thankful to my colleague Dr. Michael Zier for the long discussions, helpful suggestions, encouragement, german and english grammar corrections, helping with the troubles with the computer hardware and software, his jokes and friendship.
- I also want to thank our FWIP team for a friendly atmosphere, wonderful relationships and daily work. Unforgotten are also our coffee break filled with discussions on daily topics but also spanning a surprisingly wide range from which I personally learned a lot.
- Especially, I would like to express my gratitude to our clean room team Gabriele Schnabel, Heike Felsmann, Claudia Neisser and Bernd Scheumann who helped me in the complicated fabrication process.
- Dr. Steffen Howitz from GeSiM - Gesellschaft für Silizium-Mikrosysteme mbH for the CVD deposition of Si_3N_4 layers.
- Prof. Dr. Siegfried Mantl from the Institute of Thin Films and Interfaces and Dr. Uwe Breuer from Central Division of Analytical Chemistry of Forschungszentrum Juelich for the fabrication of the Si substrate with a buried $CoSi_2$ layer needed for the fabrication of the first Si-MCLED with $CoSi_2$ as a bottom mirror.

- My thanks belong also to colleagues from FZD who supported me in my research work and helped me with measurements, especially to Sylvio Probst (EL), Prof. Dr. Jiaming Sun (EL, PL), Dr. Arndt Mücklich (TEM), Uta Lucchesi (FTIR, Raman), Dr. Volkhard Beyer (VASE) and Dr. Michael Zier (IV measurements).
- The external colleagues Dr. Mohamed Benyoucef and Dr. Armando Rastelli from the Institute for Integrative Nanosciences of IFW Dresden for the possibility to make an optical characterisation in IFW labs.
- Dr. Thomas Gemming from the Institute for Complex Materials IFW Dresden for the TEM sample preparation using FIB and for the cross section TEM images of MCLEDs.
- Especially I am obliged to Dr. Jan Schmidt and Dr. Hermann Seifarth for their their help, support, interest and valuable hints.
- I would like to give my special thanks to my parents for enabling me the necessary education and my boyfriend Hagen whose patient love enabled me to complete this work.

Declaration / Versicherung

Hereby, I do solemnly and sincerely declare that this dissertation was done by me, personally. Due acknowledgement has been made in the text to all other sources and material used. The material has not been accepted in whole, or in part, for any other degree. This dissertation has been prepared at the Institute of Ion Beam Physics and Materials Research of the Research Center Dresden-Rossendorf under the guidance of Professor Dr. Manfred Helm and Dr. Bernd Schmidt.

Hiermit versichere ich, dass ich die vorliegende Arbeit ohne unzulässige Hilfe Dritter und ohne Benutzung anderer als der angegebenen Hilfsmittel angefertigt habe. Gedanken, die aus fremden Quellen direkt oder indirekt übernommen wurden, sind als solche kenntlich gemacht. Die Arbeit wurde bisher weder im Inland noch im Ausland in gleicher oder ähnlicher Form einer anderen Prüfungsbehörde vorgelegt. Ich erkenne die Promotionsordnung der Technischen Universität Dresden an. Diese Dissertation wurde am Institut für Ionenstrahlphysik und Materialforschung des Forschungszentrums Dresden-Rossendorf unter der wissenschaftlichen Betreuung von Professor Dr. Manfred Helm sowie Dr. Bernd Schmidt angefertigt.

Dresden, Juli 9, 2009

Major statements (Thesen)

- Realising Si-based electrically driven light emitters in a process technology compatible with mainstream microelectronics CMOS technology is key requirement for the implementation of low-cost Si-based optoelectronics and thus one of the big challenges of semiconductor technology.

- The aim of this work was the development of microcavity enhanced silicon light emitting diodes (MCLED), their design, fabrication, and experimental as well as theoretical analysis.

- Based on the Fabry-Perot theory and the measured electroluminescence (EL) spectrum of simple bulk silicon pn-diodes published by Sun (APL, 2003) an ideal Si based 1λ MCLED has been simulated for a resonance wavelength 1150 nm. According to the calculations the extraction efficiency increases from the value of 3% (simple Si LED) up to 26% (MCLED).

- The realisation of the aim of this work was split into the following steps: a) structural and optical investigations of single SiO_2 and amorphous Si (a-Si) layers fabricated by magnetron sputter deposition, b) deposition and characterisation of multilayer stacks of SiO_2 /a-Si forming the distributed Bragg reflectors and c) design, fabrication and characterisation of the completely processed MCLED.

- In the first experiments the properties, homogeneity, the thickness variation over the wafer and the deposition rates of single a-Si and SiO_2 layers, produced by magnetron sputter deposition, have been investigated. The goal was to find optimal deposition parameters, which allow the fabrication of high quality multilayer stacks based on a-Si and SiO_2 , forming a distributed Bragg reflectors (DBR). The investigations have shown that the structural and optical properties of the deposited material strongly depend on the deposition process parameters. The most critical variable parameter during the sputter deposition was the substrate bias.

- Subsequently, the optical properties of the distributed Bragg reflectors (DBRs), a stack of alternating layers with different index of refraction, were investigated. The thickness of each optical layer corresponds to one quarter of the wavelength for which the mirror is designed (for the resonant wavelength 1150 nm: $d_{SiO2} = 200$ nm and $d_{a-Si} = 80$ nm). Thickness deviations of all layers of about 10% were observed, which degradates slightly the properties of the DBRs. The use of a substrate bias during the deposition of the a-Si layers results in an increase of the reflectivity of the DBRs by about 1%.

- In a MCLED the spontaneous internal emission is controlled by placing the emitter inside an optical cavity with a thickness of the order of its emitting wavelength. The resulting interference effects increase the part of the emission that can be extracted. In this work two different concepts have been followed a) MCLED with a bottom $CoSi_2$ mirror and top DBR, and b) MCLED with two DBRs.

- In the first concept the 1λ thick silicon light emitting layer was embedded between metallic $CoSi_2$ mirror at the bottom and 2.5 pairs SiO_2 /a-Si DBR at the top. The result of the investigation of this system is that due to the B diffusion, the light emitting region is fully spread across the microcavity active layer. The coupling of the light emission into the microcavity mode was achieved. However, the replacement of the $CoSi_2$ bottom mirror by the DBR decreases the light absorption losses.

  The second concept was based on silicon pn-diode placed between two DBRs. The pn-diodes were produced in thin silicon membranes with the thickness in the order of μm. In order to be able to control the thickness of the membranes the SOI (silicon on insulator) wafers with a 2 μm thick silicon device layer on the top of the buried oxide were used. The devices were tuned for a 4λ cavity (the thickness of the Si device layer is about d = 1300 nm), which is a good compromise between the optical properties and the mechanical stability of the MCLED. The final device analysed and described in this work has a thickness of the emitting silicon layer of 1751 nm, which corresponds to a 5.5λ cavity with the resonance maximum at 1146 nm. As a reference an LED fabricated on a 1620 nm thick device layer of the SOI substrate without DBRs was used (weak 5λ Fabry-Perot cavity). Further, the comparison of calculations with measured reflectance and electroluminescence spectra of both devices was made. The structures (thicknesses of all layers) of the LED on SOI and of the MCLED were determined using the ellipsometry, TEM and FTIR. The extracted efficiency of the 5.5λ MCLED is $\eta_{extr} = 5\%$, wich corresponds to an enhancement by about 65% compared to the LED on a bulk silicon ($\eta_{extr} = 3\%$).

- A proof-of-principle of an electrically driven Si microcavity LED was demonstrated. However, several possibilities for a further improvement of the extracted light efficiency can be envisioned: *i*) shorter cavity length; *ii*) placing the pn-junction exactly into one antinode of the electric field amplitude by using the low energy boron implantation and subsequent rapid thermal annealing; *iii*) reducing the stress using Si_3N_4/SiO_2 DBRs, having also a smaller refractive index contrast; *iv*) in the case of planar diodes with p^+- and n^+-contacts on the top of the device the use of the interdigital structure design with multiple pn-MCLEDs; *v*) a vertically contacted MCLED with p^+-contact on the top and n^+-contact on the bottom of the active device layer - membrane; *vi*) a better confinement could be achieved by lateral patterning of the active layer of the MC into a 2D or 3D photonic crystal structures.